EUROPEAN RESPIRATORY journal
FLAGSHIP SCIENTIFIC JOURNAL OF ERS

Early View

Original Research Article

Aberrant and Ectopic Cell Populations in Restrictive Allograft Syndrome after Lung Transplantation

Lena M. Leiber, Leonard Christian, Lavinia Neubert, Jannik Ruwisch, Hande Yilmaz, Edith K. J. Plucinski, Linus T. Langer, Jan C. Kamp, Mark Greer, Bernd Haermeyer, Mark Kühnel, Christopher Werlein, Aurelien Justet, Anke K. Bergmann, Hanne Beeckmans, Matthias Ballmaier, Jawad Salman, Robin Vos, Lars Knudsen, Ulrich Martin, Bart M. Vanaudenaerde, Ali Önder Yildirim, Jens M. Hohlfeld, Fabio Ius, Florian Laenger, Tobias Welte, Christine Falk, Naftali Kaminski, Danny D. Jonigk, Jens Gottlieb, Jonas C. Schupp

Please cite this article as: Leiber LM, Christian L, Neubert L, *et al*. Aberrant and Ectopic Cell Populations in Restrictive Allograft Syndrome after Lung Transplantation. *Eur Respir J* 2026; in press (https://doi.org/10.1183/13993003.00537-2025).

Aberrant and Ectopic Cell Populations in Restrictive Allograft Syndrome after Lung Transplantation

Lena M. Leiber[1,2], Leonard Christian[1,2], Lavinia Neubert[2,3], Jannik Ruwisch[1,2], Hande Yilmaz[1,2], Edith K. J. Plucinski[2,3], Linus T. Langer[1,2], Jan C. Kamp[1,2,3], Mark Greer[1,2], Bernd Haermeyer[4], Mark Kühnel[2,5], Christopher Werlein[2,3], Aurelien Justet[6], Anke K. Bergmann[4], Hanne Beeckmans[7], Matthias Ballmaier[8], Jawad Salman[9], Robin Vos[7], Lars Knudsen[10], Ulrich Martin[2,9,11], Bart M. Vanaudenaerde[7], Ali Önder Yildirim[12], Jens M. Hohlfeld[1,2,13], Fabio Ius[2,9], Florian Laenger[5], Tobias Welte[1,2,†], Christine Falk[2,14], Naftali Kaminski[15], Danny D. Jonigk[2,3,5*], Jens Gottlieb[1,2*], Jonas C. Schupp[1,2,13,15*]

†Died March 10th, 2024
*Contributed equally

Affiliations: [1] Department of Respiratory Medicine and Infectious Diseases, Hannover Medical School, Hannover, Germany; [2] Biomedical Research in Endstage and Obstructive Lung Disease Hannover, German Center for Lung Research, Hannover, Germany; [3] Institute of Pathology, Hannover Medical School, Hannover, Germany; [4] Institute of Human Genetics, Hannover Medical School, Hannover, Germany; [5] Institute of Pathology, RWTH Aachen, Aachen, Germany; [6] Service de Pneumologie, CHU de Caen, Centre de compétence des maladies pulmonaires rares, ISTCT, UMR6030-CNRS-CEA-Université de Caen, Caen, France; [7] Laboratory of Respiratory Diseases and Thoracic Surgery (BREATHE), KU Leuven, Leuven, Belgium; [8] Central Research Facility Cell Sorting, Hannover Medical School, Hannover, Germany; [9] Clinic for cardiac, thoracic, transplant and vascular surgery, Hannover Medical School, Hannover, Germany; [10] Institute for Functional and Applied Anatomy, Hannover Medical School, Hannover, Germany; [11] Leibniz Research Laboratories for Biotechnology and Artificial Organs, Lower Saxony Center for Biomedical Engineering, Implant Research and Development, Hannover, Germany; [12] Institute of Lung Health and Immunity (LHI), Helmholtz Zentrum Muenchen, Institute of Lung Biology and Disease; Munich, Germany; [13]Department of Clinical Airway Research, Fraunhofer Institute for Toxicology and Experimental Medicine (ITEM), Hannover, Germany; [13] Institute of Transplant Immunology, Hannover Medical School, Hannover, Germany; [14] Section of Pulmonary, Critical Care and Sleep Medicine, Yale School of Medicine, New Haven, CT, United States

Corresponding author: Prof. Dr. med. Jonas C. Schupp; telephone number: +49 511-532-3934; fax number: +49 511-532-161139; e-mail address: schupp.jonas@mh-hannover.de

Running Title: Aberrant Cells in Restrictive Allograft Syndrome

Impact of our research: Our study provides the first-ever single-cell data on structural (i.e., parenchymal and supporting stromal) lung cells in restrictive allograft syndrome and reveals transcriptomic characterizations, such as aberrant cell populations, as well as their histologic localization and distribution patterns. Furthermore, we identify transcriptomic and histologic similarities and differences between idiopathic pulmonary fibrosis and restrictive allograft syndrome (RAS) and highlight potential therapeutic targets for RAS.

Author contributions: J.C.S. conceptualized, acquired funding, and supervised the study. J.G. performed cohort characterization and phenotyping. L.N., F.L., D.D.J., F.I., J.S., J.C.K., and M.K. procured, processed, and characterized RAS and control specimens. L.M.L. and L.C. dissociated the lungs and isolated the nuclei. M.B. performed FANS. L.M.L., L.C., and J.C.S. performed snRNA-seq barcoding and library construction. L.M.L., L.C., and the Research Core Unit Genomics (RCUG) of MHH conducted quality control of the libraries. B.H. and A.K.B. performed sequencing. All sequencing data were processed, curated, visualized, and analyzed by J.C.S. and L.M.L. HE, IHC, and IF including quantification were performed by L.M.L. and J.R. and analyzed by L.M.L., J.C.S., J.R., L.N. and D.D.J. Histologic images were generated by L.M.L. L.C. prepared the samples for micro-CT experiments, which were scanned by J.R. and L.K. and analyzed by J.R., L.K., J.C.S., and L.M.L. E.K.J.P. created the graphical abstracts based on specifications from J.C.S. and L.M.L. M.G., A.J., U.M., A.Ö.Y., B.V., R.V., J.H., H.B., C.F., and N.K. provided critical interpretation, review, and commentary on data and the manuscript. The manuscript was drafted by L.M.L. and J.C.S. and reviewed and edited by all authors.

Funding: Supported by Else Kröner-Fresenius Foundation (EKFS, 2023_EKCS.18, 2021_EKEA.16, 2020_EKSP.78), CORE100Pilot Advanced Clinician Scientist Program of Hannover Medical School funded by EKFS and the Ministry of Science and Culture of Lower Saxony, and by German Center for Lung research (FKZ 82DZL002B1, FKZ 82DZL002C1 & FKZ 82DZLT82C1, all to J.C.S.). R01HL127349, R01HL141852, U01HL145567, R21HL161723, P01HL11450, and a grant from Veracyte (NK), the Three Lakes Foundation (NK)

Total word count of the body of the manuscript: 3069

Abstract:

Rationale: Restrictive allograft syndrome (RAS) is a major cause of mortality following lung transplantation due to progressive fibrosis of the lung allograft with no therapeutic options. Knowledge of the cellular and molecular mechanisms driving fibrosis in RAS remains limited.

Objective: To characterize the cellular and molecular changes in human RAS lungs through single-cell transcriptomic profiling.

Methods: Single-nucleus RNA-sequencing (snRNA-seq) was performed in peripheral lung tissues from 15 RAS patients undergoing lung re-transplantation, and from 9 healthy control lungs. Findings were validated and extended using histologic techniques including immunofluorescence, RNA *in situ* hybridization, Elastica-van-Gieson immunohistochemistry, quantitative histological analyses, and micro-CT scans.

Measurements and Main results: snRNA-seq analysis of RAS lungs revealed previously undescribed aberrant basaloid cells, ectopic *COL15A1*$^{+}$ peribronchial vascular endothelial cells (pVECs), and *CTHRC1*$^{+}$ fibrotic fibroblasts. Histologic stains disclosed distinctive distribution patterns: aberrant basaloid cells, primarily localized at the fibrotic edge, together with juxtaposed *CTHRC1*$^{+}$ fibrotic fibroblasts and ectopic *COL15A1*$^{+}$ pVECs form the fibrotic niche of alveolar fibroelastosis (AFE). *PRX*$^{+}$ alveolar microvasculature is partially lost in AFE areas. Micro-CT scans revealed changes from pulmonary to systemic perfusion, facilitated by *COL15A1*$^{+}$ pVECs. Last, our data reveals potential therapeutic targets in RAS, including integrin αvβ6, activator of TGFβ.

Conclusion: Considering the multifaceted differences of RAS and idiopathic pulmonary fibrosis, we revealed a surprising general principle of an entity-spanning composition of the fibrotic niche by aberrant basaloid cells localized at the fibrotic edge, ectopic *COL15A1*$^{+}$ pVECs and *CTHRC1*$^{+}$ fibrotic fibroblasts. This suggests a flexible but cellular pathogenesis-guided transferability of potential therapeutic approaches between progressive fibrotic lung diseases.

Word count: 250 words

ERJ Key words: interstitial lung diseases, pulmonary fibrosis, lung transplantation, tissue remodeling, RNA expression, histology

Mesh browser Key words: Single-Cell Analysis [E05.242.900], Lung Diseases, Interstitial [C08.381.483], Graft Rejection [G12.875.545.328], Lung Transplantation [E04.928.600.495], Pulmonary Fibrosis [C08.381.483.652]

INTRODUCTION:

Chronic lung allograft dysfunction (CLAD) after lung transplantation (LuTx) is an aggressive remodeling process caused by various factors, including allo- and auto-immunity, infection, aspiration and ischemia. Due to lacking therapeutic options, CLAD remains a major cause of post-LuTx morbidity, re-transplantation, and post-LuTx mortality. CLAD manifests as restrictive and/or obstructive phenotypes.(1–3) Up to 30 % of CLAD patients develop the restrictive phenotype, termed restrictive allograft syndrome (RAS).(2,4) RAS is associated with a worse prognosis than the obstructive phenotype, bronchiolitis obliterans syndrome (BOS), with survival rates after diagnosis of 6–18 months versus 3–5 years.(2,5–8) Histologically, RAS lung tissue is characterized by alveolar fibroelastosis (AFE)(6,9–11), defined by collagenous obliteration of alveoli, and de-epithelization/elastosis of alveolar walls with only scant inflammation.(9,11) A peculiar feature of AFE is the sharp transition from fibrosis to alveoli with an inconspicuous architecture, here referred to as the 'fibrotic edge'.(11)

Much of the current understanding of the pathogenesis and pathognomonic changes in RAS, including risk factors like acute cellular rejection, donor-specific antibodies, and late-onset diffuse alveolar damage, derives from animal models, bronchoalveolar lavage (BAL) or blood analyses.(6,8,12–14) Unpublished scRNA-seq data suggest that immune mechanisms also contribute to RAS pathogenesis.(15) However, a detailed characterization of structural cells in RAS lungs remains lacking. In this study, we performed the first single-cell transcriptomic analysis of structural (i.e., parenchymal and supporting stromal) lung cells in human RAS lungs using a data-driven approach to elucidate the cellular and gene expression changes underlying the histopathological characteristics of this poorly understood syndrome. We identified by single-nucleus RNA-sequencing (snRNA-seq) the previously undescribed

presence of aberrant basaloid cells, ectopic *COL15A1*$^{+}$ peribronchial endothelial cells (pVECs) and *CTHRC1*$^{+}$ fibrotic fibroblast populations in RAS. Tissue stains and micro-CT scans revealed distinctive distribution patterns of these cells, the absence of bronchiolization in RAS, and a previously undescribed change of perfusion in the RAS lung.

Parts of these data were previously presented as an abstract at the ERS Congress 2024.(16)

MATERIAL AND METHODS:

Detailed experimental methods and stains of control lungs are provided in the online data supplement. We performed snRNA-seq using peripheral lung parenchyma from upper lobes of 15 RAS patients undergoing lung re-transplantation, phenotyped according to current International Society for Heart & Lung Transplantation (ISHLT) criteria, and upper lobe samples from 9 control lungs (surgical size adjustment during lung transplantation n = 5; histologically tumor-free specimen n = 4; Fig. 1A, Suppl. Fig. E1, Suppl. Table E1).(6) SnRNA-seq data were processed with CellRanger and analyzed using R and the Seurat package. Transcriptomic data was deposited on Gene Expression Omnibus under the accession number GSE284081. Epithelial, endothelial and stromal cell populations were characterized through iterative clustering followed by differential expression analysis. To focus on structural alterations, immune cells were excluded from this study. Wilcoxon rank sum test with Bonferroni correction of *P* values for multiple comparisons established cell type-specific marker genes (Suppl. Table E2). Epithelial, endothelial and stromal cell subpopulations were validated and localized by immunofluorescent (IF) microscopy, RNA *in situ* hybridization (RNA-ISH),

immunohistochemistry (IHC), and combined Elastica van Gieson-immunohistochemistry (EvG-IHC) stains using FFPE samples derived from the same lung explants used for snRNA-seq, enabling direct molecular and histological correlation within individual specimens (n = 8 RAS and n = 12 control lungs for IF; n = 5 RAS and n = 4 control lungs for RNA-ISH; n = 8 RAS and n = 4 control lungs for EvG-IHC) (Suppl. Tables E3, E4, Suppl. Figs. E2–E23, E27). For quantitative analysis of IF and RNA-ISH images, cell segmentation and machine-learning-based quantification were performed using QuPath (v0.5.1) and the StarDist extension (Suppl. Fig. E24).(17,18) Micro-CT scans of two RAS specimens provided further insights into the structural characteristics of RAS. No blinding was performed in this study.

All biological materials and data were collected following written informed consent from the patients and approval from the Ethics Committee of Hanover Medical School (IRB # 10141_BO_K_2022).

RESULTS:

SnRNA-seq was applied to 105,952 single nuclei from 15 RAS and 9 control specimens (Fig. 1B). A technical summary, including median UMI/genes/reads per nucleus, reads mapped to probe set, and the number of detected genes, is provided in the supplement (Supp. Table E2A). Based on distinct markers, all major lung cell types were identified, as well as aberrant basaloid cells, ectopic *COL15A1*$^{+}$ pVECs and *CTHRC1*$^{+}$ fibrotic fibroblasts - previously discovered in idiopathic pulmonary fibrosis (IPF)(19,20) but not in RAS (Fig. 1B–D, Suppl. Fig. E25). Detailed marker gene expressions of all profiled nuclei are provided in the supplement (Suppl. Table E2B).

SnRNA-seq analysis of the epithelial cell repertoire identified the presence of aberrant basaloid cells in human RAS lungs

40,390 single nuclei (n = 24,565 RAS; n = 15,825 control), representing 38.1 % of all profiled nuclei, were identified as epithelial cells based on distinct marker genes. Major epithelial cell populations of the human lung, including alveolar type 1 (AT1) and type 2 (AT2) cells, basal cells, ciliated cells, and secretory cells were identified in all specimens (Fig. 2A–D, Suppl. Table E2C). Additionally, we detected aberrant basaloid cells in all but one of our RAS specimens. This characteristic cell type was first described in 2020 in human IPF lungs, and, to a lesser extent, in Chronic Obstructive Pulmonary Disease (COPD) lungs.(19,20) Aberrant basaloid cells express the basal cell markers *KRT17* and *LAMB3* alongside canonical epithelial markers but lack other established basal cell markers such as *KRT5* and *KRT15*. Furthermore, they express senescence-related genes (*CCND1, MDM2*, and *GDF15*) and markers of epithelial-mesenchymal transition (EMT) (*CDH2*, *COL1A1*, *VIM*, and *FN1*) (Fig. 2D, Suppl. Table E2C).(19) Also, they show the highest expression levels of genes coding for the integrin subunits αvβ6 (*ITGAV*, *ITGB6*), activators of TGFβ, compared to all other cell types in our specimens (Fig. 2D, Suppl. Table E2B). Pathway analysis confirmed their unique profile including TGFβ receptor signaling in EMT (Suppl. Fig. E26). We identified 1,274 aberrant basaloid cells in RAS matching this unique gene signature, representing a median of 5.4 % of the epithelial cell compartment in RAS patients (vs. controls, unadjusted $p < 0.0001$, Wilcoxon rank-sum test, Fig. 2B, Fig. 2C; Suppl. Table E2H). Correlation analysis with the IPF cell atlas data confirmed the transcriptional concordance of aberrant basaloid cells between RAS and IPF (Fig. 1D).(19)

Aberrant basaloid cells are localized at the fibrotic edge

We confirmed the presence of aberrant basaloid cells in RAS tissue and investigated their distribution by IF using antibodies against *KRT17*, *TP63*, *CTSE*, *integrin αvβ6*, and *COX2* - a distinctive marker combination not overlapping with any other common lung cell type (Fig. 2D, Suppl. Table E2B).(19) Additionally, we included *TP63* for immunofluorescence validation as it is an established and literature-supported characteristic marker gene of aberrant basaloid cells.(19–25) *KRT17*, *TP63* and *integrin αvβ6* served to identify aberrant basaloid epithelial cells, while *CTSE* and *COX2* were interpreted as more broadly expressed epithelial injury marker. All RAS samples exhibited the same characteristic distribution pattern of aberrant basaloid cells: they consistently localize to the margin of the fibrotic edge, lining it almost continuously in a single cell layer. Additionally, aberrant basaloid cells invade the alveolar space in a branching pattern lining fibrotically thickened alveolar septa (Fig. 3A–C, Suppl. Figs. E2–7, Suppl. Fig. E23). Throughout the samples, we observed and quantified an epithelial gradient in RAS: aberrant basaloid cells occur frequently at the fibrotic edge and become increasingly rare toward healthy-looking alveoli, until eventually disappearing (Suppl. Fig. E24A, Suppl. Fig. E24B). In contrast to IPF, myofibroblast foci covered by aberrant basaloid cells were a rare histological finding in RAS. No aberrant basaloid cells were detected in control specimens (Suppl. Figs. E8–E11).

Fully developed AFE is characterized by a homogeneous, pauci-cellular fibrosis with preserved elastic fibers of the remnant alveolar walls, which are denuded of epithelial cells, while the former alveoli are filled with collagen. Near the fibrotic edge, we consistently observed multiple air-containing structures, which we termed “obliterating alveoli”. Lining epithelial cells of obliterating alveoli have lost contact to remnant alveolar walls due to thick

collagen depositions (see EvG stains in Fig. 3). Obliterating alveoli consist of aberrant basaloid cells, *SFTPC*$^{+}$/*KRT17*$^{+}$ transitional cells, and *LAMP*$^{+}$/*AGER*$^{+}$ AT1 cells, most of which are pathologically *CTSE*$^{+}$ (Fig. 3, Suppl. Fig. E24D–F). Although combinations of these cell types exist, most obliterating alveoli contain at least some aberrant basaloid cells (Suppl. Fig. E24D–F). In general, aberrant basaloid cells seem to exclusively appear in monolayers, regardless of their localization in RAS lung tissue.

The endothelial cell repertoire is shifted towards ectopic *COL15A1*$^{+}$ peribronchial vascular endothelial cells, and shows a loss of *PRX*$^{+}$ alveolar microvasculature

27,657 single nuclei (n = 15,309 RAS; n = 12,348 control), representing 26.1 % of all profiled nuclei, were identified as endothelial cells (ECs) based on distinct markers (Fig. 4A–D, Suppl. Table E2D). We identified all known EC populations of the human lung in all specimens, including arterial ECs, aerocytes, general capillary ECs (gCAPs), venous ECs, lymphatic ECs, and *COL15A1*$^{+}$ pVECs (Fig. 4A–D, Suppl. Table E2D)(26). *COL15A1*$^{+}$ pVECs are known to form vessels adjacent to major airways and subpleural vessels, and their transcriptomic profile (e.g., *COL15A1, PLVAP, SPRY1, ZNF385D*) aligned with previous studies (Fig. 4D, Suppl. Table E2D).(19,26) Pathway analysis suggests unique signaling through e.g., INSR, calcitonin-like ligands and tachykinin receptors (Suppl. Fig. E26). In RAS, the endothelial repertoire showed a significant increase in *COL15A1*$^{+}$ pVECs (1.9 % vs. 8.2 %, unadjusted p = 0.04, Wilcoxon rank-sum test, Fig. 4B, Suppl. Table E2H). Additionally, we observed a non-significant trend toward a decreased fraction of aerocytes in RAS (median percentage 11.2 % RAS vs. 26.0 % control, unadjusted p = 0.055; Fig. 4B).

IF revealed ectopic *COL15A1*$^{+}$ pVECs in RAS, partially replacing *PRX*$^{+}$ alveolar microvasculature

We validated the presence of *COL15A1*$^{+}$ pVECs using antibodies against their distinctive markers *COL15A1* and *PLVAP* alongside the pan-endothelial marker *CD31*. In control specimens, *COL15A1*$^{+}$ pVECs are strictly limited to peribronchial vasculature or to larger vessels of the pleura and do not contribute to the normal alveolar microvasculature (aerocytes and gCAPs), which stains positive for the pan-microvasculature marker *PRX* (Suppl. Figs. E15–17).(26) In RAS, *COL15A1*$^{+}$ pVECs show a deviating distribution pattern: they are no longer restricted to peribronchial vasculature and pleura but expand substantially (Fig. 5, Suppl. Fig. E24C). We refer to all *COL15A1*$^{+}$ pVECs outside locations adjacent to major airways or the pleura as 'ectopic pVECs'. This designation is based solely on their spatial localization, as transcriptomic profiles of ectopic and non-ectopic *COL15A1*$^{+}$ pVECs were not distinguishable in our study. Remarkably, ectopic pVECs gradually expand parallel to the aberrant basaloid cell gradient, forming vessels at fibrotic areas adjacent to the fibrotic edge. Toward the dense fibrotic subpleural space, we observed a non-significant rarefication of ectopic pVECs. However, while ectopic pVECs are extensively present in fibrotic areas, we observed a significantly reduced number of *PRX*$^{+}$ vessels in these areas compared to the alveolar tissue (Fig. 5A–C, Suppl. Fig. E24C). Similar to our epithelial findings, ectopic pVECs are not restricted to fibrotic areas but invade alveolar tissue (Fig. 5A–C, Suppl. Fig. E24C). Where ectopic pVECs reach into alveolar tissue, we observed a loss of physiologic *PRX*$^{+}$ alveolar microvasculature in both, IF and EvG-IHC stains (Fig. 5A–F, Suppl. Figs. E12–14).

Micro-CT imaging with 3D reconstruction revealed pronounced vascular remodeling in the dense zone of subpleural fibrotic consolidation in RAS tissue (Fig. 5G). Virtual sectioning

showed extensive sprouting of vasculature-like structures within the subpleural fibrosis, extending into AFE areas. Most of these vasculature-like structures were *CD31*$^{+}$ and *COL15A1*$^{+}$ in sequential EvG-IHC stains (Fig. 5D–F). Morphologically, these vascular structures appear to originate from the pleura, as cross-sections became narrower with increasing distance from the pleura (Fig. 5G).

The stromal cell compartment contains *CTHRC1*$^{+}$ fibrotic fibroblasts in RAS

37,905 single nuclei (n = 20,712 RAS; n = 17,193 control), representing 35.8 % of all profiled nuclei, were identified as stromal cells based on distinct markers. They include pericytes, smooth muscle cells (SMC), mesothelium, and fibroblast populations. Within fibroblasts, we identified distinct subpopulations, including alveolar fibroblasts, stressed alveolar fibroblasts, adventitial fibroblasts, and *CTHRC1+* fibrotic fibroblasts (Fig. 6A–D, Suppl. Table S2E).(27) While *CTHRC1*$^{+}$ fibrotic fibroblasts were found in RAS and control subjects, they compose a significantly higher fraction of all stromal cells in RAS compared to controls (median percentage among stromal cells: 21.5 % RAS vs. 6.4 % control, p = 0.0002; Fig. 6B, Suppl. Table E2H). In contrast, the fraction of alveolar fibroblasts in RAS is significantly reduced (RAS vs. control: 38.0 % vs. 48.5 %, unadjusted p = 0.005; Fig. 6B). The identified *CTHRC1*$^{+}$ fibrotic fibroblasts exhibited a distinct transcriptional profile: aside from *CTHRC1*, they exhibit the highest expression of collagens *COL1A1* and *COL3A1*, ECM-related genes such as *COMP*, *LUM*, *SPARC*, *THBS2*, *POSTN*, *FN1*, the growth factor *VEGFA*, the matricellular protein *CCN4*, the TGF-β signaling pathway activator *INHBA*, and the secreted serine protease *PLAU* (Fig. 6D, Fig. 6E, Suppl. Table E2E). Biological pathways enriched in *CTHRC1*$^{+}$ fibrotic fibroblasts include: elastic fiber formation; chondroitin sulfate, dermatan sulfate and peptide hormone biosynthesis; activation of matrix metalloproteinases; collagen degradation,

collagen chain biosynthesis and modifying enzymes, and collagen chain trimerization (Fig. 6F, Suppl. Table E2F). Taken together, marker gene expression and enriched pathways of *CTHRC1*$^+$ fibrotic fibroblasts highlight their prominent role in the fibrotic remodeling of AFE.

RNA *In Situ* Hybridization reveals localization of *CTHRC1*$^+$ fibrotic fibroblasts in RAS

RNA *in situ* hybridization (RNA-ISH) stains of *CTHRC1*$^+$/*COL1A1*$^+$ fibrotic fibroblasts revealed a predominant localization of *CTHRC1*$^+$ fibrotic fibroblasts in areas of AFE in RAS, with only very few *CTHRC1*$^+$ fibrotic fibroblasts observed in controls (Suppl. Fig. E21). *CTHRC1*$^+$ fibrotic fibroblasts are ubiquitously distributed across all areas of AFE, occasionally forming fibroblast foci at the fibrotic edge. In contrast to aberrant basaloid and ectopic pVECs, *CTHRC1*$^+$ fibrotic fibroblasts were present in all areas of fibrosis, not only at the fibrotic edge. Outside fibrotic AFE areas, *CTHRC1*$^+$ fibrotic fibroblasts were sporadically observed in small nests in thickened alveolar septa in more distal RAS tissue, but not in healthy-looking alveolar walls (Fig. 6G–I, Suppl. Figs. E18–20, Suppl. Fig. E24G-H).

DISCUSSION:

In this study, we provide the first single-cell transcriptomic catalogue of structural lung cells in human RAS. Our snRNA-seq data revealed aberrant basaloid cells, *COL15A1*$^+$ pVECs, and *CTHRC1*$^+$ fibrotic fibroblasts overlapping with previously identified cell populations in IPF.(19) Other IPF-associated changes, such as proximalization of the alveolar epithelium, where AT1 and AT2 cells are replaced by airway cell populations, were not observed, since our

data shows neither a significant decline in AT1 and AT2 cells, nor an increase in airway-derived cells (Fig. 2B).(19) We validated the previously unknown presence of aberrant basaloid cells, ectopic *COL15A1*$^{+}$ pVECs, and *CTHRC1*$^{+}$ fibroblasts in RAS by IHC, IF and RNA-ISH, and identified their unique distribution patterns.

While allograft airway epithelial cells have been linked to fibroproliferation and aberrant tissue repair in BOS(28,29), little was known about epithelial changes in RAS. Aberrant basaloid cells are disease-associated cells, which have been found in IPF and scleroderma with pulmonary involvement, and to a much lesser extent in COPD.(19–21) Their origin remains elusive, but recent research indicates that human AT2 cells can transdifferentiate into aberrant basaloid cells.(30) Their discovery in the human RAS lung suggests previously unknown commonalities between these clinically distinct entities, as their expression profile closely matches the aberrant basaloid cell population identified by Adams et al. in human IPF lungs.(19) Our data indicates a relevant contribution of this cell population to the pathogenesis and/or disease progression of RAS for the following reasons: first, we identified aberrant basaloid cells in all but one of our RAS specimens, but none in control specimens, supporting the hypothesis that aberrant basaloid cells are a pathognomonic feature of fibrotic lung diseases in general and a hallmark of RAS specifically. Second, their unique expression profile may promote the fibrotic remodeling seen in AFE regions of RAS lungs. This is indicated by the epithelial-mesenchymal transition (EMT)-like phenotype, and the high expression of genes associated with the pathogenesis of IPF such as integrin αVβ6, *MMP7*, *GDF15*, and *EPHB2*. Third, cellular senescence is associated with disease progression in age-related and chronic diseases like IPF, as well as frailty and transplant-specific complications in solid-organ transplants.(31) Thus, aberrant basaloid cells likely drive

pathologic cellular senescence in RAS due to their expression of multiple senescence markers, including *CDKN1A*, *CDKN2B*, *MDM2*, and *GDF15*.

Little is known about the endothelial cell compartment in RAS patients and its possible pathologic impacts. Similar to IPF, we observed significantly expanded *COL15A1*$^{+}$/*PLVAP*$^{+}$ ectopic pVECs in RAS, with largely overlapping transcriptomic profile.(19) In RAS, ectopic pVECs at the fibrovascular interface are characteristically distributed parallel-running to the aberrant basaloid cell gradient, potentially due to repetitive endothelial injury.(32) EvG-IHC staining demonstrated that ectopic pVECs in obliterated AFE regions lack spatial connections to former alveolar septa, indicating potential neoangiogensis. Moreover, wherever ectopic pVECs infiltrate the alveolar microvasculature, normal *PRX*$^{+}$ alveolar capillaries are missing. Similar observations in IPF and nonspecific interstitial pneumonia(19,30,33) suggest a contribution of vascular ECs, particularly *COL15A1*$^{+}$ pVECs, to the pathogenesis of RAS and other fibrotic diseases. We hypothesize that these ectopic *COL15A1*$^{+}$/*PLVAP*$^{+}$ pVECs may not possess full barrier function: *PLVAP* forms the diaphragms of fenestrated endothelium, potentially influencing vascular permeability and leukocyte trafficking/transmigration, and is typically absent in mature barrier endothelium.(34,35) Based on this, we propose that ectopic pVECs might contribute to impaired gas exchange and vascular permeability in the RAS lung. The origin and exact role of ectopic pVECs in RAS remains enigmatic nonetheless.

AFE is characterized by collagen-rich fibrosis and hyperelastosis within the remodeled alveolar walls.(9,11,36–38) In our data, *CTHRC1*$^{+}$ fibrotic fibroblasts emerged as key mediators of fibroelastotic remodeling in RAS(13,14), as they express numerous fibrosis-associated genes, including *BMP1*, *COL1A2*, *COL3A1*, *CXCL12*, *CTHRC1*, *MMP2*, *MMP14*, *PLOD2*, *SERPINE1*, *TIMP1*, and *TIMP2*.(27) The transcriptional profile of these CTHRC1^{+} fibrotic fibroblasts is highly consistent with that of the *CTHRC1*$^{+}$ myofibroblast subpopulation

previously described in IPF.(19,27) Pathway analysis in *CTHRC1*$^{+}$ fibrotic fibroblasts revealed key pathomechanisms of AFE, including elastogenesis, collagenesis, elastic fiber and ECM formation, organization, and regulation. The fibroblast to *CTHRC1*$^{+}$ myofibroblast conversion through *SFRP1*$^{+}$ transitional fibroblasts has been recently unraveled.(39) *CTHRC1*$^{+}$ fibrotic fibroblasts are known key drivers of fibrosis, not only in the lung (e.g., IPF and scleroderma-associated interstitial lung disease), but in organ fibrosis throughout.(40–42)

While our data reveals multiple unexpected similarities between IPF and RAS, it is equally important to emphasize their differences: in IPF, aberrant basaloid cells characteristically line the active edge of pathognomonic myofibroblast foci(19), whereas myofibroblast foci are rare in RAS. Further, the histo-anatomical distribution of ectopic pVECs differs between IPF and RAS: in IPF, ectopic pVECs are associated with areas of bronchiolization, whereas in RAS, bronchiolization is absent, and ectopic pVECs primarily localize in AFE areas, possibly contributing to a shift from pulmonary to systemic perfusion.

Currently, no effective therapy for RAS is available. In this context, our observation of markedly elevated expression levels of genes encoding the integrin subunits αvβ6 in aberrant basaloid cells is of potential relevance. Integrin αvβ6 can activate latent TGF-β1, and its high expression is known to substantially contribute to organ fibrosis.(43) Integrin αvβ6 therefore emerged as a promising therapeutic target for IPF.(44) Moreover, increased expression levels of TGF-β1 have also been reported in BAL analysis from RAS patients and linked to the development of BOS.(45,46) Collectively, these observations raise the possibility that integrin αvβ6 may also play a role in RAS pathogenesis and could represent a candidate target for future therapeutic investigations. Our snRNA-seq dataset may serve as a reference atlas for exploring the relevance and applicability of anti-fibrotic strategies in RAS.

Our study has certain limitations. First, the size of our cohort may not capture the complete heterogeneity of RAS. However, we analyzed samples from 15 well-characterized RAS patients, which represents a substantial number given the rarity of this condition. Due to limited availability of suitable specimens, the same cohort had to be used for both transcriptomic profiling and histological validation. Second, analyzing end-stage RAS tissue provides insights into the pathophysiologic characteristics of RAS, which may be more ambiguous or absent in earlier disease stages. Furthermore, this single-time point study could not study mechanisms of disease progression. Third, due to the integration approach of our snRNA-seq data analysis, some nuclei of our control specimens were spuriously identified as aberrant basaloid cells and as *CTHRC1*$^{+}$ fibrotic fibroblasts. However, their gene expression profiles showed substantially reduced expression of major aberrant basaloid-/*CTHRC1*$^{+}$ fibrotic fibroblast-specific marker genes (Figs. 2D, 6D,E, Suppl. Fig. E26C). Fourth, as we provide nuclei data, capturing the entire transcriptome is inherently not possible, but we still cover the large majority of transcripts at a single-cell resolution. Furthermore, given the limited availability of published snRNA-seq data in IPF profiled with the same technology, we restricted our comparisons to IPF to qualitative alignments based on shared marker genes and cell-type identities. Future single-cell or single-nucleus RNA-seq data sets will be needed to confirm and complement our findings. Fifth, as histological protein marker expression was evaluated using serial tissue sections, definitive multi-target co-expression at the single-cell level cannot be determined; interpretations therefore rely on concordant localization across adjacent microanatomical regions. And last, to enable a focused and high-resolution analysis, we concentrated on RAS and the structural cell compartment. A simultaneous characterization of immune cell populations or a comparative transcriptomic analysis including BOS would have required the integration of extensive additional datasets. Given the

limited existing knowledge on RAS, such breadth was not feasible within a single study and should therefore be addressed in future investigations.

Taken together, this study - in combination with previous scRNA-seq studies in fibrotic lung diseases(19–21) - reveals a striking, but common cellular similarity in fibrotic lung diseases, despite differing histomorphological patterns, such as the usual interstitial pneumonia pattern in IPF and AFE pattern in RAS. Specifically, we observed that the fibrotic niche in both diseases is consistently formed by aberrant basaloid cells, ectopic *COL15A1*$^{+}$ pVECs, and *CTHRC1*$^{+}$ fibrotic fibroblasts (Fig. 7A–C). These findings provide a strong rationale for further investigating the potential transferability of IPF-specific therapeutic strategies to RAS. The unexpected transcriptomic similarity of key fibrotic cell populations in both diseases suggests overlapping molecular mechanisms that may be therapeutically exploitable. Nonetheless, future studies are needed to validate these parallels and assess their translational relevance.

ACKNOWLEDGMENTS:

We are indebted with great gratitude to all patients who enabled conducting this study by their participation. We thank the Fiedler lab, the Braun lab, and the Prasse lab for the generous provision of their lab devices, and Regina Engelhardt for excellent histopathological support. Figures 1A, 7 and our graphical abstract were created using BioRender.com.

REFERENCES:

1. Silva T de, Voisey J, Hopkins P, Apte S, Chambers D, O'Sullivan B. Markers of rejection of a lung allograft: state of the art. Biomark Med. 2022 Apr;16(6):483–98. doi:10.2217/bmm-2021-1013

2. Sato M, Waddell TK, Wagnetz U, Roberts HC, Hwang DM, Haroon A, et al. Restrictive allograft syndrome (RAS): a novel form of chronic lung allograft dysfunction. J Heart Lung Transplant Off Publ Int Soc Heart Transplant. 2011 Jul;30(7):735–42. doi:10.1016/j.healun.2011.01.712 PubMed PMID: 21419659.

3. Smirnova NF, Riemondy K, Bueno M, Collins S, Suresh P, Wang X, et al. Single-cell transcriptome mapping identifies a local, innate B cell population driving chronic rejection after lung transplantation. JCI Insight. 2022 Sep 22;7(18):e156648. doi:10.1172/jci.insight.156648

4. Pakhale SS, Hadjiliadis D, Howell DN, Palmer SM, Gutierrez C, Waddell TK, et al. Upper lobe fibrosis: a novel manifestation of chronic allograft dysfunction in lung transplantation. J Heart Lung Transplant Off Publ Int Soc Heart Transplant. 2005 Sep;24(9):1260–8. doi:10.1016/j.healun.2004.08.026 PubMed PMID: 16143243.

5. Todd JL, Jain R, Pavlisko EN, Finlen Copeland CA, Reynolds JM, Snyder LD, et al. Impact of forced vital capacity loss on survival after the onset of chronic lung allograft dysfunction. Am J Respir Crit Care Med. 2014 Jan 15;189(2):159–66. doi:10.1164/rccm.201306-1155OC PubMed PMID: 24325429; PubMed Central PMCID: PMC3983891.

6. Glanville AR, Verleden GM, Todd JL, Benden C, Calabrese F, Gottlieb J, et al. Chronic lung allograft dysfunction: Definition and update of restrictive allograft syndrome—A consensus report from the Pulmonary Council of the ISHLT. J Heart Lung Transplant. 2019 May;38(5):483–92. doi:10.1016/j.healun.2019.03.008

7. Klouda T, Vargas SO, Midyat L. Restrictive allograft syndrome after lung transplantation. Pediatr Transplant. 2021 May;25(3):e14000. doi:10.1111/petr.14000

8. Fernandez IE, Heinzelmann K, Verleden S, Eickelberg O. Characteristic patterns in the fibrotic lung. Comparing idiopathic pulmonary fibrosis with chronic lung allograft dysfunction. Ann Am Thorac Soc. 2015 Mar;12 Suppl 1:S34-41. doi:10.1513/AnnalsATS.201410-476MG PubMed PMID: 25830833.

9. Jonigk D, Rath B, Borchert P, Braubach P, Maegel L, Izykowski N, et al. Comparative analysis of morphological and molecular motifs in bronchiolitis obliterans and alveolar fibroelastosis after lung and stem cell transplantation. J Pathol Clin Res. 2017 Jan;3(1):17–28. doi:10.1002/cjp2.60

10. Verleden SE, Von der Thüsen J, Roux A, Brouwers ES, Braubach P, Kuehnel M, et al. When tissue is the issue: A histological review of chronic lung allograft dysfunction. Am J Transplant. 2020;20(10):2644–51. doi:10.1111/ajt.15864 PubMed PMID: 32185874.

11. Ofek E, Sato M, Saito T, Wagnetz U, Roberts HC, Chaparro C, et al. Restrictive allograft syndrome post lung transplantation is characterized by pleuroparenchymal fibroelastosis. Mod Pathol. 2013 Mar;26(3):350–6. doi:10.1038/modpathol.2012.171

12. Verleden GM, Glanville AR, Lease ED, Fisher AJ, Calabrese F, Corris PA, et al. Chronic lung allograft dysfunction: Definition, diagnostic criteria, and approaches to treatment-A consensus report from

the Pulmonary Council of the ISHLT. J Heart Lung Transplant Off Publ Int Soc Heart Transplant. 2019 May;38(5):493–503. doi:10.1016/j.healun.2019.03.009 PubMed PMID: 30962148.

13. Lynch TJ, Ahlers BA, Swatek AM, Ievlev V, Pai AC, Brooks L, et al. Ferret Lung Transplantation Models Differential Lymphoid Aggregate Morphology Between Restrictive and Obstructive Forms of Chronic Lung Allograft Dysfunction. Transplantation. 2022 Oct 1;106(10):1974–89. doi:10.1097/TP.0000000000004148 PubMed PMID: 35442232; PubMed Central PMCID: PMC9529760.

14. Todd JL, Weigt SS, Neely ML, Grau-Sepulveda MV, Mason K, Sever ML, et al. Prognosis and Risks for Probable Chronic Lung Allograft Dysfunction: A Prospective Multicenter Study. Am J Respir Crit Care Med. 2024 Oct 29;rccm.202403-0568OC. doi:10.1164/rccm.202403-0568OC

15. Duong A, Moshkelgosha S, Wong AK, Berra G, Renaud-Picard B, Wilson G, et al. Single-Cell RNA Sequencing Identifies Unique Pulmonary Macrophage Subsets Associated with Chronic Lung Allograft Dysfunction. J Heart Lung Transplant. 2022 Apr;41(4):S20. doi:10.1016/j.healun.2022.01.042

16. Leiber LM, Christian L, Neubert L, Yilmaz H, Kamp JC, Plucinski EK, et al. Single-nuclei RNA-seq reveals aberrant cell populations in restrictive allograft syndrome after lung transplantation. In: Transplantation [Internet]. European Respiratory Society; 2024 [cited 2024 Dec 18]. p. OA985. Available from: http://publications.ersnet.org/lookup/doi/10.1183/13993003.congress-2024.OA985 doi:10.1183/13993003.congress-2024.OA985

17. Bankhead P, Loughrey MB, Fernández JA, Dombrowski Y, McArt DG, Dunne PD, et al. QuPath: Open source software for digital pathology image analysis. Sci Rep. 2017 Dec 4;7(1). doi:10.1038/s41598-017-17204-5

18. Cell Detection with Star-Convex Polygons. In: Lecture Notes in Computer Science [Internet]. Cham: Springer International Publishing; 2018 [cited 2025 Jul 26]. p. 265–73. Available from: https://link.springer.com/10.1007/978-3-030-00934-2_30 doi:10.1007/978-3-030-00934-2_30

19. Adams TS, Schupp JC, Poli S, Ayaub EA, Neumark N, Ahangari F, et al. Single-cell RNA-seq reveals ectopic and aberrant lung-resident cell populations in idiopathic pulmonary fibrosis. Sci Adv. 2020 Jul 10;6(28):eaba1983. doi:10.1126/sciadv.aba1983

20. Habermann AC, Gutierrez AJ, Bui LT, Yahn SL, Winters NI, Calvi CL, et al. Single-cell RNA sequencing reveals profibrotic roles of distinct epithelial and mesenchymal lineages in pulmonary fibrosis. Sci Adv. 2020 Jul 1;6(28):eaba1972. doi:10.1126/sciadv.aba1972 PubMed PMID: 32832598.

21. Valenzi E, Tabib T, Papazoglou A, Sembrat J, Trejo Bittar HE, Rojas M, et al. Disparate Interferon Signaling and Shared Aberrant Basaloid Cells in Single-Cell Profiling of Idiopathic Pulmonary Fibrosis and Systemic Sclerosis-Associated Interstitial Lung Disease. Front Immunol. 2021 Mar 30;12:595811. doi:10.3389/fimmu.2021.595811 PubMed PMID: 33859634; PubMed Central PMCID: PMC8042271.

22. Mayr CH, Santacruz D, Jarosch S, Bleck M, Dalton J, McNabola A, et al. Spatial transcriptomic characterization of pathologic niches in IPF. Sci Adv. 2024 Aug 9;10(32):eadl5473. doi:10.1126/sciadv.adl5473

23. Svobodová B, Löfdahl A, Kadefors M, Mohamed Ali S, Rosmark O, Prabhala P, et al. Collagen VII Is Associated with Airway Remodeling, Honeycombing, and Fibroblast Foci in Usual Interstitial

Pneumonia/Idiopathic Pulmonary Fibrosis. Am J Pathol. 2025 Aug;195(8):1467–83. doi:10.1016/j.ajpath.2025.03.013

24. Uthaya Kumar DB, Motakis E, Yurieva M, Kohar V, Martinek J, Wu TC, et al. Bronchial epithelium epithelial-mesenchymal plasticity forms aberrant basaloid-like cells in vitro. Am J Physiol-Lung Cell Mol Physiol. 2022 Jun 1;322(6):L822–41. doi:10.1152/ajplung.00254.2021

25. Wu B, Shichino S, Ueha S, Matsukiyo R, Ishimura Y, Ogiwara H, et al. Ex vivo lung-organoid model for aberrant basaloid cell induction and activation. Inflamm Regen. 2025 Oct 30;45(1):33. doi:10.1186/s41232-025-00396-z

26. Schupp JC, Adams TS, Cosme C, Raredon MSB, Yuan Y, Omote N, et al. Integrated Single-Cell Atlas of Endothelial Cells of the Human Lung. Circulation. 2021 Jul 27;144(4):286–302. doi:10.1161/CIRCULATIONAHA.120.052318 PubMed PMID: 34030460; PubMed Central PMCID: PMC8300155.

27. Tsukui T, Sun KH, Wetter JB, Wilson-Kanamori JR, Hazelwood LA, Henderson NC, et al. Collagen-producing lung cell atlas identifies multiple subsets with distinct localization and relevance to fibrosis. Nat Commun. 2020 Apr 21;11(1):1920. doi:10.1038/s41467-020-15647-5

28. Belperio JA, Weigt SS, Fishbein MC, Lynch JP. Chronic Lung Allograft Rejection: Mechanisms and Therapy. Proc Am Thorac Soc. 2009 Jan 15;6(1):108–21. doi:10.1513/pats.200807-073GO

29. Estenne M, Hertz MI. Bronchiolitis Obliterans after Human Lung Transplantation. Am J Respir Crit Care Med. 2002 Aug 15;166(4):440–4. doi:10.1164/rccm.200201-003PP

30. Lang NJ, Gote-Schniering J, Porras-Gonzalez D, Yang L, De Sadeleer LJ, Jentzsch RC, et al. Ex vivo tissue perturbations coupled to single-cell RNA-seq reveal multilineage cell circuit dynamics in human lung fibrogenesis. Sci Transl Med. 2023 Dec 6;15(725):eadh0908. doi:10.1126/scitranslmed.adh0908 PubMed PMID: 38055803.

31. Lorenz EC, Hickson LJ, Khairallah P, Najafi B, Kennedy CC. Cellular Senescence and Frailty in Transplantation. Curr Transplant Rep. 2023 Jun;10(2):51–9. doi:10.1007/s40472-023-00393-6 PubMed PMID: 37576589; PubMed Central PMCID: PMC10414789.

32. Ackermann M, Werlein C, Plucinski E, Leypold S, Kühnel MP, Verleden SE, et al. The role of vasculature and angiogenesis in respiratory diseases. Angiogenesis. 2024 Apr 5. doi:10.1007/s10456-024-09910-2 PubMed PMID: 38580869.

33. Schupp JC, Manning EP, Chioccioli M, Kamp JC, Christian L, Ryu C, et al. Alveolar Vascular Remodeling in Nonspecific Interstitial Pneumonia: Replacement of Normal Lung Capillaries with COL15A1-Positive Endothelial Cells. Am J Respir Crit Care Med. 2023 Oct 1;208(7):819–22. doi:10.1164/rccm.202303-0544LE PubMed PMID: 37552025; PubMed Central PMCID: PMC10563189.

34. Denzer L, Muranyi W, Schroten H, Schwerk C. The role of PLVAP in endothelial cells. Cell Tissue Res. 2023 May;392(2):393–412. doi:10.1007/s00441-023-03741-1

35. Wijk A, Wisniewska-Kruk J, Vogels IMC, Veen HA, Ip WF, Wel NN, et al. Expression patterns of endothelial permeability pathways in the development of the blood-retinal barrier in mice. FASEB J. 2019 Apr;33(4):5320–33. doi:10.1096/fj.201801499RRR

36. Piper PJ, Vane JR, Wyllie JH. Inactivation of Prostaglandins by the Lungs. Nature. 1970 Feb;225(5233):600–4. doi:10.1038/225600a0

37. Montero MA, Osadolor T, Khiroya R, Salcedo MT, Robertus JL, Rice A, et al. Restrictive allograft syndrome and idiopathic pleuroparenchymal fibroelastosis: do they really have the same histology? Histopathology. 2017 Jun;70(7):1107–13. doi:10.1111/his.13171

38. Braubach P, Werlein C, Verleden SE, Maerzke I, Gottlieb J, Warnecke G, et al. Pulmonary Fibroelastotic Remodelling Revisited. Cells. 2021 Jun 1;10(6):1362. doi:10.3390/cells10061362

39. Mayr CH, Sengupta A, Asgharpour S, Ansari M, Pestoni JC, Ogar P, et al. Sfrp1 inhibits lung fibroblast invasion during transition to injury-induced myofibroblasts. Eur Respir J. 2024 Feb;63(2):2301326. doi:10.1183/13993003.01326-2023 PubMed PMID: 38212077; PubMed Central PMCID: PMC10850614.

40. Valenzi E, Bulik M, Tabib T, Morse C, Sembrat J, Trejo Bittar H, et al. Single-cell analysis reveals fibroblast heterogeneity and myofibroblasts in systemic sclerosis-associated interstitial lung disease. Ann Rheum Dis. 2019 Oct;78(10):1379–87. doi:10.1136/annrheumdis-2018-214865 PubMed PMID: 31405848; PubMed Central PMCID: PMC7255436.

41. Ruiz-Villalba A, Romero JP, Hernandez SC, Vilas-Zornoza A, Fortelny N, Castro-Labrador L, et al. Single-cell RNA-seq analysis reveals a crucial role for Collagen Triple Helix Repeat Containing 1 (CTHRC1) cardiac fibroblasts after myocardial infarction. Circulation. 2020 Nov 10;142(19):1831–47. doi:10.1161/CIRCULATIONAHA.119.044557 PubMed PMID: 32972203; PubMed Central PMCID: PMC7730974.

42. Gur C, Wang SY, Sheban F, Zada M, Li B, Kharouf F, et al. LGR5 expressing skin fibroblasts define a major cellular hub perturbed in scleroderma. Cell. 2022 Apr 14;185(8):1373-1388.e20. doi:10.1016/j.cell.2022.03.011 PubMed PMID: 35381199; PubMed Central PMCID: PMC7612792.

43. Sheppard D. Integrin-mediated activation of latent transforming growth factor beta. Cancer Metastasis Rev. 2005 Sep;24(3):395–402. doi:10.1007/s10555-005-5131-6 PubMed PMID: 16258727.

44. Lancaster L, Cottin V, Ramaswamy M, Wuyts WA, Jenkins RG, Scholand MB, et al. Bexotegrast in Patients with Idiopathic Pulmonary Fibrosis: The INTEGRIS-IPF Clinical Trial. Am J Respir Crit Care Med. 2024 Aug 15;210(4):424–34. doi:10.1164/rccm.202403-0636OC PubMed PMID: 38843105; PubMed Central PMCID: PMC11351797.

45. Sacreas A, von der Thüsen JH, van den Bosch TPP, Weynand B, Verbeken EK, Debbaut C, et al. The pleural mesothelium and transforming growth factor-β1 pathways in restrictive allograft syndrome: A pre-clinical investigation. J Heart Lung Transplant Off Publ Int Soc Heart Transplant. 2019 May;38(5):570–9. doi:10.1016/j.healun.2019.02.001 PubMed PMID: 30819647.

46. Morrone C, Smirnova NF, Jeridi A, Kneidinger N, Hollauer C, Schupp JC, et al. Cathepsin B promotes collagen biosynthesis, which drives bronchiolitis obliterans syndrome. Eur Respir J. 2021 May;57(5):2001416. doi:10.1183/13993003.01416-2020 PubMed PMID: 33303550.

Figure Legends:

Figure 1: Transcriptomic profiling of human RAS lungs using snRNA-seq.

A: Overview of experimental design. Tissue samples of 15 restrictive allograft syndrome (RAS) lung explants from patients undergoing lung re-transplantation and from 9 donor control lungs were used. The lung tissues were mechanically and enzymatically dissociated, followed by the isolation of nuclei from the dissociated samples. Clean single nuclei suspensions were obtained through flow-activated nuclei sorting (FANS) using 4',6-Diamidino-2-phenylindol (DAPI). For snRNA-seq library preparation, 10x Genomics' Chromium Next GEM technology for multiplexed fixed samples was employed. The prepared libraries were sequenced using the Illumina platform. Subsequent computational analysis was performed to explore and validate the snRNA-seq data. Histological validation and spatial localization were achieved through immunofluorescence, RNA *in situ* hybridization, combined Elastica van Gieson-immunohistochemistry stains, and micro-CT scans. **B**: Uniform Manifold Approximation and Projection (UMAP) representation of 105,952 single nuclei obtained from 15 RAS, and 9 control donor lungs. Each dot represents a single nucleus. Nuclei are labeled as one of 19 distinctive cell types in the left UMAP: epithelial cells (AT1, AT2, aberrant basaloid, basal, ciliated and secretory cells), endothelial cells (aerocytes, vascular endothelial (VE) arterial, VE gCapillary, VE lymphatic, VE systemic, and VE venous cells), and stromal cells (fibroblasts (alveolar, adventitial, fibrotic, and inflamed alveolar), mesothel, pericytes, and smooth mu scle cells). Additionally, nuclei are labeled by disease status (top right), and subject (bottom right) where each color depicts a distinct subject. **C**: Heat map of the average marker gene expression per cell type. Gene expression values are unity normalized from 0 to 1. **D**: Correlation matrix of all identified cell populations of this dataset and of analogous

parenchymal cell types of the IPF atlas(19). Matrix cells are colored by Spearman's rho. Annotation bars (RAS or IPF) denote the origin dataset of each cell population.

Figure 2: snRNA-seq analysis reveals aberrant basaloid cells in RAS lungs.

A: UMAPs of 40,390 epithelial single nuclei from 15 RAS, and 9 control donor lungs, labeled by cell type (upper UMAP), disease (bottom left), and subject (bottom right) where each color depicts a distinct subject. **B**: Boxplots representing the percent makeup distributions of each epithelial cell type among all identified epithelial cells organized by disease group. Whiskers represent 1.5 × interquartile range (IQR). Statistical significance was defined at three levels: $p < 0.05$: *, $p < 0.01$: **, and $p < 0.001$: ***. Aberrant basaloid cells are significantly increased ($p < 0.001$) in RAS compared to control lungs. Detailed results of unadjusted Wilcoxon rank sum test comparing RAS and control proportions are reported in supplemental table E2H. **C**: Stacked bar plots representing the frequency (in %) of each epithelial cell type among all identified epithelial cells per subject. Each bar represents a different subject (15 RAS and 9 control subjects). Stacked bars are ordered by increasing frequencies of aberrant basaloid cells. **D**: Heat map representing characteristics of the six identified epithelial cell types. Expression values are centered and scaled across subjects. Each column shows the average expression per subject and disease state. Each subject is represented by a unique color, and disease state and epithelial cell type are represented in the colored annotation bars above.

Figure 3: IF validation reveals aberrant basaloid cells localized at the fibrotic edge.

IF and corresponding EvG stains of three different RAS specimens. Split channels are depicted in supplemental figures E2–E7. Stains of control lungs are depicted in supplemental figures E8–E11. **A–C:** Scale bar of overviews (top rows of A–C) are 1000 µm. Scale bars of close-up views (bottom rows of A–C) are 100 µm. Arrows indicate aberrant basaloid cells identified based on the combined staining patterns of *KRT17*, *CTSE*, *integrin αvβ6*, *COX2*, and *TP63* within the same microanatomical region – the fibrotic edge - across the respective panels. IF stains demonstrate their preferential localization at the fibrotic edge and partial expansion into the alveolar space and AFE areas. In proximity to the fibrotic edge, multiple "obliterating alveoli" (air-containing structures in fibrotic areas) are observed. They show a heterogeneous cellular composition, typically including aberrant basaloid cells, and variably also *SFTPC*$^{+}$/*KRT17*$^{+}$ transitional cells and *LAMP*$^{+}$/*AGER*$^{+}$ AT1 cells. In concordance with our transcriptomic data, IF stains show no bronchiolization. EvG stains confirm the AFE pattern in RAS. Dashed black lines serve as guides for the identification of the fibrotic edge. **D:** IF stains of control lungs, showing a bronchiole with *KRT17*$^{+}$/*TP63*$^{+}$ basal cells. Scale bars are 100 µm.

Figure 4: Identification of increased *COL15A1*$^{+}$ peribronchial vascular endothelial cells in RAS.

A: UMAPs of 27,657 endothelial single nuclei from 15 RAS, and 9 control donor lungs, labeled by cell type (upper UMAP), disease (bottom left), and subject (bottom right) where each color depicts a distinct subject. **B**: Boxplots representing the percent distributions of each endothelial cell type among all identified endothelial cells organized by disease group. Whiskers represent 1.5 × interquartile range (IQR). Statistical significance was defined at three levels: $p < 0.05$: *, $p < 0.01$: **, and $p < 0.001$: ***. COL15A1^{+} peribronchial vascular

endothelial cells (pVECs) are significantly increased ($p < 0.05$) in RAS compared to control lungs. Detailed results of unadjusted Wilcoxon rank sum test comparing RAS and control proportions are reported in supplemental table E2H. **C**: Stacked bar plots representing the frequency (in %) of each endothelial cell type among all identified endothelial cells per subject. Each bar represents a different subject (15 RAS and 9 control subjects). Stacked bars are ordered by increasing frequencies of *COL15A1*$^{+}$ pVECs. **D**: Heat map representing marker gene expression of the six identified endothelial cell types. Gene expression is unity normalized between 0 and 1 across endothelial cells. Each column shows individual cell average marker gene expression per subject and disease state. Each subject is represented by a unique color, and disease state and endothelial cell type are represented in the colored annotation bars above.

Figure 5: Localization of *COL15A1*$^{+}$ peribronchial vascular endothelial cells in RAS.

A–C: IF stains of three different RAS specimens. Scale bars are 100 µm. Split channels are depicted in supplemental figures E12–E14. Stains of control lungs are depicted in supplemental figures E15–E17. Arrows in *CD31/COL15A1* and *CD31/PLVAP* panels indicate *CD31*$^{+}$*/COL15A1*$^{+}$*/PLVAP*$^{+}$ (ectopic) peribronchial vascular endothelial cells (pVECs). PVECs occur in high frequencies in AFE areas. They also expand into the alveoli, where they partially replace the physiologic *CD31*$^{+}$*/PRX*$^{+}$ microvasculature (arrows in *CD31/PRX* panels indicate physiologic alveolar capillaries). **D–F**: EvG-IHC stains of RAS specimens corresponding to the IF stains in A–C. Scale bars are 100 µm. Arrows indicate *CD31*$^{+}$ VE cells and *COL15A1*$^{+}$ ectopic pVECs. Positive staining aligns with the observations made in A–C. EvG-IHC staining show that ectopic pVECs in AFE regions lack spatial connections to former alveolar septa or other

physiological structures, suggesting a neoangiogenic potential. Dashed black lines serve as guides for the identification of the fibrotic edge. **G**: Micro-CT imaging of subpleural RAS remodeling. 3D reconstruction of the tissue specimen shows a dense zone of subpleural fibrotic consolidation. Tungsten contrasting does not contrast fibrotic tissue. Virtual sectioning of the block indicates pronounced sprouting of vasculature-like structures within the subpleural fibrosis. Morphologically, vascular structures seem to originate from the pleura, as cross sections of the observed vessels rejuvenate with increasing distance from the pleura. EvG-IHC staining of a RAS specimen. Scale bar is 500 µm. Arrows indicate *CD31*$^{+}$ VE cells, confirming vascular-like structures seen in micro-CT scans as vessels. The combination with *COL15A1* targeted IHC-EvG stains reveals that these vessels are mostly (ectopic) pVECs.

Figure 6: Identification and localization of *CTHRC1*$^{+}$ fibrotic fibroblasts in RAS.

A: UMAPs of 37,905 stromal single nuclei from 15 RAS, and 9 control donor lungs, labeled by cell type (upper UMAP), disease (bottom left), and subject (bottom right) where each color depicts a distinct subject. **B:** Boxplots representing the nonzero percent makeup distributions of each stromal cell type among all identified stromal cells organized by disease group. Whiskers represent 1.5 × interquartile range (IQR). RAS and control cell type frequencies were compared using the Wilcoxon rank sum test (for detailed results, see Suppl. table E2H). Statistical significance was defined at three levels: $p < 0.05$: *, $p < 0.01$: **, and $p < 0.001$: ***. Alveolar fibroblasts are significantly decreased (unadjusted $p < 0.01$) in RAS compared to control lungs and *CTHRC1+* fibrotic fibroblasts are significantly increased (unadjusted $p < 0.001$) in RAS compared to control lungs. **C**: Stacked bar plots representing the frequency (in %) of each stromal cell type among all identified stromal cells per subject. Each bar

represents a different subject (15 RAS and 9 control subjects). Stacked bars are ordered by increasing frequencies of *CTHRC1*$^{+}$ fibrotic fibroblasts. **D**: Heat map representing the marker gene expression of the seven identified stromal cell types. Gene expression is unity normalized between 0 and 1 across stromal cells. Each column shows average gene expression per subject and disease state. Each subject is represented by a unique color, and disease state and stromal cell type are represented in the colored annotation bars above. **E**: Heat map of differentially expressed genes comparing RAS and controls in *CTHRC1*$^{+}$ fibrotic fibroblasts, hierarchically clustered. Average expression values are scaled across subjects. Each subject is represented by a unique color, and disease state and cell type are represented in the colored annotation bars above. **F**: Pathway analysis of 15 RAS and 9 control specimens. Depicted are average enrichment scores per cell type and disease state. Enrichment scores are unity normalized between 0 and 1 across all identified cells types. Cell type and disease status are indicated by the colored annotation bars above. **G–I**: RNA-ISH staining of 3 different RAS specimens. Scale bar of overviews (top row) are 1000 µm. Scale bars of close-up views (bottom row) are 100 µm. Split channels are depicted in supplemental figures E18–E20. Stains of control lungs are depicted in supplemental figures E21. *CTHRC1*$^{+}$*/COL1A1*$^{+}$ cells represent *CTHRC1*$^{+}$ fibrotic fibroblasts which are distributed across all parts of AFE areas and form small nests in fibrotically thickened alveolar septa.

Figure 7: Graphical summary of aberrant and ectopic cells in RAS.

A: Schematic illustration of healthy lung tissue. Upper illustration shows the mesothelial coated pleura, and subpleural lung tissue including *COL15A1*$^{+}$ vessels near the pleura, alveoli, elastin fibers in alveolar septa, AT1 and AT2 cells, and *PRX*$^{+}$ capillaries. Bottom illustration

shows healthy lung tissue including a bronchus and its corresponding bronchial artery, peribronchial *COL15A1*$^{+}$ vessels, alveoli, elastin fibers in alveolar septa, AT1 and AT2 cells, and *PRX+* capillaries. **B:** Schematic overview illustration of RAS lung tissue. It shows characteristic elements of RAS such as a thickened pleura, areas of AFE, vasculature-like structures within the subpleural fibrosis reaching into AFE areas and rejuvenating with increasing distance from the pleura, *COL15A1*$^{+}$ vessels near the pleura and ectopic *COL15A1*$^{+}$ vessels in areas of AFE and in alveolar septa where they partially replace *PRX*$^{+}$ capillaries, a decreased amount of *PRX+* capillaries, *CTHRC1*$^{+}$ fibrotic fibroblasts in areas of AFE and sporadically in small nests in thickened alveolar septa in more distal RAS tissue, aberrant basaloid cells lining the active edge of the fibrotic edge in a monolayer and lining thickened alveolar septa, and enriched elastic fibers in thickened alveolar septa. **C:** Schematic close-up illustration of RAS lung tissue. It shows characteristic elements of RAS such as AFE, ectopic *COL15A1*$^{+}$ vessels in areas of AFE and in alveolar septa where they partially replace *PRX*$^{+}$ capillaries, a decreased amount of *PRX*$^{+}$ capillaries, *CTHRC1*$^{+}$ fibrotic fibroblasts in areas of AFE, aberrant basaloid cells lining the active edge of the fibrotic edge in a monolayer and lining thickened alveolar septa, obliterating alveoli near the fibrotic edge consisting of either aberrant basaloid cells, *SFTPC*$^{+}$*/KRT17*$^{+}$ transitional cells, and *LAMP*$^{+}$*/AGER*$^{+}$ AT1 cells, all of which being pathologically *CTSE*$^{+}$, and enriched elastic fibers in thickened alveolar septa.

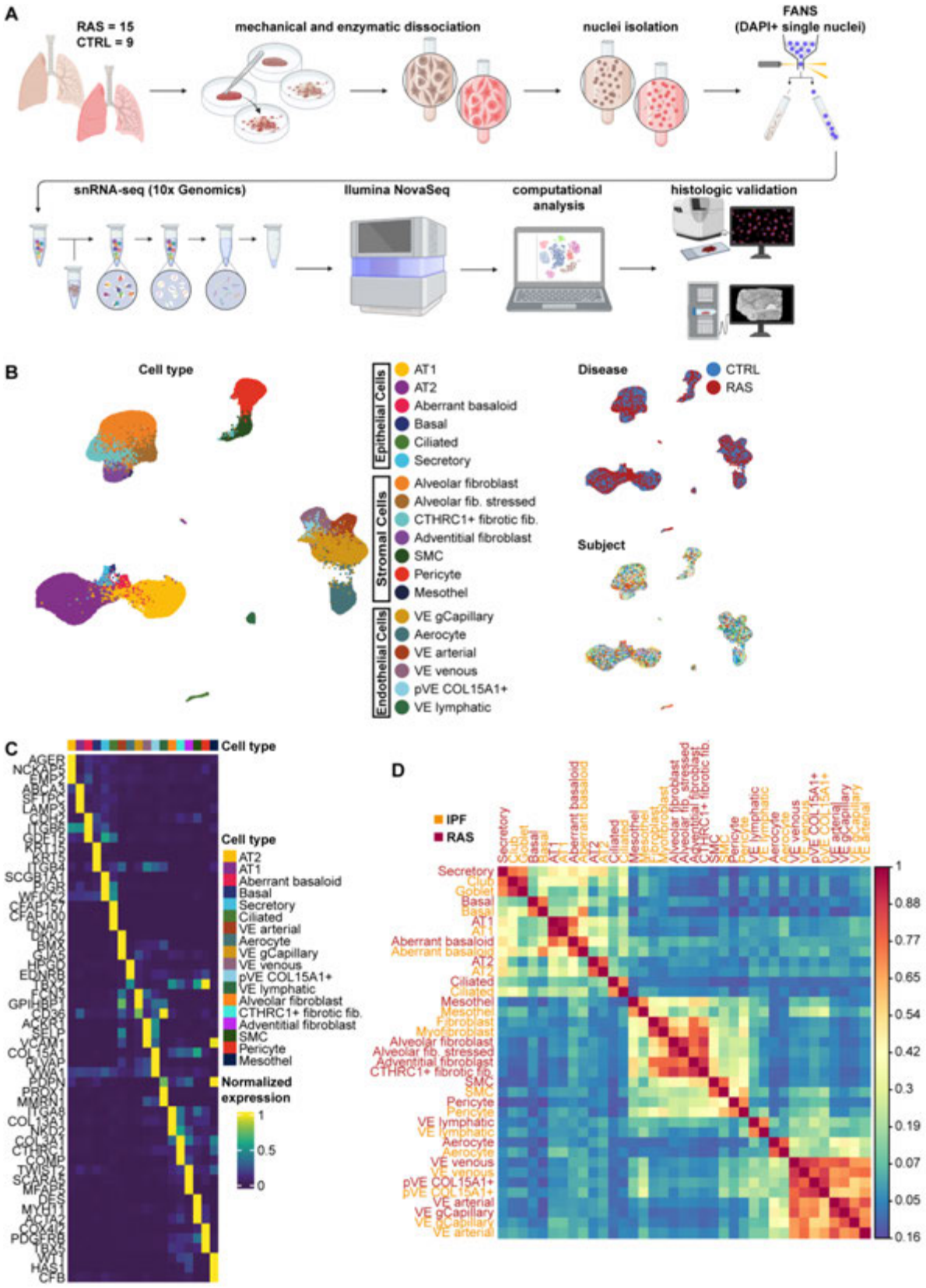

Figure 1

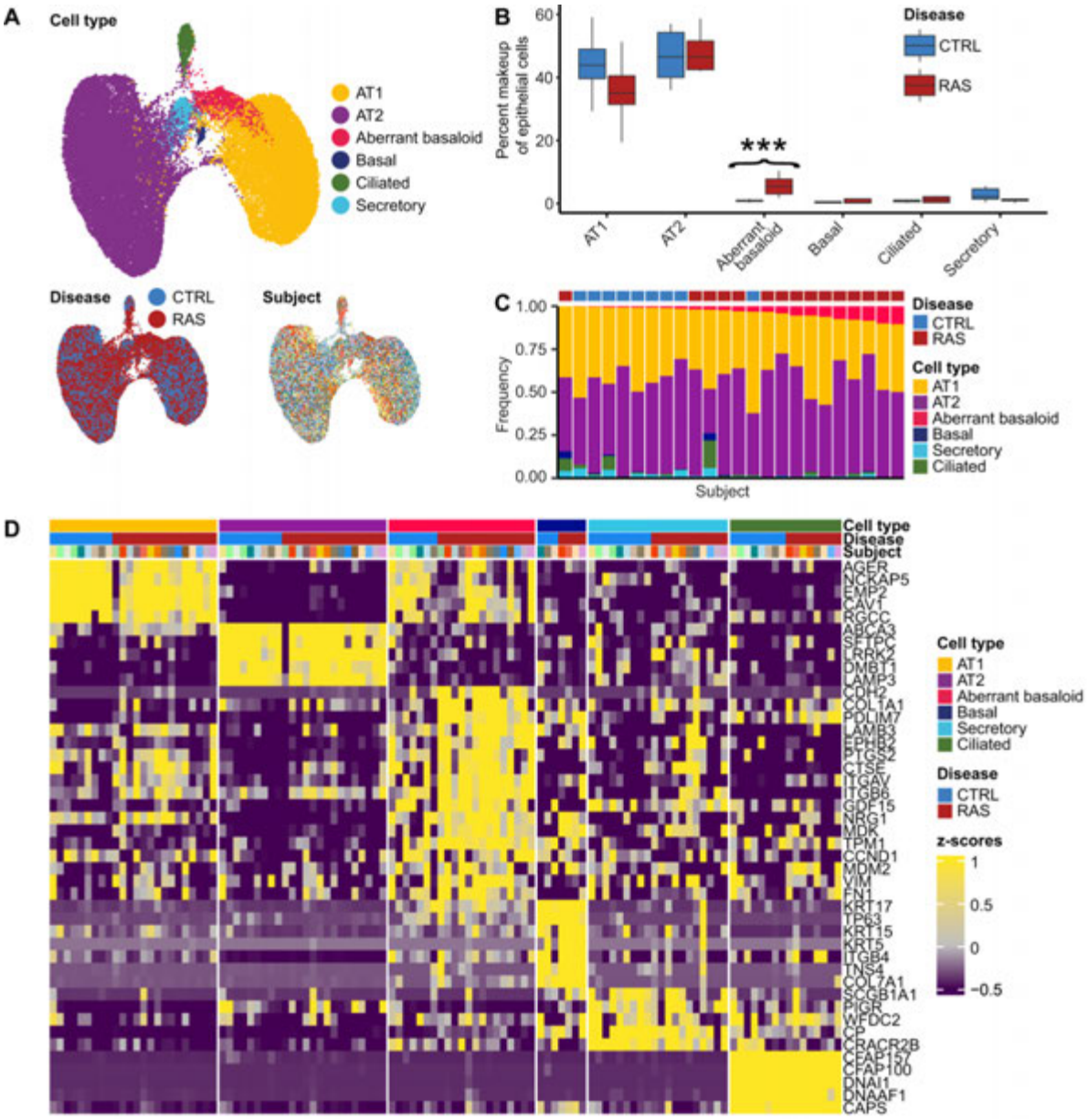

Figure 2

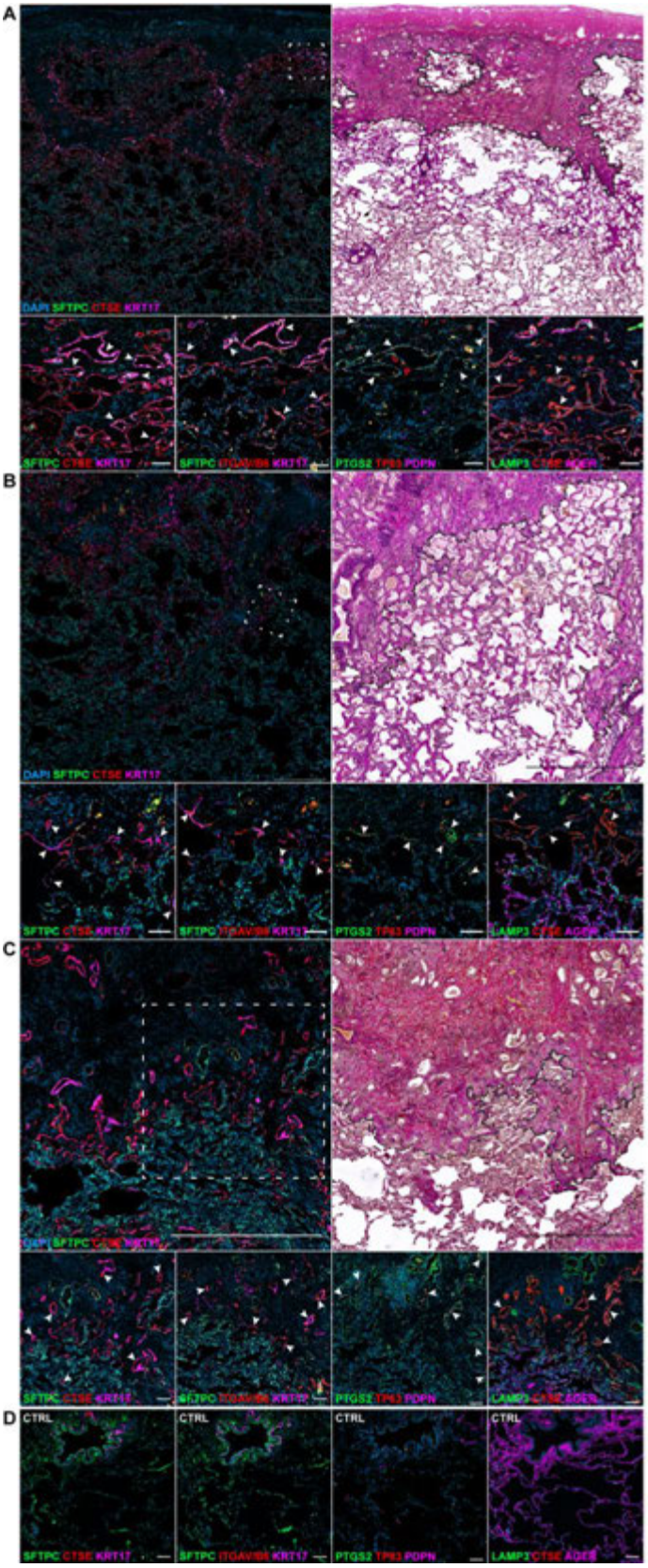

Figure 3

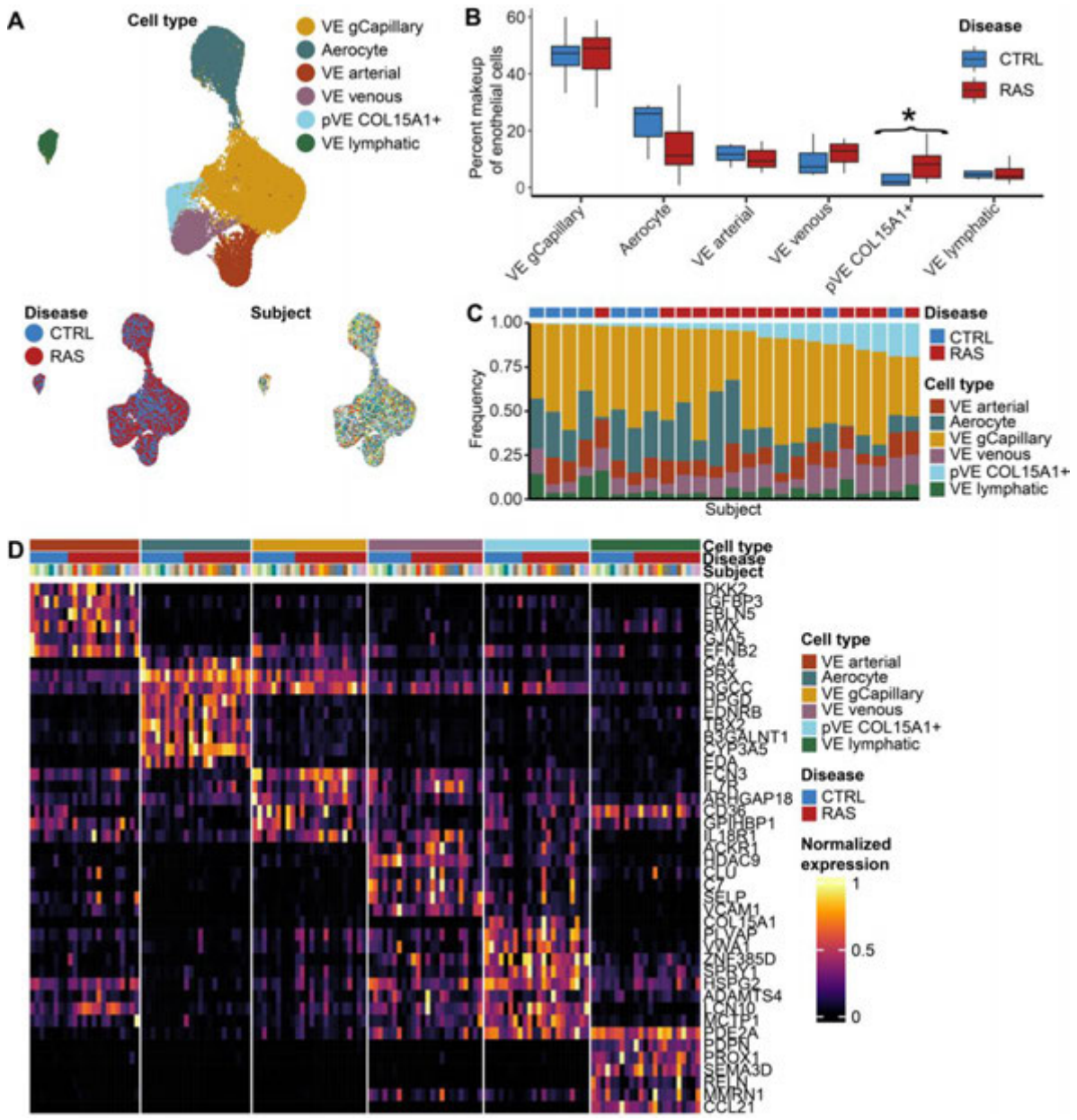

Figure 4

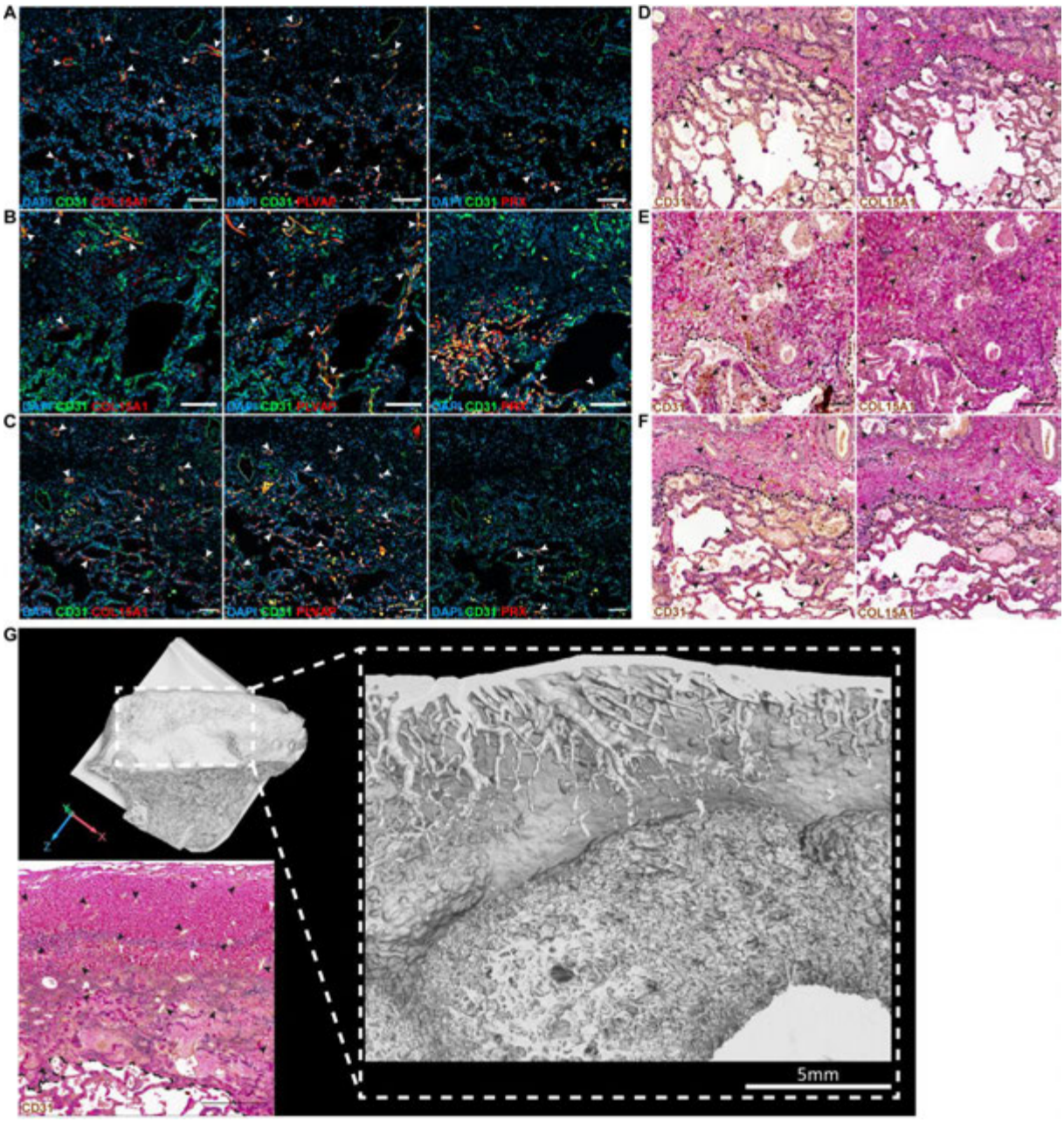

Figure 5

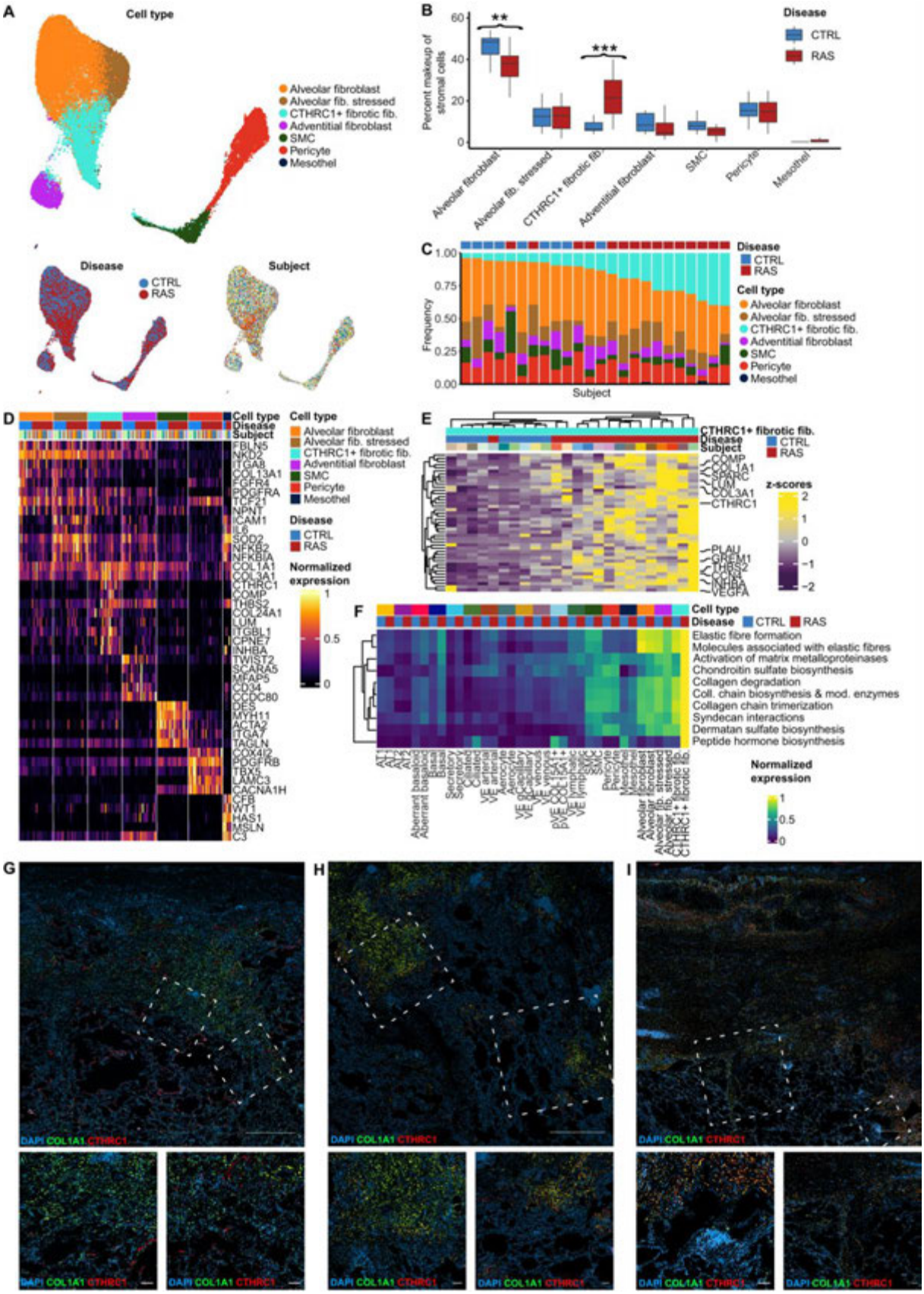

Figure 6

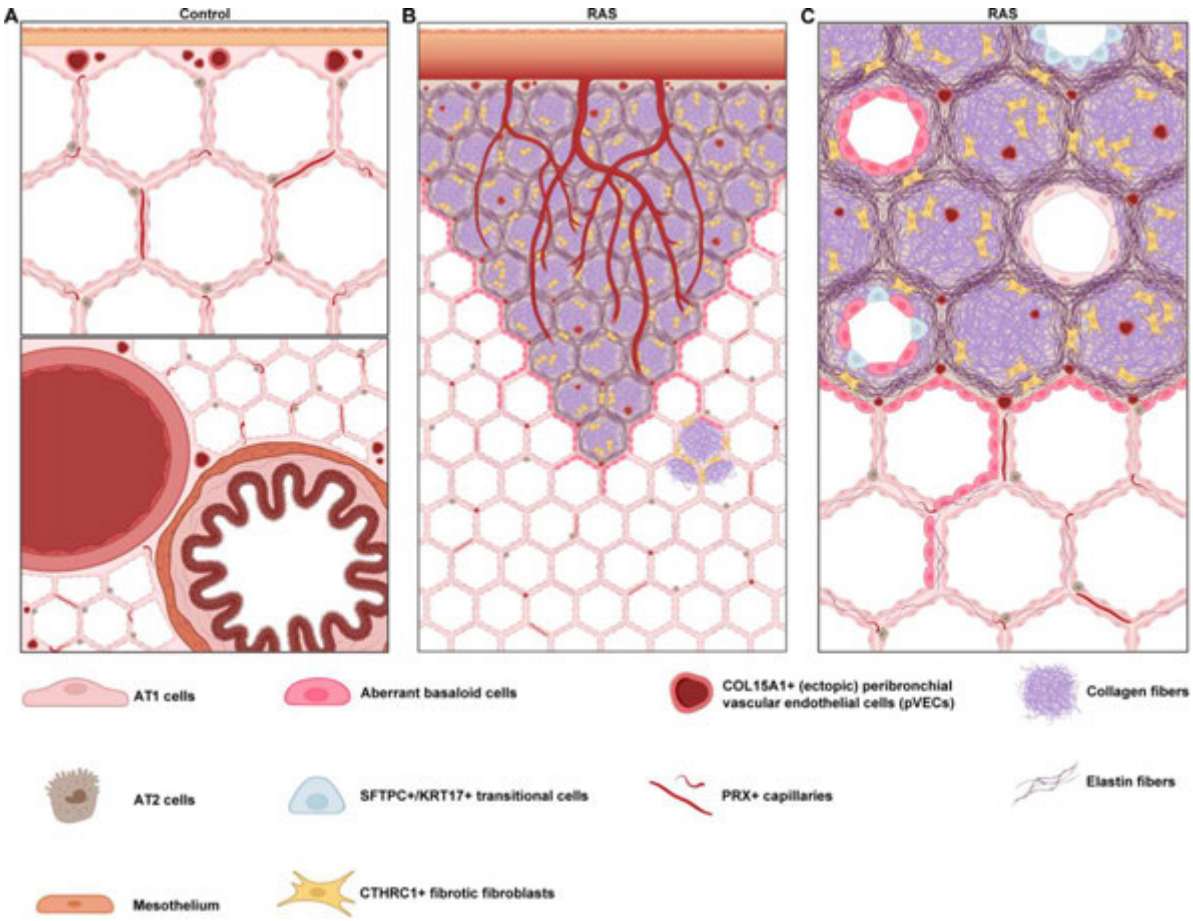

Figure 7

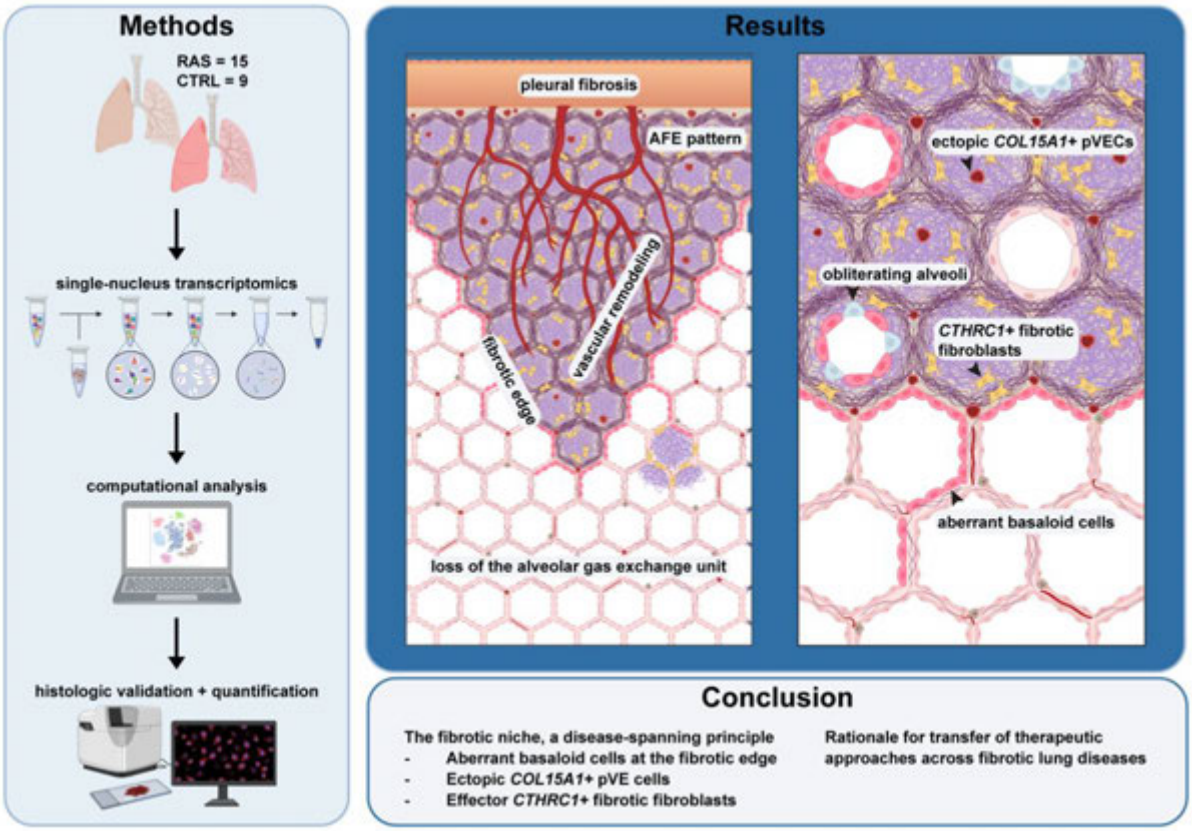

Graphical abstract

Online Data Supplement

Aberrant and Ectopic Cell Populations in Restrictive Allograft Syndrome after Lung Transplantation

Lena M. Leiber[1,2], Leonard Christian[1,2], Lavinia Neubert[2,3], Jannik Ruwisch[1,2], Hande Yilmaz[1,2], Edith K. J. Plucinski[2,3], Linus T. Langer[1,2], Jan C. Kamp[1,2,3], Mark Greer[1,2], Bernd Haermeyer[4], Mark Kühnel[2,5], Christopher Werlein[2,3], Aurelien Justet[6], Anke K. Bergmann[4], Hanne Beeckmans[7], Matthias Ballmaier[8], Jawad Salman[9], Robin Vos[7], Lars Knudsen[10], Ulrich Martin[2,9,11], Bart M. Vanaudenaerde[7], Ali Önder Yildirim[12], Jens M. Hohlfeld[1,2,13], Fabio Ius[2,9], Florian Laenger[5], Tobias Welte[1,2,†], Christine Falk[2,14], Naftali Kaminski[15], Danny D. Jonigk[2,3,5*], Jens Gottlieb[1,2*], Jonas C. Schupp[1,2,13,15*]

†Died March 10th, 2024

*Contributed equally

Methods:

Selection of RAS specimens for snRNA-seq

All CLAD specimens available at the biobank of Medical School Hanover (MHH) are phenotyped according to the latest ISHLT guidelines.(5) Formalin-fixed peripheral lung tissue from the upper lobe from 15 explant lungs from the department of pathology at MHH were used.

Nuclei isolation for Chromium Fixed RNA Profiling (Multiplexed Samples)

Under a biological safety hood, each specimen was transferred into a plastic Petri dish on ice and minced into small pieces (~1 mm^3) using a scalpel. The specimens were then transferred on ice into gentleMACS™ C Tubes (Miltenyi Biotec, Bergisch Gladbach, Germany; Cat# 130-093-237).

The fixation buffer was freshly prepared by mixing 100 µL 10× Fix & Perm Buffer (10x Genomics, Pleasanton, CA, USA; Cat# 2000517), 108.1 µL 37 % formaldehyde solution (Sigma-Aldrich, St. Louis, MO, USA; Cat# F8775), and 791.9 µL nuclease-free water (Life Technologies, Waltham, MA, USA; Cat# AM9937) per 1 mL total volume. 1 mL of fixation buffer was added to each sample. Samples were incubated for 16–24 h at 4 °C. After fixation, samples were centrifuged at 850 × *g* for 5 minutes at room temperature (RT). The supernatant was carefully removed without disturbing the tissue pellet, which was often very loose. Subsequently, 2 mL of ice-cold phosphate-buffered saline (PBS) (Thermo Fisher Scientific, Waltham, MA, USA; Cat# 10010023) containing 0.04 % bovine serum albumin (BSA) (Sigma-Aldrich, St. Louis, MO, USA; Cat# 126615-25ML) was added. The tissue pellet was gently resuspended as needed using wide-bore pipette tips (Eppendorf, Hamburg, Germany; Cat# 990452).

A second centrifugation step was performed under the same conditions. The supernatant was removed without disturbing the pellet. On ice, 1 mL Tissue Resuspension Buffer (containing 0.496× PBS + 50 mM Tris-HCl, pH 8.0 ((Thermo Fisher Scientific, Waltham, MA, USA; Cat# AM9856)) + 0.02 % BSA + 0.24 U/µL RNase Inhibitor (Sigma-Aldrich Chemie GmbH, Taufkirchen, Germany; Cat# 3335402001), and nuclease-free water) was added to each sample and gently resuspended using wide-bore tips. Samples were centrifuged at 850 × *g* for 5 min at RT using a swinging-bucket rotor. Supernatants were removed without disturbing the tissue pellets.

Meanwhile, 2 mL per specimen of freshly prepared Tissue Digestion Buffer was pre-warmed at 37 °C in a water bath for 10 minutes, then added to each sample. The buffer contained 250 µg/mL Liberase™ TM (Sigma-Aldrich, St. Louis, MO, USA; Cat# 5401127001), 2.5 mg/mL Collagenase D (Sigma-Aldrich, St. Louis, MO, USA; Cat# 11088882001), and 0.5 mM $CaCl_2$ (Jena Bioscience, Jena, Germany; Cat# BU-103), prepared in 1× PBS (from 10× PBS; Life Technologies, Waltham, MA, USA; Cat# AM9624) and filled up to volume with nuclease-free water (Life Technologies, Waltham, MA, USA; Cat# AM9937).For dissociation, a gentleMACS™ Octo Dissociator with heaters was used with the following program: Incubation for 45 min at 50 rpm, 37 °C, followed by spinning for 30 sec at (+)2000 rpm, 37 °C and 30 sec at (-)2000 rpm, 37 °C. Before running the program, it was confirmed that no tissue pieces remained attached to the inner walls of gentleMACS™ C Tubes and that all tissue pieces were fully resuspended in Tissue Digestion Buffer. After dissociation, gentleMACS™ C Tubes were detached and centrifuged at 300 × *g* for 30 sec (swinging-bucket rotor) to collect all tissue pieces at the bottom of the gentleMACS™ C Tubes. Each pellet was resuspended in its supernatant using wide-bore tips (Eppendorf, Hamburg, Germany; Cat# 990452). To remove undissociated tissue pieces and debris, each specimen was passed through a 70 µm filter (pluriSelect Life Science

UG, Leipzig, Germany; Cat# 43-50070-03) into a pre-cooled 50 mL conical tube. Each filter and gentleMACS™ C Tube was rinsed with a total of 2 mL 1× PBS. Filtrates were collected in the respective 50 mL conical tubes. Samples were centrifuged at 850 × *g* for 5 min at 4 °C using a swinging-bucket rotor. Supernatants were removed without disturbing the pellets. Each pellet was resuspended in 1 mL Concentrated Quenching Buffer (10x Genomics, Pleasanton, CA, USA; Cat# 1000414, 2000516). To enrich for intact nuclei and reduce debris and aggregates, samples were passed through pluriStrainer Mini 20 µm filters (pluriSelect Life Science UG, Leipzig, Germany; Cat# 43-5020-20) into 1.5 mL LoBind tubes. Nuclei concentrations were measured using a LUNA-FL™ Dual Fluorescence Cell Counter with Acridine Orange/Propidium Iodide Stain (AO/PI) (Logos Biosystems, Anyang-si, South Korea; Cat# LBS-AF008). The Enhancer (10x Genomics, Pleasanton, CA, USA; Cat# 1000414, 2000482) was warmed at 65 °C for 10 min, vortexed briefly, and centrifuged. A volume corresponding to 10% of each sample's volume was added to each sample, followed by gentle mixing. Samples were stored at 4 °C for up to one week.

Fluorescence Activated Nuclei Sorting (FANS) of DAPI$^+$ single nuclei

For flow cytometric sorting of nuclei, specimens were stained with 4',6-diamidino-2-phenylindole (DAPI) (Life Technologies, Waltham, MA, USA; Cat# D1306) immediately before sorting. The final DAPI concentration ranged between 1 and 10 µg/mL and was adjusted as needed to achieve saturated nuclear staining. Sorting was performed at the Central Research Facility Cell Sorting of MHH using cell sorters equipped with a 100 µm nozzle at 35 psi (FACSAria III Fusion, FACSAria IIu Becton-Dickinson, or MoFlo XDP, Beckman-Coulter). 5×10^5 DAPI$^+$ single nuclei per specimen were sorted into individual 15 mL tubes, each containing

1 mL of 0.5× PBS supplemented with 0.02 % BSA. Intact single nuclei were identified based on their light-scattering properties and DNA content, as measured by DAPI fluorescence. A narrow gate was applied in the DAPI channel to include only intact nuclei and to exclude debris (Fig. E1A). In further gating steps, doublets were excluded using Forward Scatter (FSC) pulse parameters (Fig. E1B), and the main population was further refined in an FSC–SSC (Side Scatter) gate (Fig. E1C). Reanalysis of 300 sorted nuclei per specimen showed a homogeneous nuclear population (Fig. E1D). Sorted single nuclei suspensions were kept on ice and processed immediately for downstream analysis once 16 specimens were sorted, following the Chromium Fixed RNA Profiling Reagent Kits for Multiplexed Samples (10x Genomics) protocol.

10x Genomics Chromium Fixed RNA Profiling for Multiplexed Samples

Sorted $DAPI^+$ single nuclei were immediately further processed using the Chromium Fixed RNA Profiling Reagent Kits for Multiplexed Samples (10x Genomics, Pleasanton, CA, USA), following the instructions in the user guide (CG000527, Rev B). The protocol was applied with the following specific choices and deviations: Multiplexing experiment design “Maximize Number of Cells” without sub-pooling and post-hybridization pooled wash workflow was chosen for all specimens. Hybridization was performed in PCR tube-strips. Due to upfront sorting of 500,000 $DAPI^+$ single nuclei per specimen and in order to minimize nuclei loss, the first counting step during post-hybridization was not performed. Further, all specimens (16 specimens/pool) were completely pooled because the absolute number of nuclei was estimated to be still nearly the same across all specimens due to FANS. Before passing the sample pool through a 20 µm filter (pluriSelect Life Science UG, Leipzig, Germany; Cat# 43-5020-20), the nuclei pellet was only resuspended in 25 % of the volume stated in the protocol to achieve a high nuclei

concentration without having to concentrate nuclei suspension after counting them (step "Cell Suspension Volume Calculator for Multiplexing 16 Samples"). 128000 nuclei were chosen as "Targeted Cell Recovery" but a 20 % higher volume of nuclei suspension stock/reaction than stated was used for the previous determined nuclei concentration and was filled up to 40 µL with Concentrated Post-Hyb Resuspension Buffer (10x Genomics, Pleasanton, CA, USA; Cat# 1000476, 2000533). For the Sample Index PCR, a total of 12 cycles was appropriate. Three different QC-approaches per library were performed for post library construction: first a 1:20 dilution of stock library and Buffer EB (QIAGEN, Hilden, Germany; Cat# 19086) was prepared of which 5 µL were used to determine a Qubit quantification of the 1:20 diluted library. Therefore, Qubit™ 1X dsDNA Assay-Kits (HS) + (BR) (Thermo Fisher Scientific, Waltham, MA, USA; Cat# Q33231), Qubit™ assay tubes (Thermo Fisher Scientific, Waltham, MA, USA; Cat# Q32856) and a Qubit™ 4 Fluorometer (Thermo Fisher Scientific, Waltham, MA, USA; Cat# Q33226) were used. Afterwards, 5 µL of each 1:20 diluted library were forwarded to the Research Core Unit Genomics (RCUG) at MHH to perform a DNA fragment length analysis (HS) and a Qubit quantification. Additionally, a qPCR was performed for each library using the KAPA Library Quantification Kit for Illumina® Platforms (Roche Diagnostics, Mannheim, Germany; Cat# 07960140001; Protocol KR0405 – v11.20) following their detailed protocol. Remaining stock libraries and 1:20 diluted libraries were stored at -20 °C.

Sequencing; data processing and analysis

cDNA libraries were sequenced on an Illumina NovaSeq 6000 platform at the Department of Human Genetics (Hanover Medical School, Germany), aiming for 800 million reads per library with a sequencing configuration of 28 base pairs on read1, 90 base pairs on read2, and 10

base pairs on Index5 and Index7, respectively. Basecalls were converted to reads using the software Cell Ranger (v7.1.0) and its bcl2fastq implementation “mkfastq”.

Read processing. Subsequent read processing was conducted using the software Cell Ranger (v7.1.0). Reads of probes were aligned to the human reference genome GRCh38 (GENCODE v32/Ensembl 98, “GRCh38-2020-A”) using the Chromium Human Transcriptome Probe Set _v1.0.1 for GRCh38-2020-A. Technical summaries on sequencing and data processing can be accessed in supplemental table E2.

Dataset integration. Dataset integration was performed as described previously(21). Nuclei-UMI count matrices were analyzed using the R package Seurat (version 4.3.0). UMI counts were normalized with a scale factor of 10,000 UMIs per nucleus and then natural log transformed using a pseudocount of 1. To discern structural lung cells from immune cells, a recursive process of integration, graph embedding, and cluster analysis was employed. Each iteration involved integrating subjects and clustering, following Seurat's recommended approach utilizing reciprocal PCA (https://satijalab.org/seurat/articles/integration_rpca.html). Initially, the top variable genes per subject were identified through Seurat's FindVariableFeatures using the "vst" parameter. Patterns of shared variance in these genes in respective subjects were then utilized to integrate the datasets using Seurat's FindIntegrationAnchors and IntegrateData functions, followed by scaling the resulting integrated expression matrix with Seurat's ScaleData.

Dimension reduction, graph embedding, clustering and visualization. Dimension reduction for visualizing and clustering was performed in a stepwise process, as performed previously (13,21). Scaled values from the integration approach underwent principal component analysis (PCA), with selected principal components chosen based on their contribution to variance.

Respective principal components were then used to estimate Euclidean distances between nuclei in feature-space, leading to graph embedding where edges connected the nearest neighbors for each nucleus. Louvain clustering was then applied to this network of connected nuclei. For visualization, nuclei distances and their graph embeddings underwent uniform manifold approximation and projection (UMAP). Clusters that showed no significant differences in gene expression were merged. This iterative process was continued until all nuclei from all subjects could be assigned to a discrete cell type whose characteristic features were consistently represented in all subjects. After the comprehensive categorization of all cells into different cell type clusters, we then determined the respective lineage assignment of each cluster based on the expression profile of the following classical lineage markers: CDH5 and PECAM1 for endothelial, MUC1 and KRT7 for epithelial, PDGFRA and PDGFRB for mesenchymal, and PTPRC for immune cells. Mesothelial were grouped together with the mesenchymal cells. As this project focused on structural cells of the RAS lungs, immune cells were excluded from downstream analyses. Multiplets and other cell barcodes of subpar quality were flagged based on their transcriptomic profiles resembling a combination of two or more distinct cell type signatures already present in the dataset. This scrutiny extended to the entire dataset and all lineage subsets. Barcodes flagged as multiplets or of low quality were excluded from subsequent analyses.

Identification of cell type specific marker genes. Cell-type specific marker genes were identified using the Wilcoxon rank sum test by comparing all cells within a specific cluster to all other cells, as implemented by Seurat's FindMarkers function. All p-values were adjusted for multiple testing using the Bonferroni correction. An adjusted p-value below 0.05 was considered significant. To evaluate our cell type annotation, we downloaded the IPF cell atlas data from GEO (GSE136831). Average gene expression of the top five marker genes by logFC

per annotated cell type population was calculated in the RAS and the IPF dataset. Only genes shared between both datasets were considered. Spearman correlation coefficients were calculated pairwise between the average cell-type profiles using the base R function “cor”. The resulting correlation matrix was visualized using the R package corrplot.

Availability of sequencing data. The processed raw data of this study has been deposited on GEO under the accession number GSE284081.

Primary antibodies and Secondary antibodies

All primary antibodies and secondary antibodies for immunofluorescent stains used in this study were extensively validated prior to application. Validation steps included testing on multiple appropriate control tissues and across a range of dilutions to ensure optimal specificity and signal-to-noise ratio. For each staining protocol (immunohistochemistry (IHC), immunofluorescence (IF), and combined Elastica van Gieson (EvG) and IHC stains), both positive and negative technical controls were routinely performed.

Negative controls for IF and IHC included omission of the primary antibody. Positive controls consisted of tissues known to express the target antigen or RNA transcript. All antibody stainings were independently assessed by at least three investigators, one of whom is a board-certified pathologist, to ensure reproducibility and consistency of staining patterns. Furthermore, the antigen specificity of all antibodies was cross-checked with the manufacturer’s data sheets, including reported immunogen sequences, validation data, and known cross-reactivities.

All used antibodies are listed in supplemental table E3. Representative examples of immunofluorescence/RNA in situ hybridization negative control stainings and representative immunohistochemical stainings of all primary antibodies listed in Table E3, as well as the secondary antibodies used for immunohistochemistry in this study are included in the Supplement (Supplementary Figures E22 and E27) to illustrate the specificity and reliability of the employed staining protocols.

Immunohistochemistry (IHC)

IHC was performed to test the functionality and accuracy of primary antibodies. IHC was performed on 3 µm thick sections of FFPE lung tissue. Before starting, all reagents were equilibrated to RT. A standard deparaffinization and rehydration of FFPE tissue was performed (2× 5 min xylene, 2× 3 min 100 % ethanol, 1× 3 min 95 % ethanol, 1× 1min 70 % ethanol, 1× 1 min 50 % ethanol, 1× 5 min distilled water), followed by heat-induced antigen retrieval. Therefore, tissue slides were boiled for 20 min at 98 °C in 1× Tris-Based Antigen Unmasking Solution (Vector Laboratories, Burlingame, CA, USA; Cat# H-3301), diluted 1:100 with distilled water. After letting specimens cool for 20 min, they were washed in 1× PBS for 5 min. Tissue sections were encircled with a Roth®-Liquid Barrier Marker (Carl Roth GmbH + Co. KG, Karlsruhe, Germany; Cat# AN 92.1) and put into a wet chamber which was used to store slides during all further incubation steps. Specimens were incubated for 10 min in BLOXALL Endogenous Peroxidase and Alkaline Phosphatase Blocking Solution (Vector Laboratories, Burlingame, CA, USA; Cat# VEC-SP-6000) in order to block endogenous peroxidase and alkaline phosphatase activity. Tissue slides were washed for 5 min in 1× PBS and blocked for 20 min using 2.5 % Normal Horse Serum Blocking Solution (Vector Laboratories, Burlingame, CA, USA;

Cat# S-2012-50). Each specimen was incubated for 30 min with a primary antibody (diluted appropriately in 2.5 % Normal Horse Serum Blocking Solution) at RT. After washing the tissue slides in 1× PBS for 5 min, each specimen was incubated for 30 min with a corresponding secondary antibody (anti-mouse, anti-rabbit or anti-goat ImmPRESS reagent (Vector Laboratories, Burlingame, CA, USA; Cat# MP-7402; Cat# MP-7401; Cat# MP-7405)) at RT. Slides were washed once again for 5 min in 1× PBS, then incubated for 6–10 min in ImmPACT® DAB Substrate Kit, Peroxidase (HRP) (Vector Laboratories, Burlingame, CA, USA; Cat# SK-4105). Incubation times varied due to each individual reaction times. After one last wash for 5 min in 1× PBS, specimens were counterstained in Hematoxylin Solution Gill no. 1 (Morphisto GmbH, Frankfurt am Main, Germany; Cat# 10216.00100) for 3 min, then washed for 15 min in tap water (intermittent exchange of tap water). Afterwards, a standard dehydration in ethanol/xylene was performed (1× 15 sec 50 % ethanol, 1× 15 sec 70 % ethanol, 1× 1 min 95 % ethanol, 2× 1 min 100 % ethanol, 2× 3 min xylene). Tissue slides were mounted with VectaMount® PT Permanent Mounting Medium (Vector Laboratories, Newark, CA, USA; Cat# VEC-H-5000) and coverslips were put on. Stained slides were digitalized and analyzed using a ZEISS Axioscan 7 and the ZEN 3.5 (blue edition) software. Slides were stored at RT.

Immunohistofluorescent (IF) stains

IF stains were performed on 3 µm thick sections of FFPE lung tissue. Before starting, all reagents were equilibrated to RT. A standard deparaffinization and rehydration of FFPE tissue was performed (2× 5 min xylene, 2× 3 min 100 % ethanol, 1× 3 min 95 % ethanol, 1× 1 min 70 % ethanol, 1× 1 min 50 % ethanol, 1× 5 min distilled water), followed by heat-induced antigen retrieval. Therefore, FFPE tissue slides were boiled for 20 min at 98 °C in 1× Tris-Based

Antigen Unmasking Solution (Vector Laboratories, Burlingame, CA, USA; Cat# H-3301), diluted 1:100 with distilled water. Afterwards specimens were cooled down for 20 min in 1× PBS at RT. Meanwhile, a stock of 0.9995× PBS + 0.05 % Tween® 20 (SERVA Electrophoresis GmbH, Heidelberg, Germany; Cat# 39796.01) was prepared and used to prepare 2.5 % normal serum (donkey (Linaris GmbH, Dossenheim, Germany; Cat# END9000-100)/horse (Vector Laboratories, Burlingame, CA, USA; Cat# S-2012-50)) corresponding to the secondary antibodies' species. All primary and secondary antibodies were diluted in suitable 2.5 % normal serum and stored at RT under aluminum foil until needed. After letting the slides cool down, they were encircled with a Roth®-Liquid Barrier Marker (Carl Roth GmbH + Co. KG, Karlsruhe, Germany; Cat# AN 92.1) and put into a wet chamber which was used to store slides during all further incubation steps. Specimens were incubated for 20 min with 2.5 % normal serum before gently tapping the slides sideways on paper towels to remove normal serum. No washing step was performed at this point. Each specimen was incubated for 60 min with the prepared solution of 2.5 % normal serum and primary antibody/antibodies at RT. Slides were washed for 2× 3 min in PBS containing 0.05 % Tween® 20. Specimens were incubated for 60 min with the prepared solution of 2.5 % normal serum and secondary antibody/antibodies under aluminum foil at RT. Slides were washed in staining troughs covered with aluminum foil for 2× 3 min in PBS containing 0.05 % Tween® 20. Specimens were incubated for 60 min with the prepared solution of 2.5 % normal serum and fluorochrome conjugated antibody/antibodies under aluminum foil at RT. Slides were washed in staining troughs covered with aluminum foil for 2× 3 min in PBS containing 0.05 % Tween® 20. Vector TrueView Autofluorescence Quenching Kit (Vector Laboratories, Newark, CA, USA; Cat# SP-8400) was used according to the manufacturer's information before washing slides in staining troughs covered with aluminum foil for 5 min in PBS containing 0.05 % Tween® 20. Slides were

mounted with VECTASHIELD Vibrance™ with DAPI Antifade Mounting Medium (Vector Laboratories, Newark, CA, USA; Cat# H-1800-2) and coverslips were put on. Stained slides were digitalized and analyzed using a ZEISS Axioscan 7 and the ZEN 3.5 (blue edition) software. Slides were stored darkly at 4 °C.

Hematoxylin-eosin (HE) stains

HE stains were performed on 3 µm thick sections of FFPE lung tissue. Before starting, all reagents were equilibrated to RT. A standard deparaffinization and rehydration of FFPE tissue was performed (2× 5 min xylene, 2× 3 min 100 % ethanol, 1× 3 min 95 % ethanol, 1× 1 min 70 % ethanol, 1× 1 min 50 % ethanol, 1× 5 min distilled water). Slides were incubated with 2:1 Hematoxylin solution Gill no. 1 (Sigma-Aldrich, St. Louis, MO, USA; Cat# GHS116) for 5 min. Afterwards, slides were washed for 15 min in tap water (intermittent exchange of tap water), then rinsed for 2 min with distilled water. Slides were incubated for 3 min in an Eosin G ready-to-use solution (Carl Roth GmbH + Co. KG, Karlsruhe, Germany; Cat# X883.1), then briefly rinsed with distilled water. Afterwards, a standard dehydration in ethanol/xylene was performed (1× 15 sec 50 % ethanol, 1× 15 sec 70 % ethanol, 1× 1 min 95 % ethanol, 2× 1 min 100 % ethanol, 2× 3 min xylene). Tissue slides were mounted with VectaMount permanent mounting solution (Vector Laboratories, Newark, CA, USA; Cat# VEC-H-5000) and coverslips were put on. Stained slides were digitalized and analyzed using a ZEISS Axioscan 7 and the ZEN 3.5 (blue edition) software. Slides were stored at RT.

RNA *in situ* hybridization (RNA-ISH)

RNA-ISH was performed on 3 µm thick sections of FFPE lung tissue and strictly according to the "RNAscope™ Multiplex Fluorescent Reagent Kit v2 User Manual" (UM 323100/Rev B/ Effective Date: 10/11/2022) by ACD bio. Probes listed in supplemental table E4 were used. All probes used in this study were extensively validated prior to application. Further, all stains were independently assessed by at least three investigators, including board-certified pathologists, to ensure reproducibility and consistency of staining patterns. Slides were stored at 4 °C in the dark until scanning. Stained slides were digitalized and analyzed using a ZEISS Axioscan 7 and the ZEN 3.5 (blue edition) software.

Elastica van Gieson (EvG) stains

EvG stains were performed on 3 µm thick sections of FFPE lung tissue. A standard deparaffinization and rehydration of FFPE tissue was performed (90 sec xylene, 90 sec 100 % ethanol, 90 sec 90 % ethanol, 90 sec 70 % ethanol). Afterwards, specimens were incubated for 10 min in Resorcinol-Fuchsine-solution according to Weigert (Waldeck GmbH & Co KG, Münster, Germany; Cat# 2E-030), then differentiated for 2× 30 sec in 100 % ethanol. Specimens were incubated for 10 min with iron hematoxylin solution according to Weigert (Waldeck GmbH & Co. KG, Münster, Germany; Cat# 2E-032, 2E-052), followed by bluing for 5 min in tap water. Slides were stained for 15 sec in picrofuchsin solution according to van Gieson (Waldeck GmbH & Co KG, Münster, Germany; Cat# 2E-050) before dehydrating them (5 sec 70 % ethanol, 90 sec 90 % ethanol, 2× 90 sec 100 % ethanol, 90 sec xylene). Stained slides were digitalized and analyzed using a ZEISS Axioscan 7 and the ZEN 3.5 (blue edition) software. Slides were stored at RT.

Combined Elastica van Gieson (EvG) and Immunohistochemistry (IHC) stains

Combined EvG and IHC stains were performed on 3 µm thick sections of FFPE lung tissue. A standard deparaffinization and rehydration of FFPE tissue was performed (2× 10 min xylene, 2 min 100 % ethanol, 2 min 90 % ethanol, 2 min 70 % ethanol, 2 min 50 % ethanol, 2 min demineralized water). Then, tissue slides were boiled for 30 min at 98 °C in T-EDTA Buffer pH 9.0 (10×) (Zytomed Systems GmbH, Berlin, Germany; Cat# ZUC029), and washed for 10 min in demineralized water at RT. Tissue sections were encircled with a Roth®-Liquid Barrier Marker (Carl Roth GmbH + Co. KG, Karlsruhe, Germany; Cat# AN 92.1). Antibody staining was performed as follows: 5 min 3 % H_2O_2, 5 min washing buffer (Zytomed Systems GmbH, Berlin, Germany; Cat# ZUC020), 5 min blocking solution(Zytomed Systems GmbH, Berlin, Germany; Cat# POLHRP-100), 5 min washing buffer, 1 h antibody incubation, 5 min washing buffer, 30 min HRP-polymer (Zytomed Systems GmbH, Berlin, Germany; Cat# POLHRP-100), 5 min washing buffer, 15 min DAB (Zytomed Systems GmbH, Berlin, Germany; Cat# DAB057 or DAB530) (1:20 diluted), and 5 min washing in demineralized water. Slides were air-dried. Afterwards, EvG stains were automatically performed according to the EvG staining protocol stated above (but without the deparaffinization/rehydration), using a HistoCore SPECTRA Workstation (Leica Biosystems, Wetzlar, Germany; Workstation-Kit Cat# 14051254355, SPECTRA ST Cat# 14051254354, SPECTRA CV Cat# 14051454200).

Micro-CT

RAS specimens were contrasted using Tungsten phosphoric acid for 48 h, then scanned with a Phoenix Nanotom® M micro-CT scanner (Waygate technologies). A voxel size of 8.46 µm was

acquired employing a x-ray tube potential (peak voltage) of 60 kV given a x-ray intensity current of 540 µA. Micrographs were obtained with an average of 5489 distinct grey scales securing optimized optical contrast. Raw data image processing applying a ROI- and Inline Median was performed prior to final 3D volume rendering, which was conducted with VGSTUDIO 2022 64-Bit Software (Volume Graphics).

Image processing

All histologic images were analyzed and processed using ZEN (blue edition) software by ZEISS. The processing method “background subtraction” was applied to all IF and RNA-ISH images using default settings. White and black values were manually adjusted for each channel. No further image processing methods were used. Multi-panel figures were put together using Adobe Illustrator 2024.

Cell segmentation and machine learning guided quantification

For quantitative image analysis, IF scans were loaded into QuPath (0.5.1). Cell segmentation was carried out based on DAPI stains, employing the StarDist extension, following the recommended QuPath workflow referred to in the docs (“https://qupath.readthedocs.io/en/stable/”). For StarDist-based cell segmentation, percentile normalization was applied using the 1st and 99th percentiles. A probability threshold of 0.5 was set for object detection. The analysis was conducted at a resolution of 0.5 µm per pixel. Detected nuclei were expanded by 5 µm to approximate whole-cell boundaries, with cell expansion constrained to 40% of the nuclear size to avoid

overestimation. Shape descriptors and intensity measurements were calculated across all cellular compartments. Prediction probabilities were included as an additional measurement parameter. Segmented cell masks were subsequently employed for manually defining channel-wise training data for the QuPath inbuilt artificial neural network (ANN) classifier. Approximately 30–50 cells per channel per slide were manually annotated, and ANN training was performed. Channel-related classifications were carefully reviewed and exported to .txt files. Zones of interest (e.g., alveoli = “Alv”, fibrotic edge/border zone = “Border”, dense fibrotic zone = “Remodeled”, non-fibrotic areas = “Not remodeled”) and “obliterating alveoli” were manually segmented and annotated on the same slide. Area size was exported to R, and cell densities per surface unit (µm²) or per cell were calculated. “Obliterating alveoli” were ordered by the relative abundance of *KRT17*$^{-}$/*CTSE*$^{-}$/*SFTPC*$^{-}$ cell populations.

Supplemental Tables:

Table E1:

n	**Control n = 9**	**RAS n = 15**
Female/Male [n]	4/5	6/9
Downsizing/Tumor-distant tissue [n]	5/4	n.a.
Age in years [median, 25 and 75 % percentiles]	57 [54-63]	44 [35 - 55]
FEV1 % baseline [median, 25 and 75 % percentiles]	n.a.	27 [17 - 37]
FVC % baseline [median, 25 and 75 % percentiles]	n.a.	41 [38 - 46]
TLC % baseline [median, 25 and 75 % percentiles]	n.a.	74 [71 - 86]
Immunosuppressive Regimen	n.a.	Tacrolimus (n = 11), Ciclosporin (n = 3), Prednisolone/mycophenolate (n = 15)
Type of previous lung transplantation	n.a.	SLTx n = 0, DLTx n = 15
Radiographic abnormalities	n.a.	subpleural consolidations n = 13, diffuse consolidations
Distribution of radiographic abnormalities	n.a.	apical predominance n = 10; no predominance n = 5
Donor specific antibodies (DSA)	n.a.	no n = 12, yes n = 3

Table E1: **Cohort characteristics**. Basic characteristics of all included control and RAS patients. Continuous variables are depicted as median and interquartile range. Age is given in years. FVC, FEV1 and TLC are calculated as percent of the baseline values, the mean of the best two post-operative measurements. All lung function values show last available lung function pre re-transplantation, FEV1 = forced expiratory volume in 1 second; FVC = forced vital capacity; n.a. = not applicable; TLC = total lung capacity; SLTx = single lung transplantation; DLTx = double lung transplantation.

Table E2: Summary of snRNA-seq analysis details

The data from supplemental table E2 has been deposited on Dryad under the DOI 10.5061/dryad.0cfxpnwd2.

A: Summary of technical summaries of read processing per sample. **B:** Full cohort marker table. Results of Wilcoxon rank-sum test of each cell-type in the whole dataset against the other varieties in the whole dataset per cell type. **C:** Epithelial subset marker table. Results of Wilcoxon rank-sum test of each epithelial cell-type against the other epithelial varieties per cell type. **D:** Endothelial subset marker table. Results of Wilcoxon rank-sum test of each endothelial cell-type against the other endothelial varieties per cell type. **E:** Stromal subset marker table. Results of Wilcoxon rank-sum test of each stromal cell-type against the other stromal varieties per cell type. **F.** Results of Wilcoxon rank-sum test comparing pathway scores of each cell-type in the whole dataset against the other varieties in the whole dataset per cell type. **G:** RAS versus control differential expression table. Results of Wilcoxon rank-sum test per cell type comparing RAS to control. **H:** Cell differential statistics. Frequencies and results of the Wilcoxon rank-sum test comparing RAS versus control cell-type makeup as a fraction of their respective lineage group.

Table E3:

Target	Species	Clonality	Clone	Conjugate	Manufacturer	REF	Dilution IHC	Dilution IF
AGER	Mouse	mono	A11		Santa Cruz	sc-80652	1:200	1:25
Cathepsin E (CTSE)	Rabbit	poly			Sigma Aldrich	HPA012940	1:200	1:100
CD31	mouse	mono	JC70A		Agilent Technologies Sales (DAKO)	M082329-2	1:100	1:50
COL15A1	Rabbit	poly			Thermo Fisher	PA553667	1:600	1:300
COX2	Mouse	mono	COX 229		Thermo Fisher	35-8200	1:100	1:50
ITGAVß6	rabbit	mono	EM05201		Sigma Aldrich	ZRB1104	1:100	1:50
KRT17	mouse	mono	E-4	Alexa Fluor® 647	Santa Cruz	sc-393002 AF647	1:50	1:25
KRT17	Mouse	Mono	E-3		DAKO	M704601-2	1:100	
LAMP3	goat	poly			biotechne/R&D systems	AF4087	1:200	1:200
p63	Mouse	mono	A4A		abcam	ab735	1:100	1:50
P63	Rabbit	mono	TP63/1423R		NSJ bio	V3815-100UG	1:100	1:50
PDPN	Mouse	mono	D2-40	Alexa Fluor® 647	biolegend	916606	1:1000	1:50
PLVAP	Rabbit	mono	E3X9D		Cell Signaling Technology	38238	1:100	1:50
PRX	Rabbit	poly			novus bio	NBP1-89598-25ul	1:400	1:200
SFTPC	Mouse	mono	H8		Santa Cruz	sc-518029	1:200	1:100
Goat-IgG	Donkey	-	-	Alexa Fluor® 488	Biozol	JIM-705-545-147	-	1:200
Mouse-IgG	Horse	-	-	DyLight® 488	Vector Laboratories	DK-8828	-	Ready-to-Use
Mouse-IgG	Donkey	-	-	Alexa Fluor® 647	Life Technologies GmbH	A32787	-	1:200
Rabbit-IgG	Horse	-	-	DyLight® 594	Vector Laboratories	DK-8828	-	Ready-to-Use
Rabbit-IgG	Donkey	-	-	Rhodamine Red™-X	Linaris (Biozol)	JIM-711-295-152	-	1:500

Table E3: Summary of antibodies used for histologic validation. Listed antibodies were used for IHC, IF, and EvG-IHC stains. Further details are available in the corresponding method sections.

Table E4:

Name	**Brand**	**Cat.**
Hs-CTHRC1	Bio-Techne	413331
Hs-COL1A1-C4	Bio-Techne	401891-C4

Table E4: Summary of probes used for RNA *in situ* hybridization. Listed probes were used for RNA *in situ* hybridization. Further details are available in the corresponding method sections.

Supplemental Figures:

Figure E1:

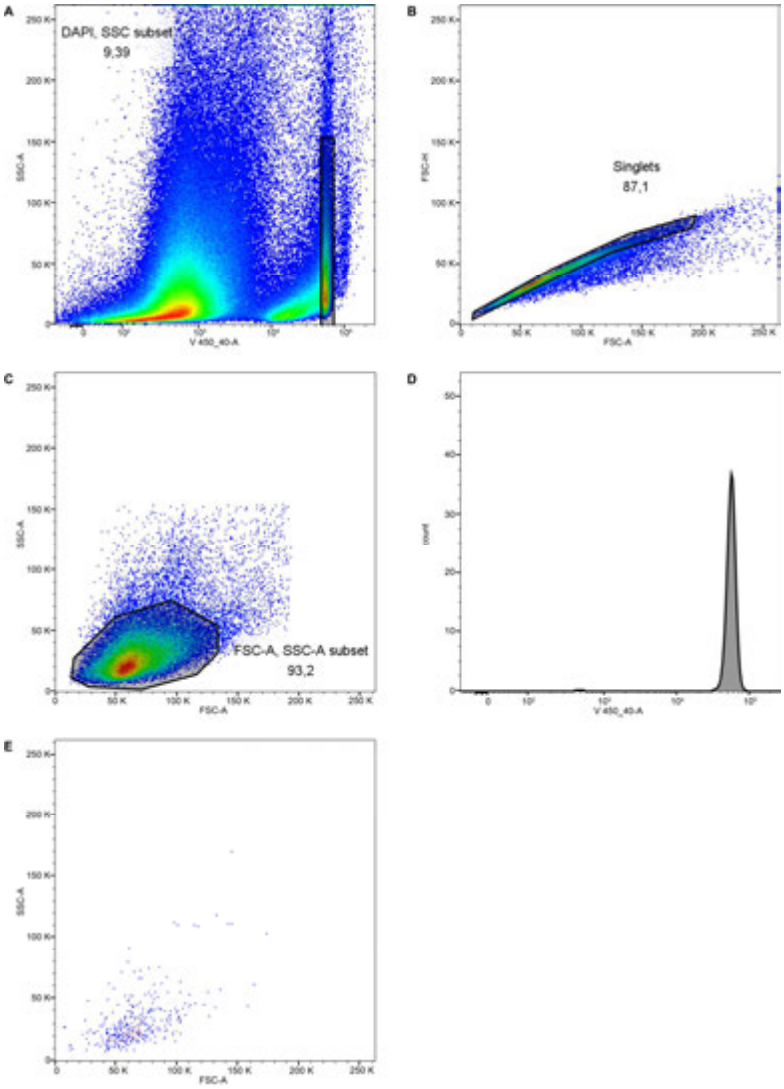

Figure E1: **Overview of the Gating Strategy for Fluorescence-Activated Nuclei Sorting**. For flow cytometric sorting of nuclei specimens were stained with 4',6-diamidino-2-phenylindole (DAPI, Thermo Scientific™) immediately before sorting. **A:** A narrow gate in the DAPI channel was set to include only intact nuclei and to exclude debris. **B:** In further gating steps, doublets were excluded using FSC pulse parameters. **C:** The main population was further narrowed down in a FSC-SSC gate. **D-E:** Reanalysis of 300 sorted nuclei from each specimen showed a homogeneous population of nuclei, which were used for downstream analyses.

Figure E2:

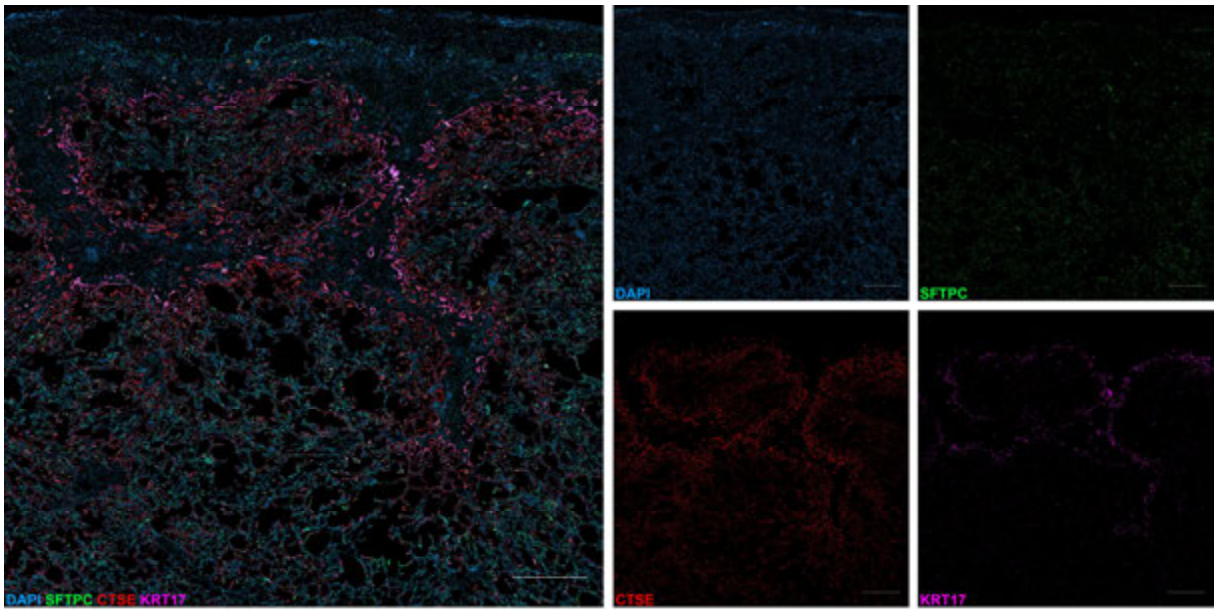

Figure E2: Split channels of epithelial targeted IF stains of RAS lungs. IF stains (split and merged channels) of peripheral RAS lung tissues. Scale bar in the merged channel is 1000 µm and scale bars in split channels are 100 µm. Target cell population: epithelial cells. For detailed information about the stains see figure legend of Fig. 3 A-C in the main manuscript.

Figure E3:

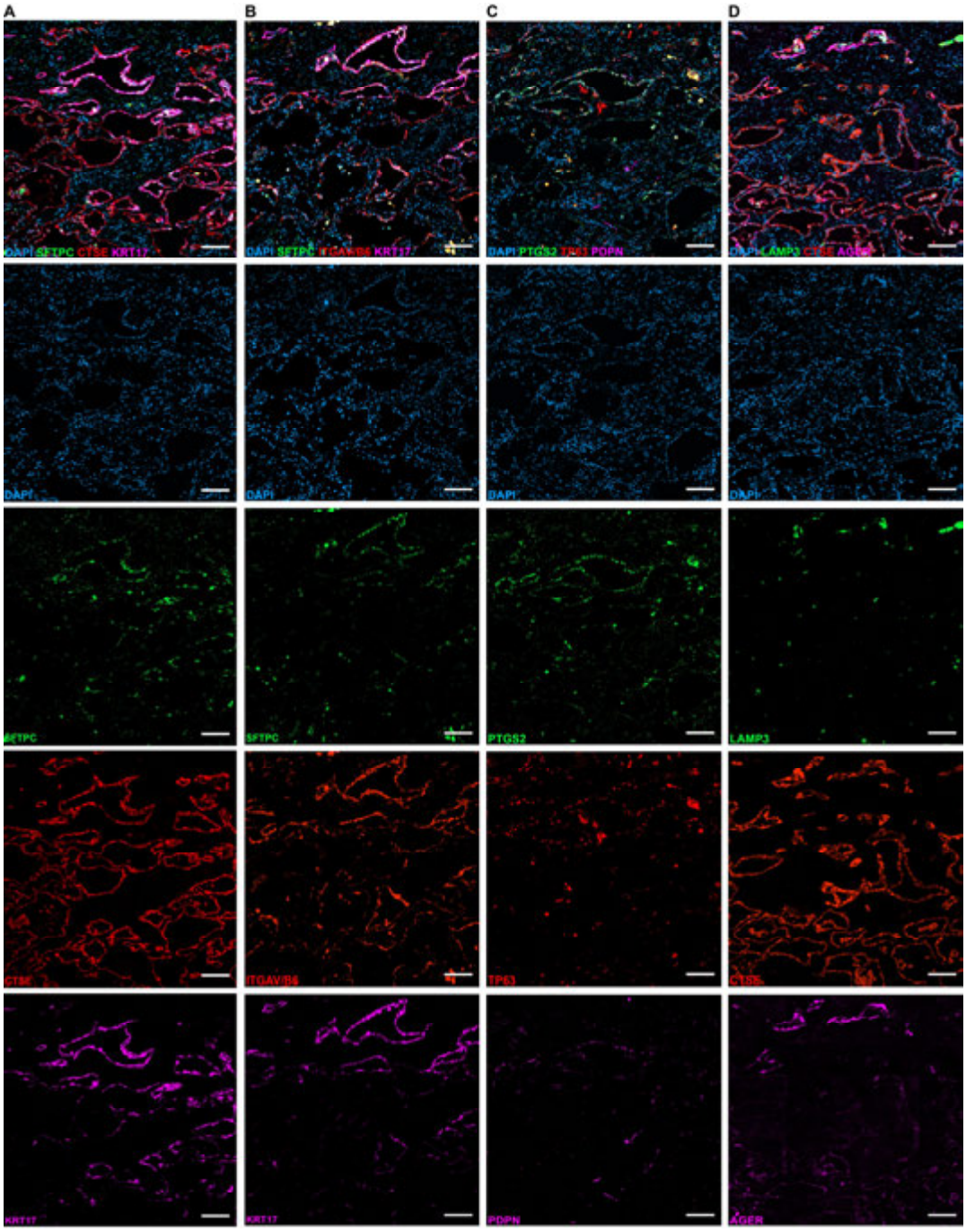

Figure E3: Split channels of epithelial targeted IF stains of RAS lungs. IF stains (split and merged channels) of peripheral RAS lung tissues. Scale bars are 100 µm. Target cell population: epithelial cells. For detailed information about the stains see figure legend of Fig. 3 A-C in the main manuscript.

Figure E4:

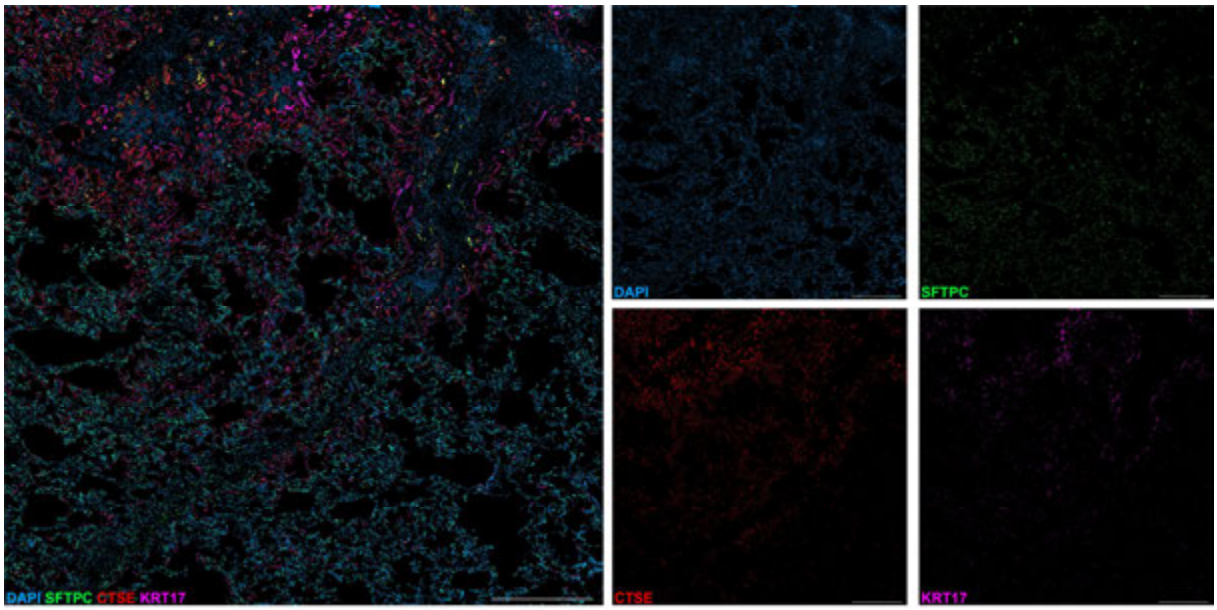

Figure E4: Split channels of epithelial targeted IF stains of RAS lungs. IF stains (split and merged channels) of peripheral RAS lung tissues. Scale bar in the merged channel is 1000 µm and scale bars in split channels are 100 µm. Target cell population: epithelial cells. For detailed information about the stains see figure legend of Fig. 3 A-C in the main manuscript.

Figure E5:

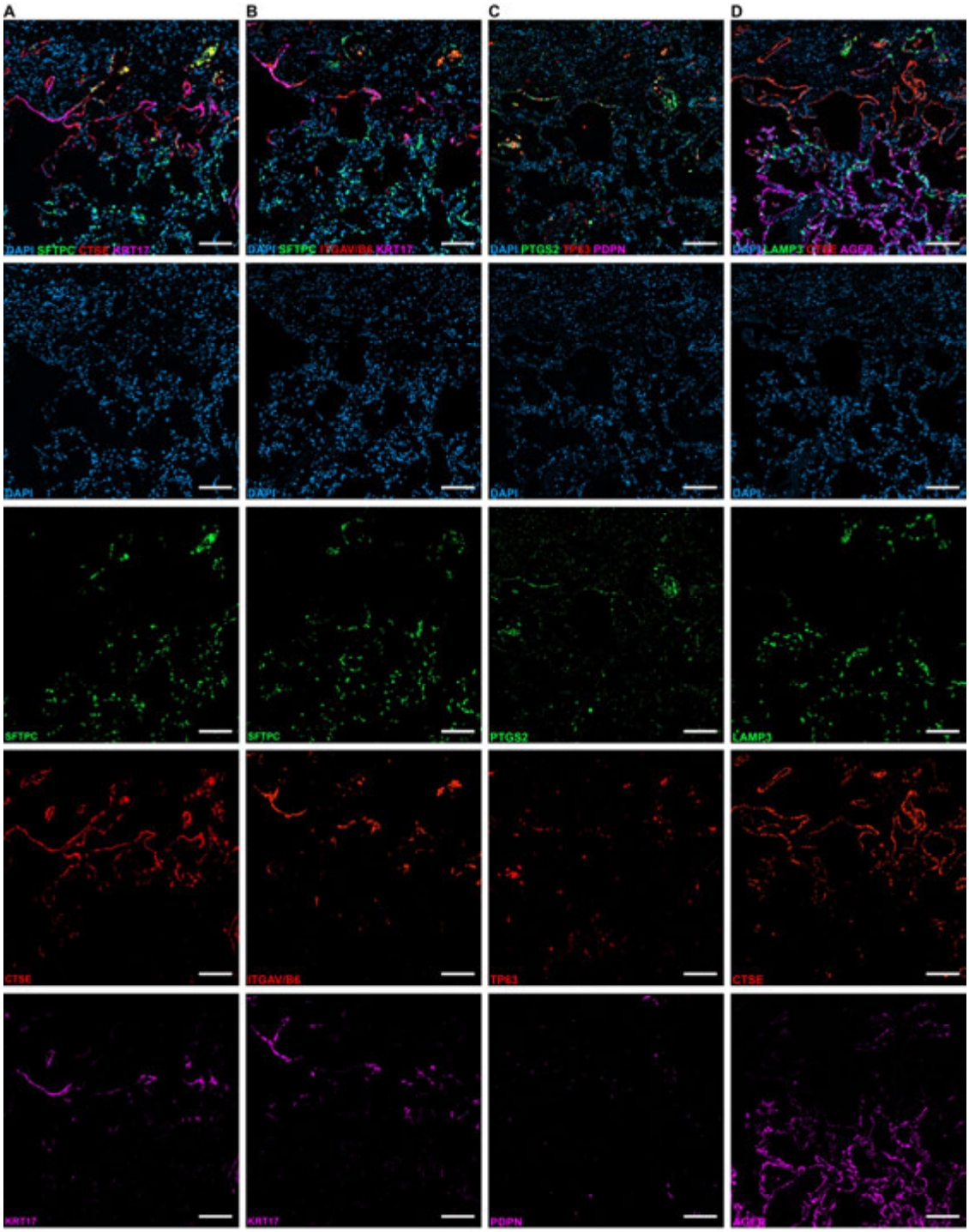

Figure E5: Split channels of epithelial targeted IF stains of RAS lungs. IF stains (split and merged channels) of peripheral RAS lung tissues. Scale bars are 100 µm. Target cell population: epithelial cells. For detailed information about the stains see figure legend of Fig. 3 A-C in the main manuscript.

Figure E6:

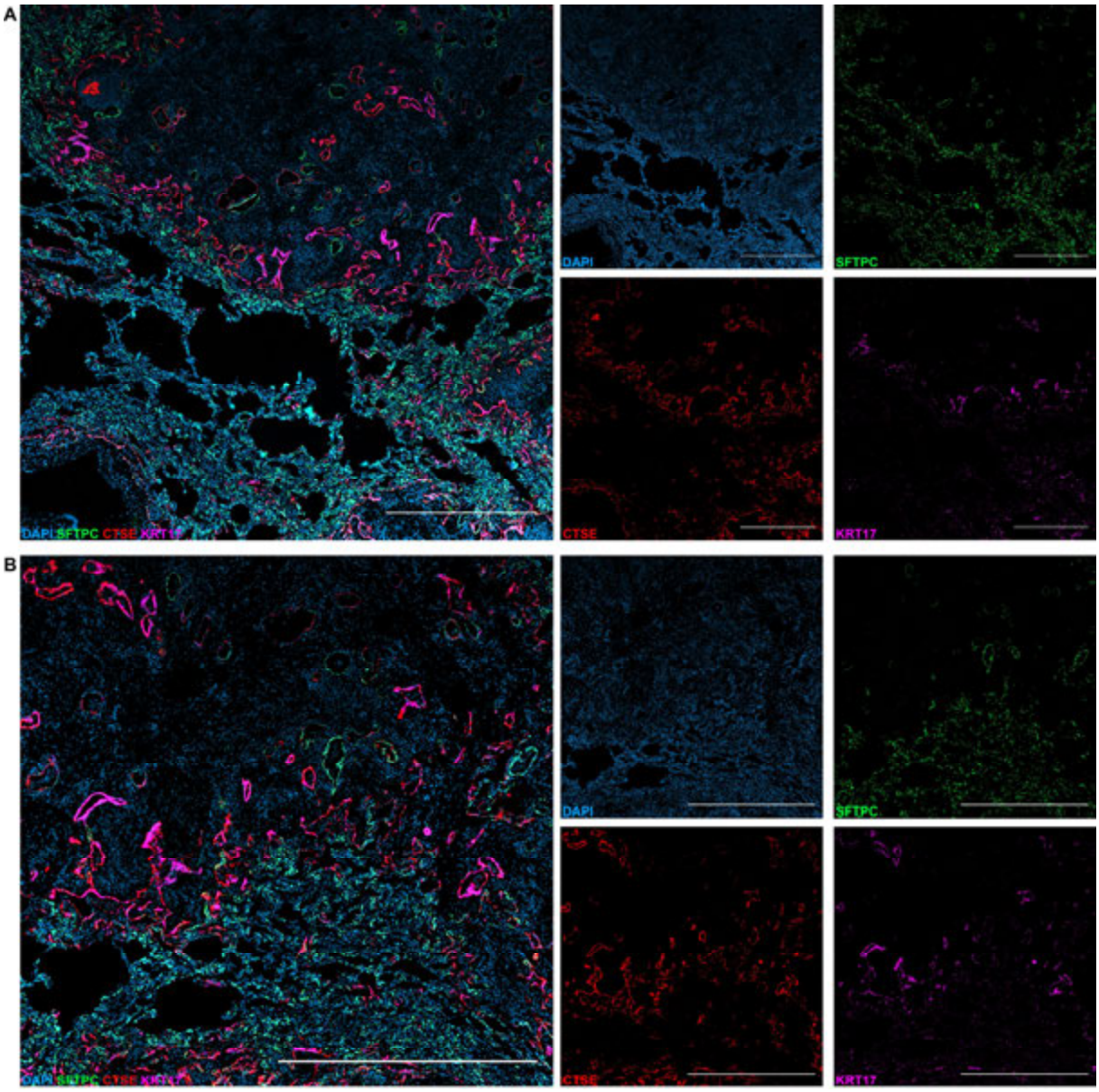

Figure E6: Split channels of epithelial targeted IF stains of RAS lungs. IF stains (split and merged channels) of peripheral RAS lung tissues. Scale bars in merged channels are 1000 µm and scale bars in split channels are 100 µm. Target cell population: epithelial cells. For detailed information about the stains see figure legend of Fig. 3 A-C in the main manuscript.

Figure E7:

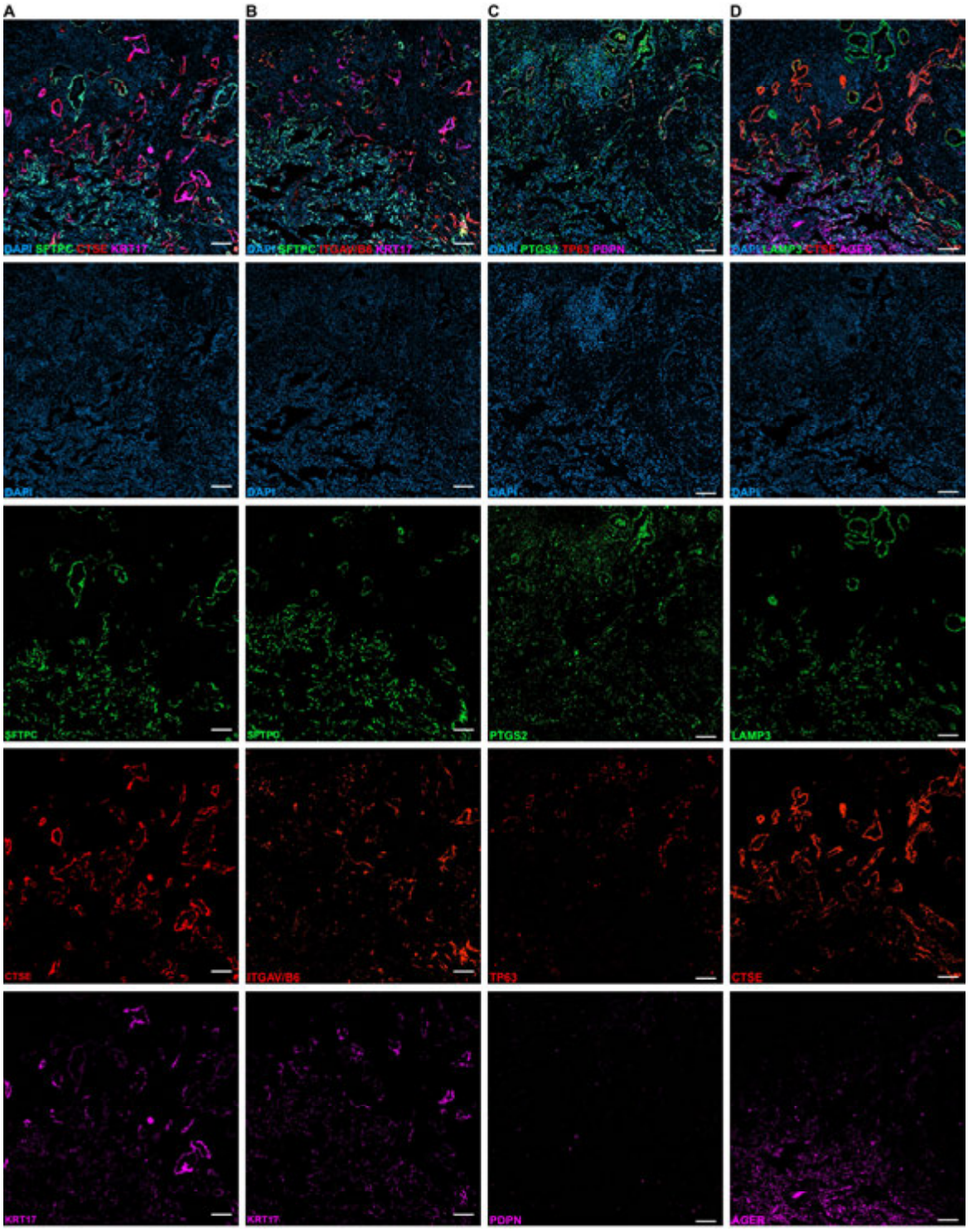

Figure E7: Split channels of epithelial targeted IF stains of RAS lungs. IF stains (split and merged channels) of peripheral RAS lung tissues. Scale bars are 100 µm. Target cell

population: epithelial cells. For detailed information about the stains see figure legend of Fig. 3 A-C in the main manuscript.

Figure E8:

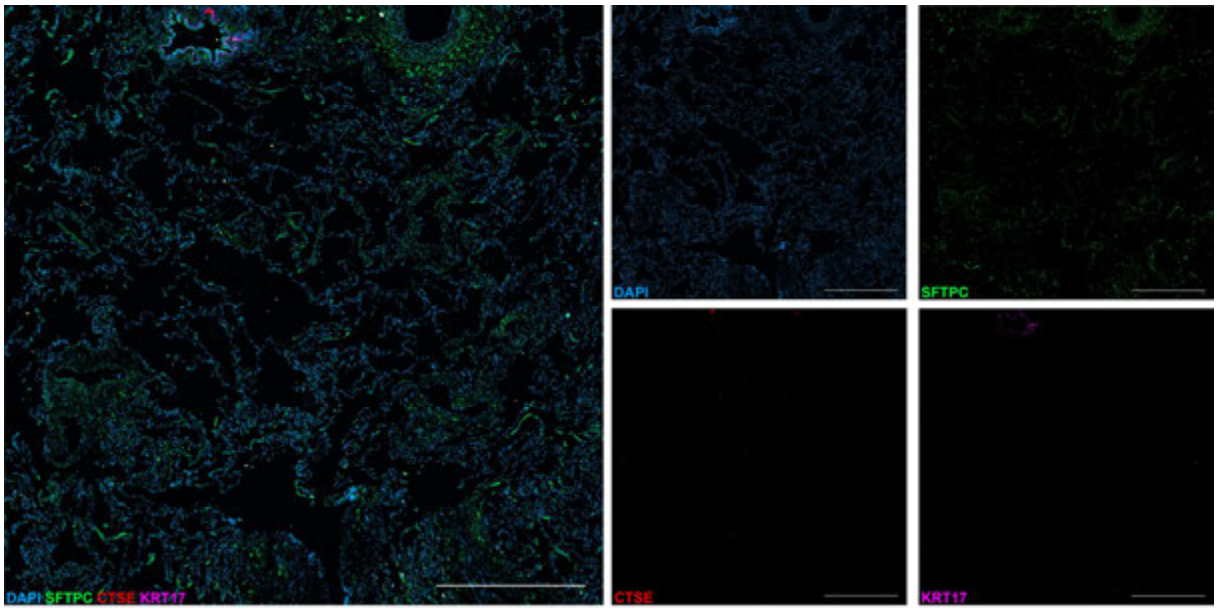

Figure E8: Split channels of epithelial targeted IF stains of control lungs. IF stains (split and merged channels) of peripheral control lung tissues. Scale bar in the merged channel is 1000 µm and scale bars in split channels are 100 µm. Target cell population: epithelial cells. No aberrant basaloid cells are observed in control stains. *KRT17*$^{+}$*/TP63*$^{+}$ cells are physiologic bronchial basal cells. Physiologic distribution patterns of *LAMP*$^{+}$*/AGER*$^{+}$ AT1 and *SFTPC*$^{+}$ AT2 cells are observed. No AFE or any other fibrotic areas are observed in control stains.

Figure E9:

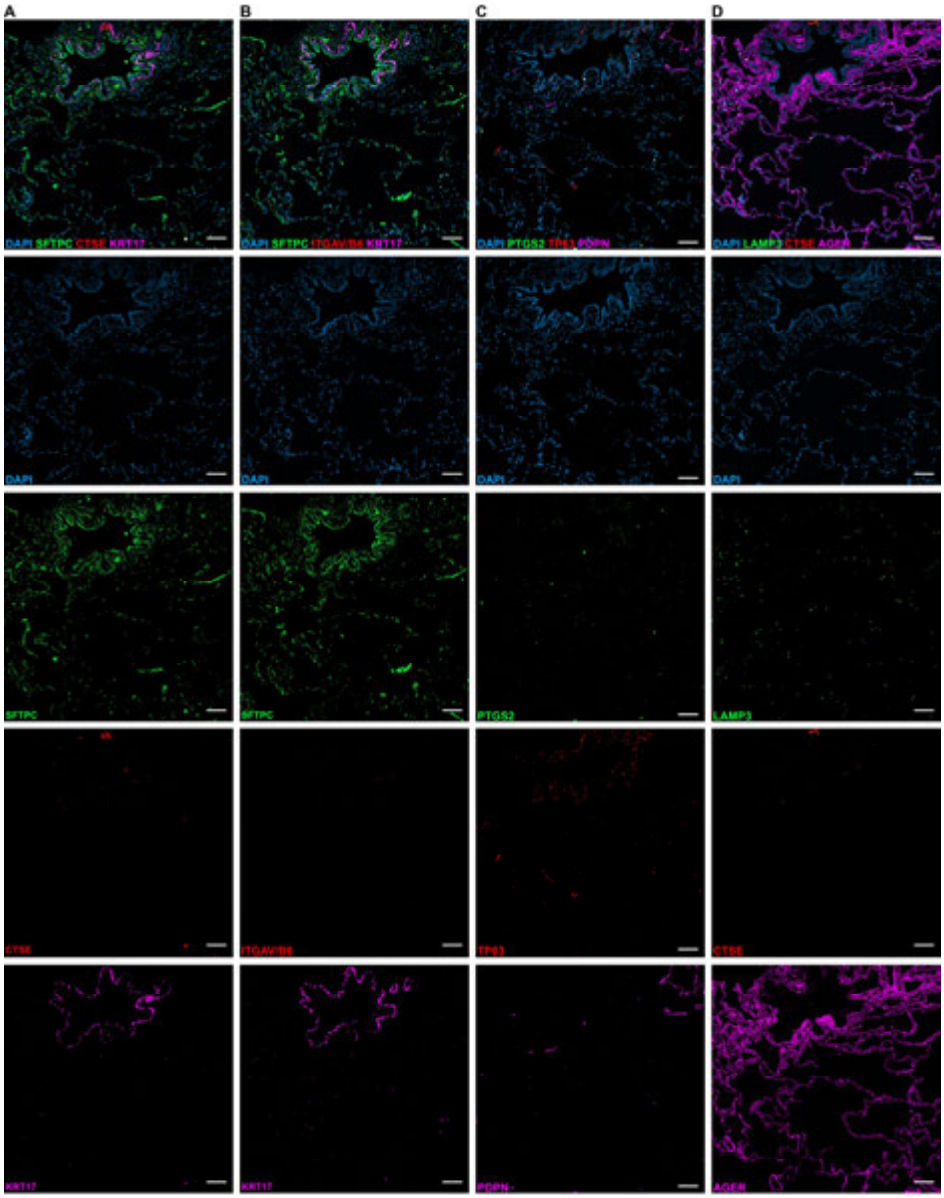

Figure E9: Split channels of epithelial targeted IF stains of control lungs. IF stains (split and merged channels) of peripheral control lung tissues. Scale bars in figures are 100 µm and stains depict closeup-views of Fig. E8. Target cell population: epithelial cells. No aberrant basaloid cells are observed in control stains. *KRT17*$^{+}$*/TP63*$^{+}$ cells are physiologic bronchial basal cells. Physiologic distribution patterns of *LAMP*$^{+}$*/AGER*$^{+}$ AT1 and *SFTPC*$^{+}$ AT2 cells are observed. No AFE or any other fibrotic areas are observed in control stains.

Figure E10:

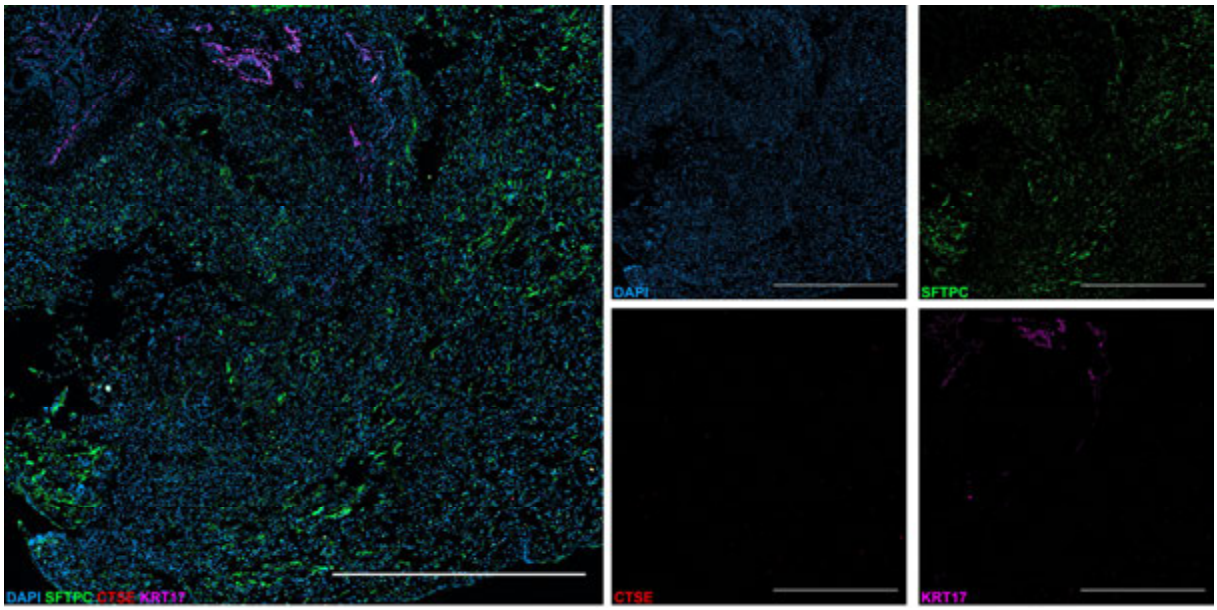

Figure E10: Split channels of epithelial targeted IF stains of control lungs. IF stains (split and merged channels) of peripheral control lung tissues. Scale bar in the merged channel is 1000 µm and scale bars in split channels are 100 µm. Target cell population: epithelial cells. No aberrant basaloid cells are observed in control stains. *KRT17*$^{+}$*/TP63*$^{+}$ cells are physiologic bronchial basal cells. Physiologic distribution patterns of *LAMP*$^{+}$*/AGER*$^{+}$ AT1 and *SFTPC*$^{+}$ AT2 cells are observed. No AFE or any other fibrotic areas are observed in control stains.

Figure E11:

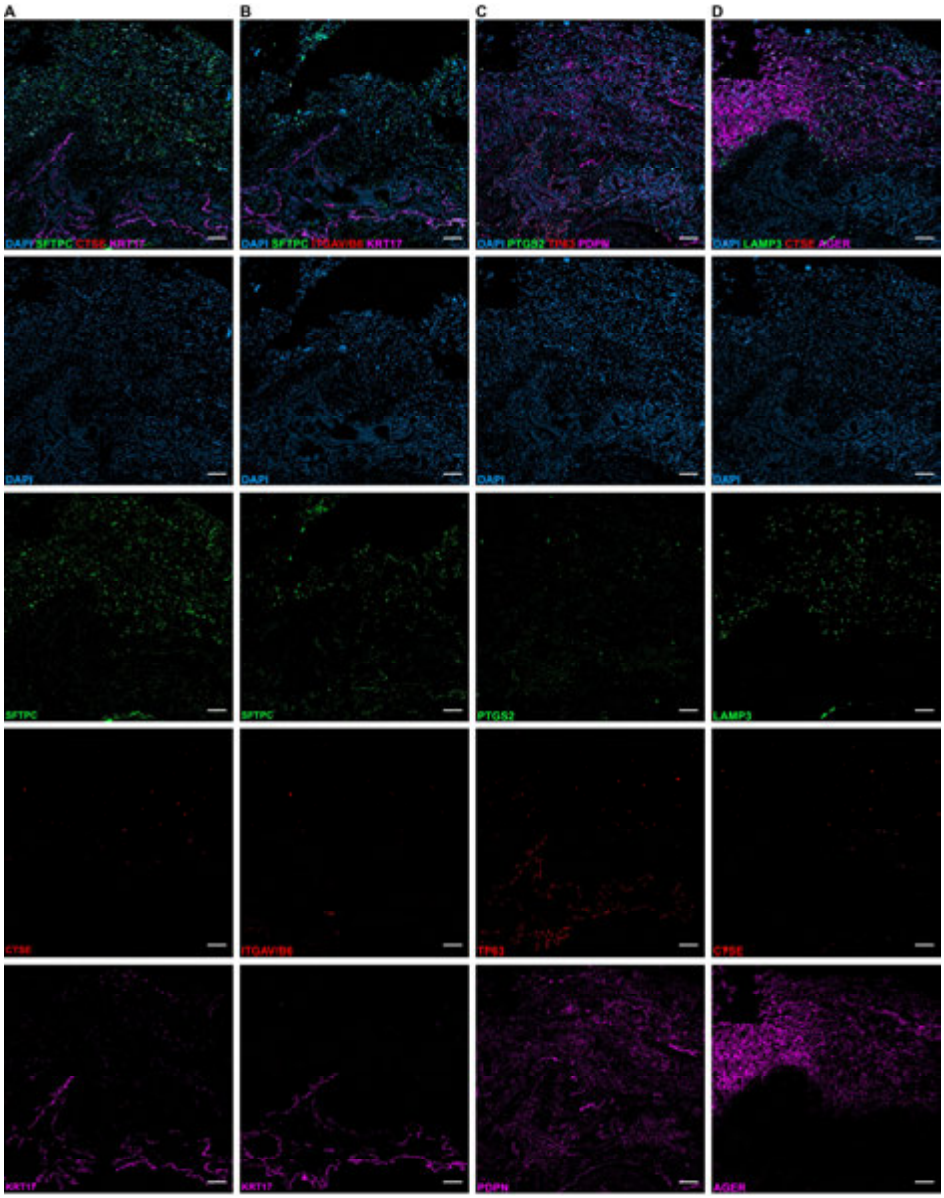

Figure E11: Split channels of epithelial targeted IF stains of control lungs. IF stains (split and merged channels) of peripheral control lung tissues. Scale bars in figures are 100 µm and stains depict closeup-views of Fig. E10. Target cell population: epithelial cells. No aberrant basaloid cells are observed in control stains. *KRT17*$^{+}$*/TP63*$^{+}$ cells are physiologic bronchial basal cells. Physiologic distribution patterns of *LAMP*$^{+}$*/AGER*$^{+}$ AT1 and *SFTPC*$^{+}$ AT2 cells are observed. No AFE or any other fibrotic areas are observed in control stains.

Figure E12:

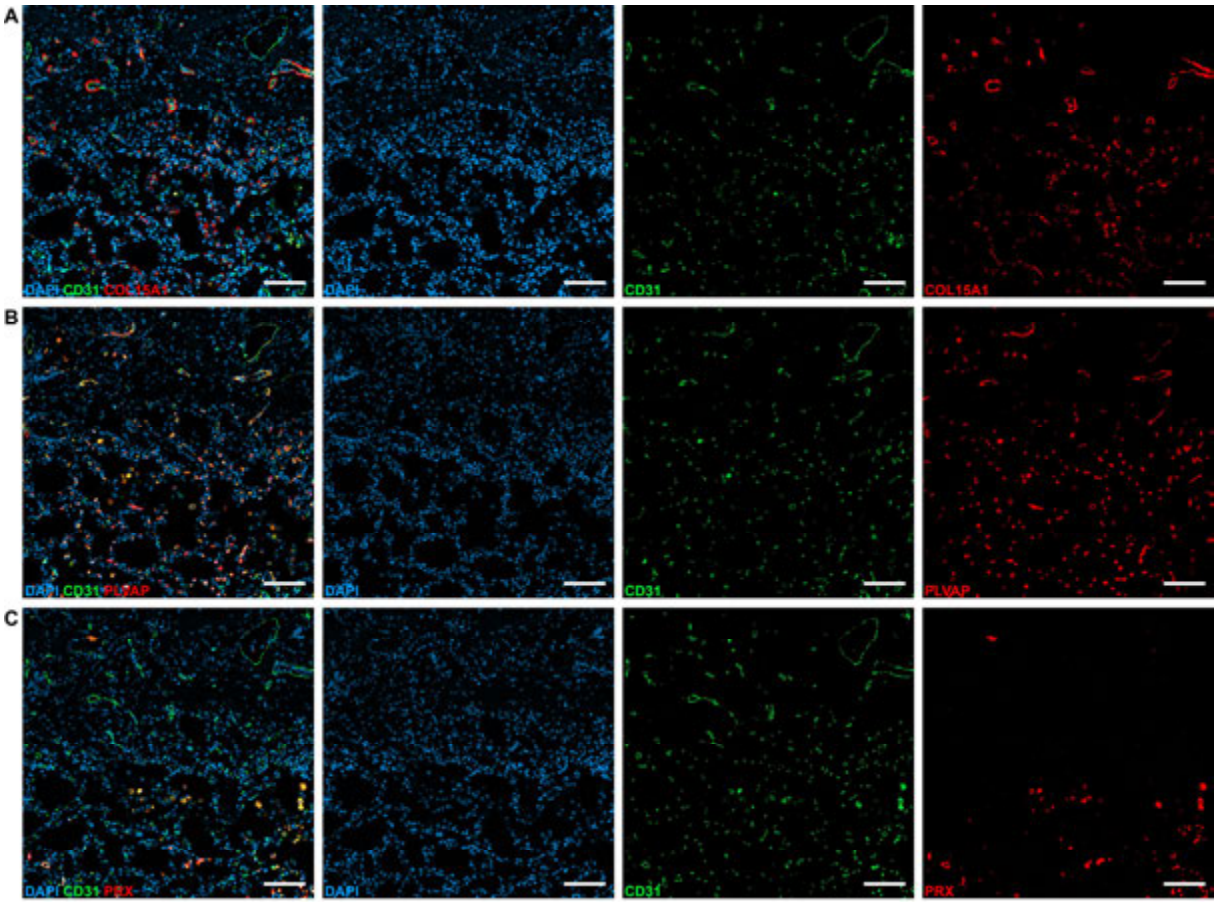

Figure E12: Split channels of endothelial targeted IF stains of RAS lungs. IF stains (split and merged channels) of peripheral RAS lung tissues. Scale bars are 100 µm. Target cell population: endothelial cells. For detailed information about the stains see figure legend of Fig. 5 A-C in the main manuscript.

Figure E13:

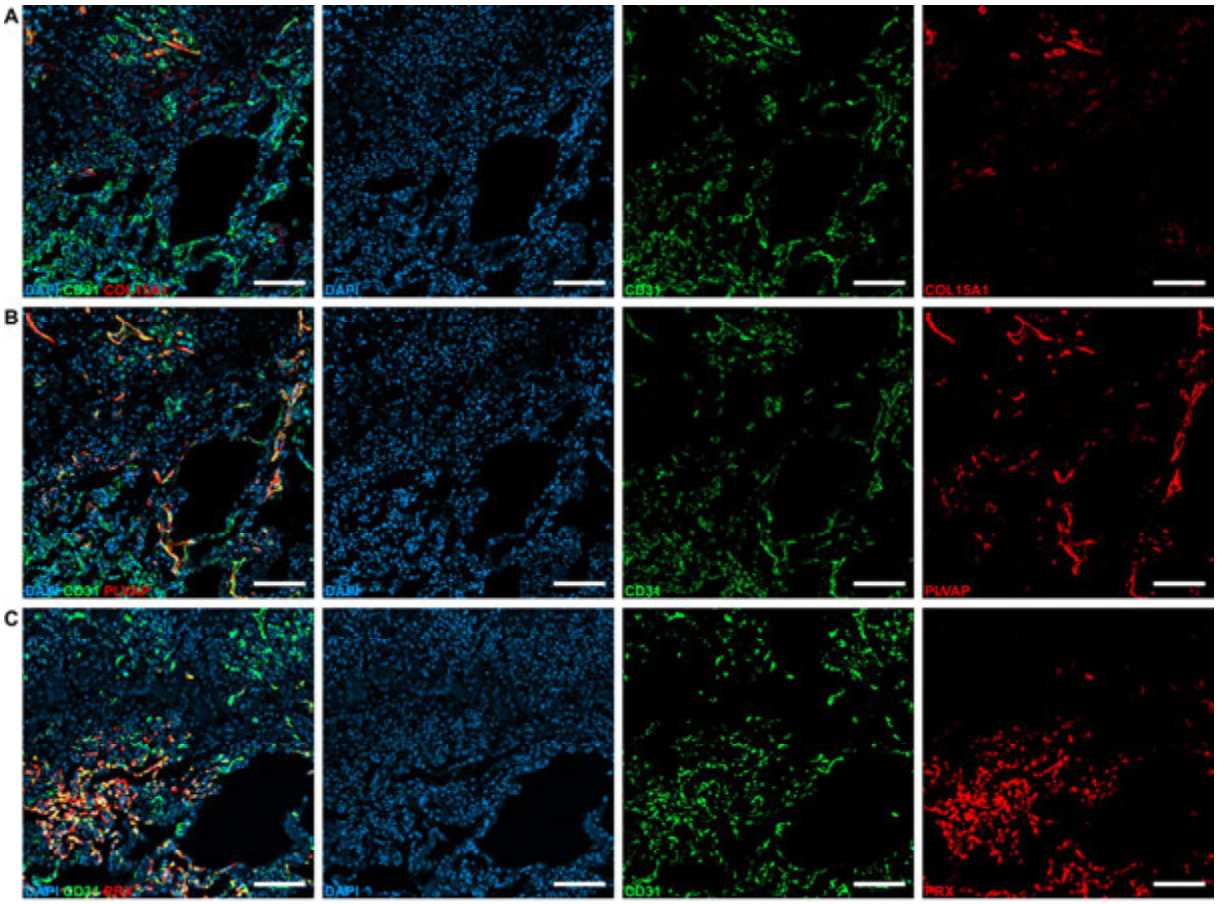

Figure E13: Split channels of endothelial targeted IF stains of RAS lungs. IF stains (split and merged channels) of peripheral RAS lung tissues. Scale bars are 100 µm. Target cell population: endothelial cells. For detailed information about the stains see figure legend of Fig. 5 A-C in the main manuscript.

Figure E14:

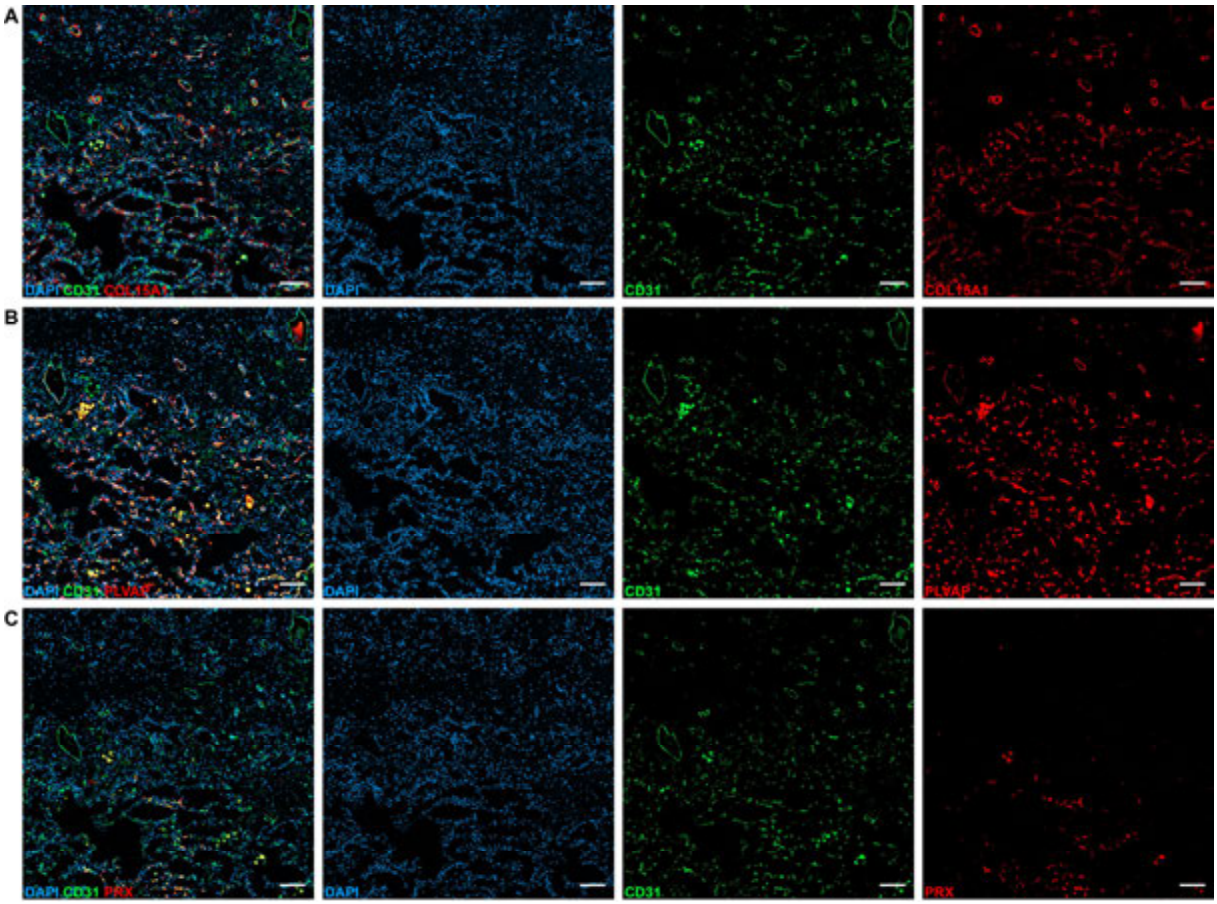

Figure E14: Split channels of endothelial targeted IF stains of RAS lungs. IF stains (split and merged channels) of peripheral RAS lung tissues. Scale bars are 100 µm. Target cell population: endothelial cells. For detailed information about the stains see figure legend of Fig. 5 A-C in the main manuscript.

Figure E15:

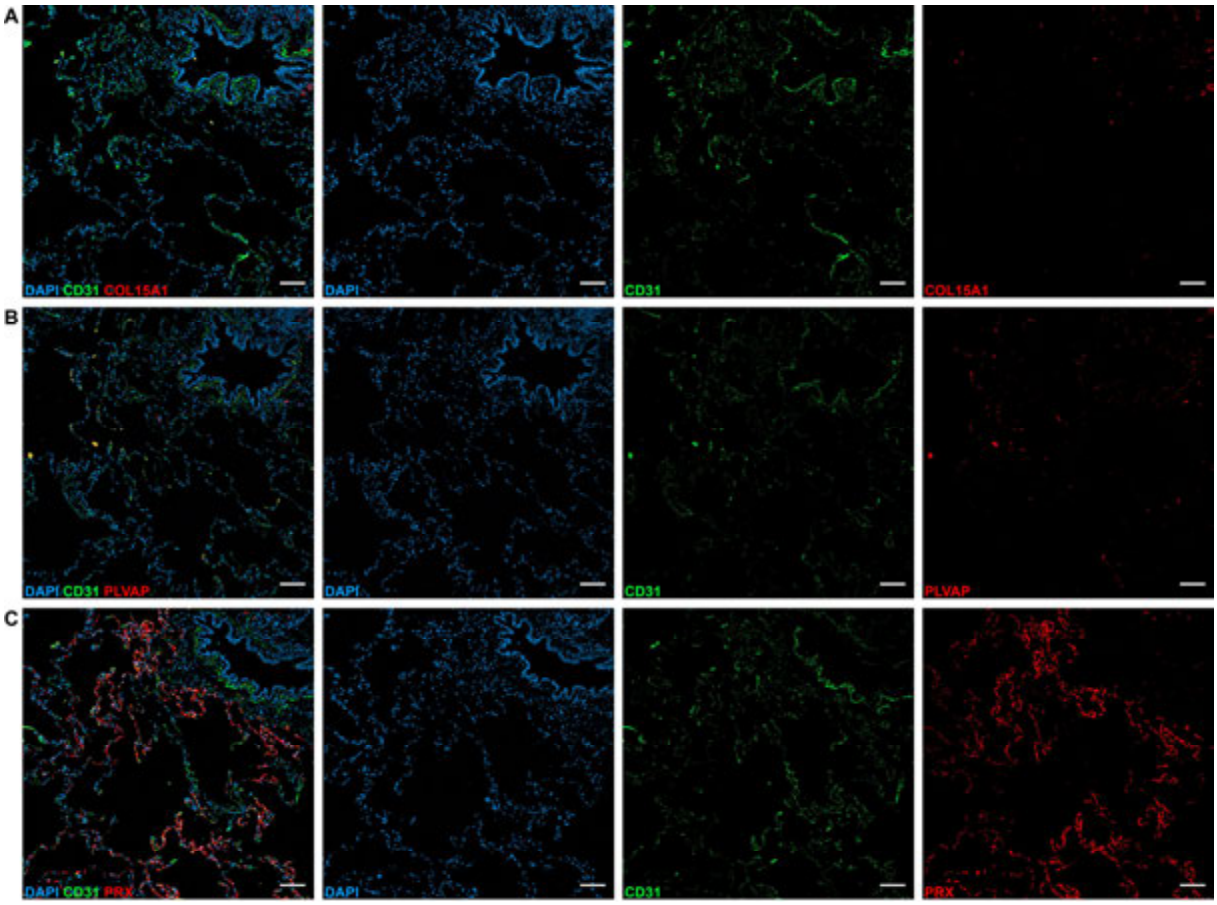

Figure E15: Split channels of endothelial targeted IF stains of control lungs. IF stains (split and merged channels) of peripheral control lung tissues. Scale bars are 100 µm. Target cell population: endothelial cells. *CD31⁺/COL15A1⁺/PLVAP⁺* peribronchial vascular endothelial cells (pVECs) are only observed adjacent to bronchi(oli) and near the pleura. No ectopic pVECs are observed in control specimens. A physiologic distribution pattern of *CD31⁺/PRX⁺* vascular endothelial cells representing physiologic alveolar microvasculature is observed.

Figure E16:

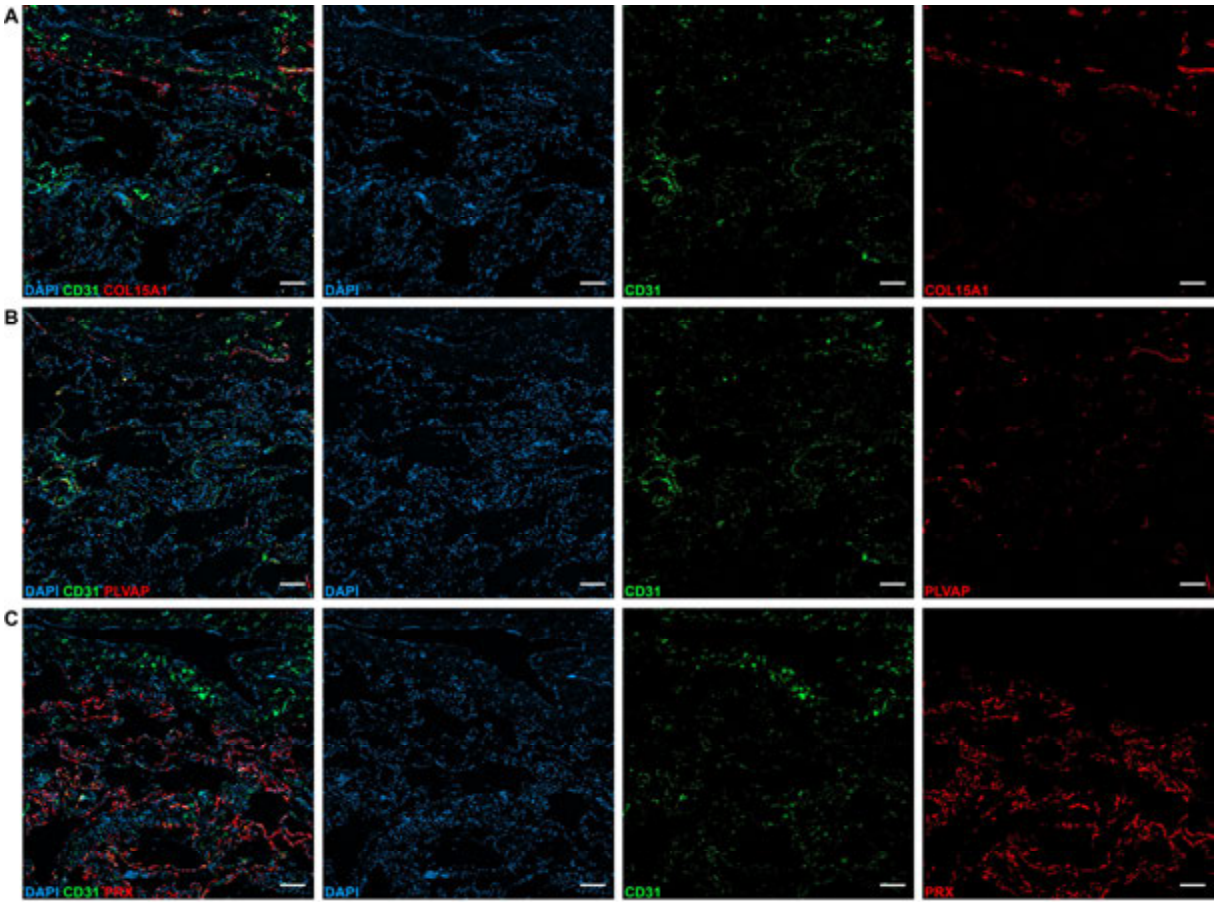

Figure E16: Split channels of endothelial targeted IF stains of control lungs. IF stains (split and merged channels) of peripheral control lung tissues. Scale bars are 100 µm. Target cell population: endothelial cells. *CD31⁺/COL15A1⁺/PLVAP⁺* peribronchial vascular endothelial cells (pVECs) are only observed adjacent to bronchi(oli) and near the pleura. No ectopic pVECs are observed in control specimens. A physiologic distribution pattern of *CD31⁺/PRX⁺* vascular endothelial cells representing physiologic alveolar microvasculature is observed.

Figure E17:

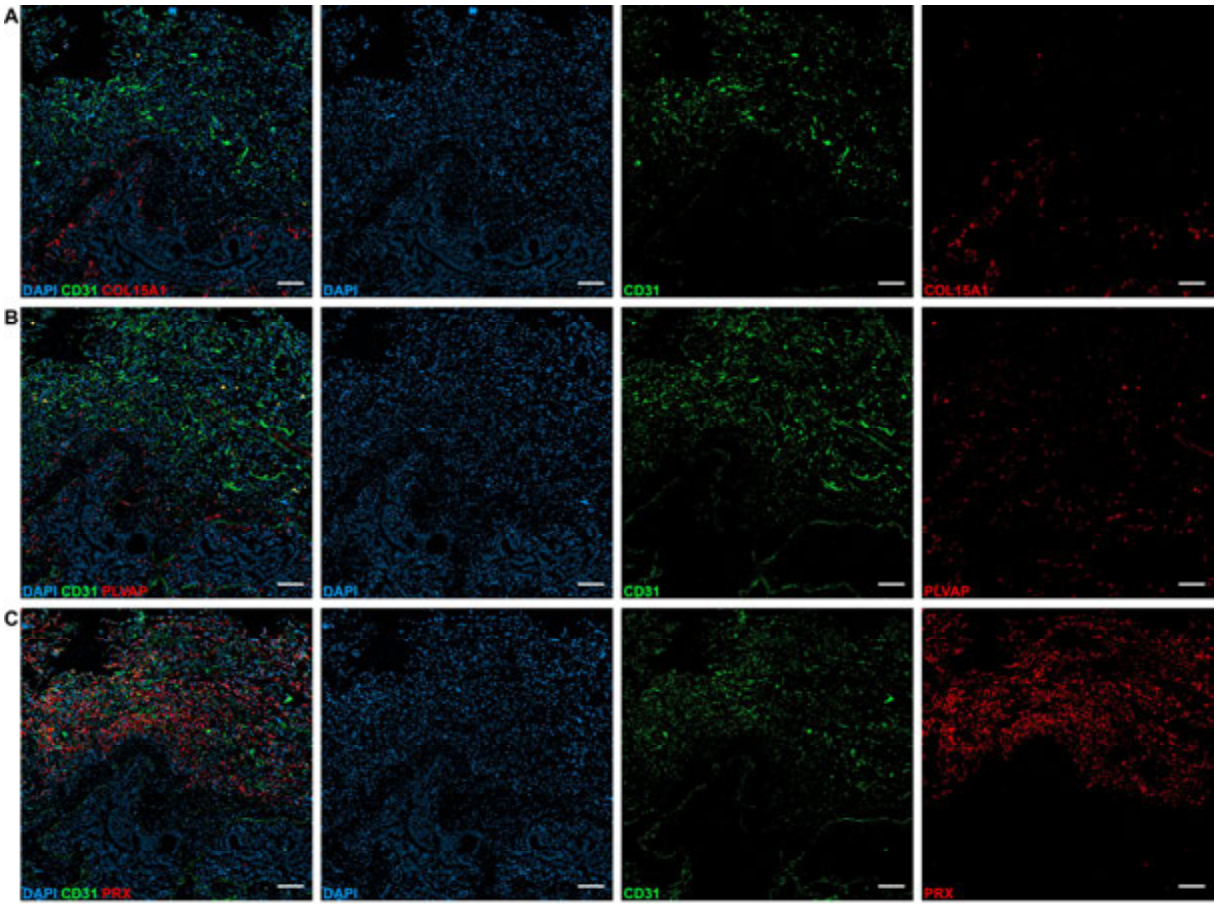

Figure E17: Split channels of endothelial targeted IF stains of control lungs. IF stains (split and merged channels) of peripheral control lung tissues. Scale bars are 100 µm. Target cell population: endothelial cells. *CD31⁺/COL15A1⁺/PLVAP⁺* peribronchial vascular endothelial cells (pVECs) are only observed adjacent to bronchi(oli) and near the pleura. No ectopic pVECs are observed in control specimens. A physiologic distribution pattern of *CD31⁺/PRX⁺* vascular endothelial cells representing physiologic alveolar microvasculature is observed.

Figure E18:

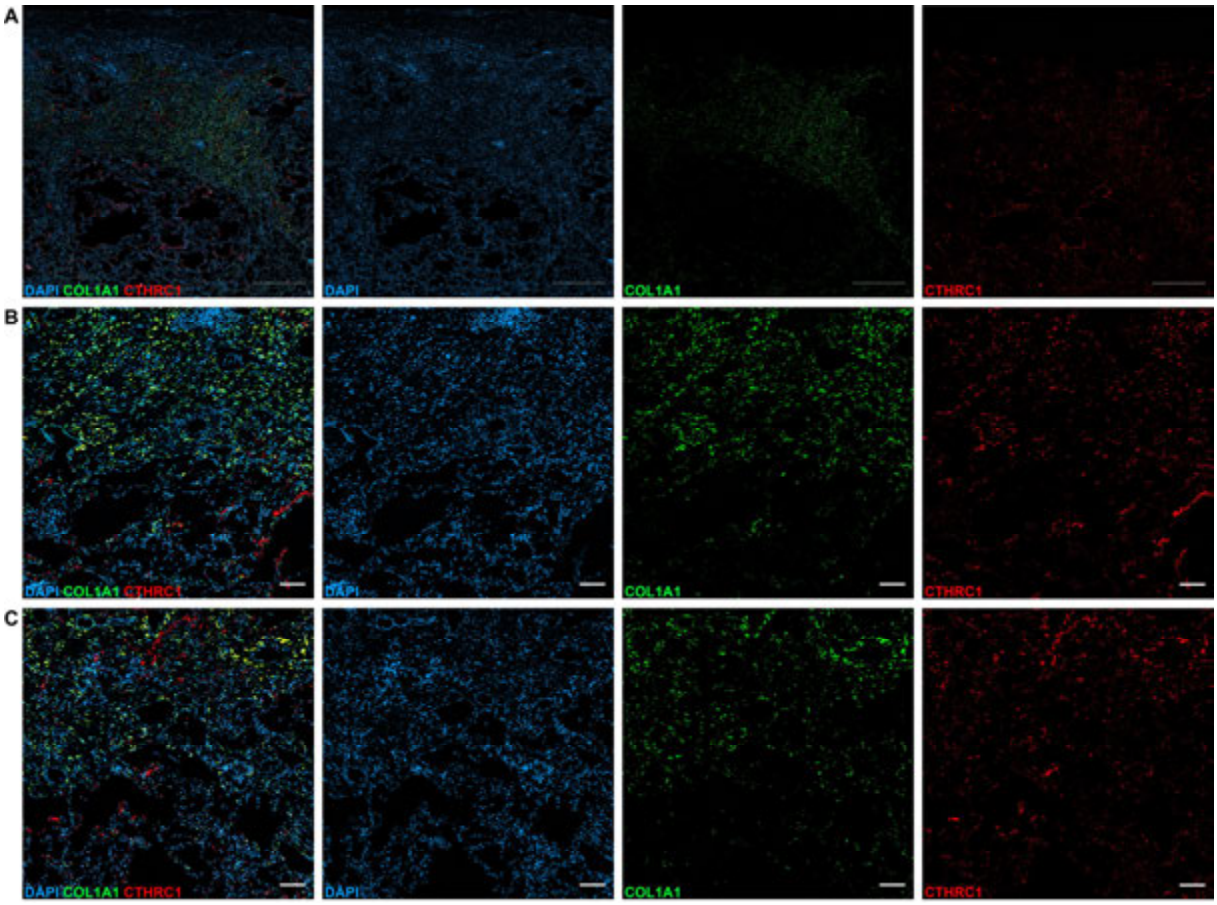

Figure E18: Split channels of stromal targeted RNA *in situ* hybridization stains of RAS lungs.

RNA *in situ* hybridization (RNAscope™) stains of peripheral RAS lung tissues. Scale bars in **A** are 1000 µm. Scale bars in **B** and **C** are 100 µm. Target cell population: stromal cells. For detailed information about the stains see figure legend of Fig. 6 G-I in the main manuscript.

Figure E19:

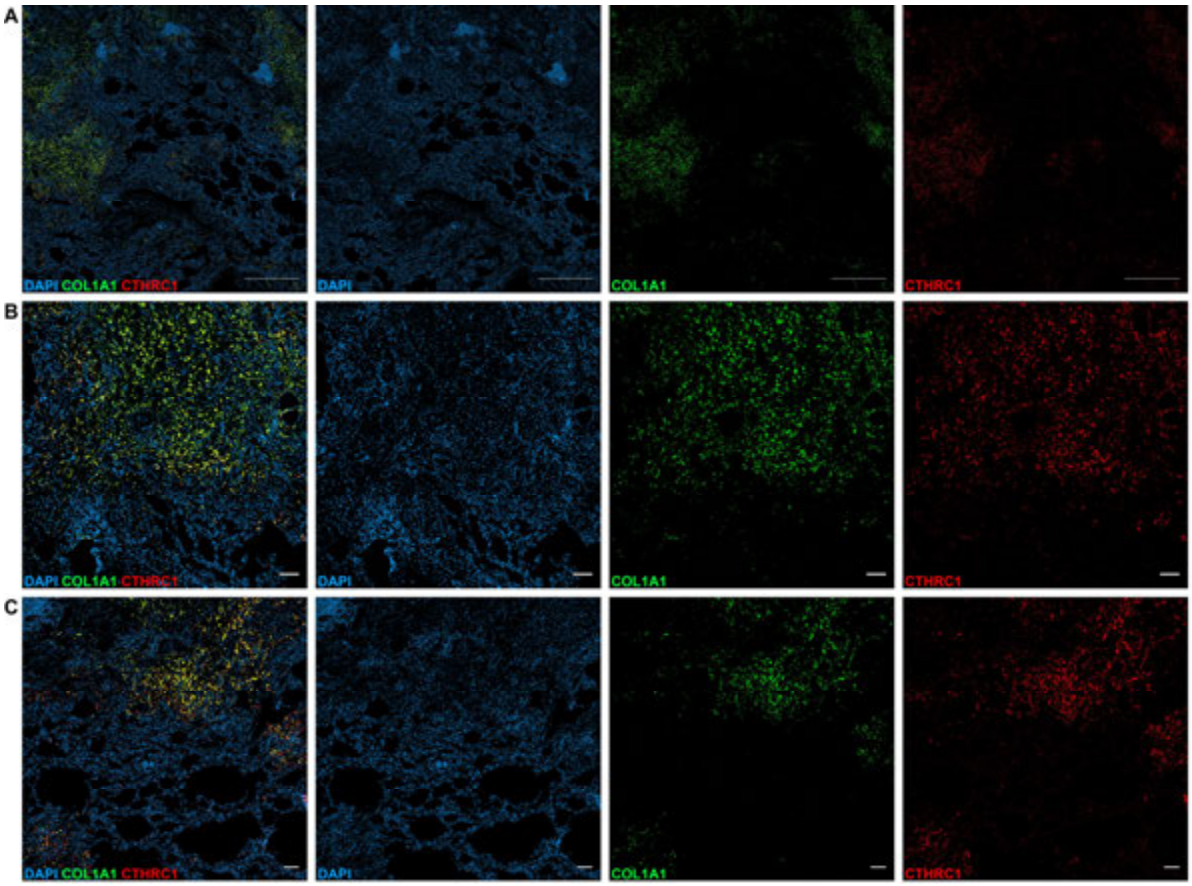

Figure E19: Split channels of stromal targeted RNA *in situ* hybridization stains of RAS lungs.

RNA *in situ* hybridization (RNAscope™) stains of peripheral RAS lung tissues. Scale bars in **A** are 1000 µm. Scale bars in **B** and **C** are 100 µm. Target cell population: stromal cells. For detailed information about the stains see figure legend of Fig. 6 G-I in the main manuscript.

Figure E20:

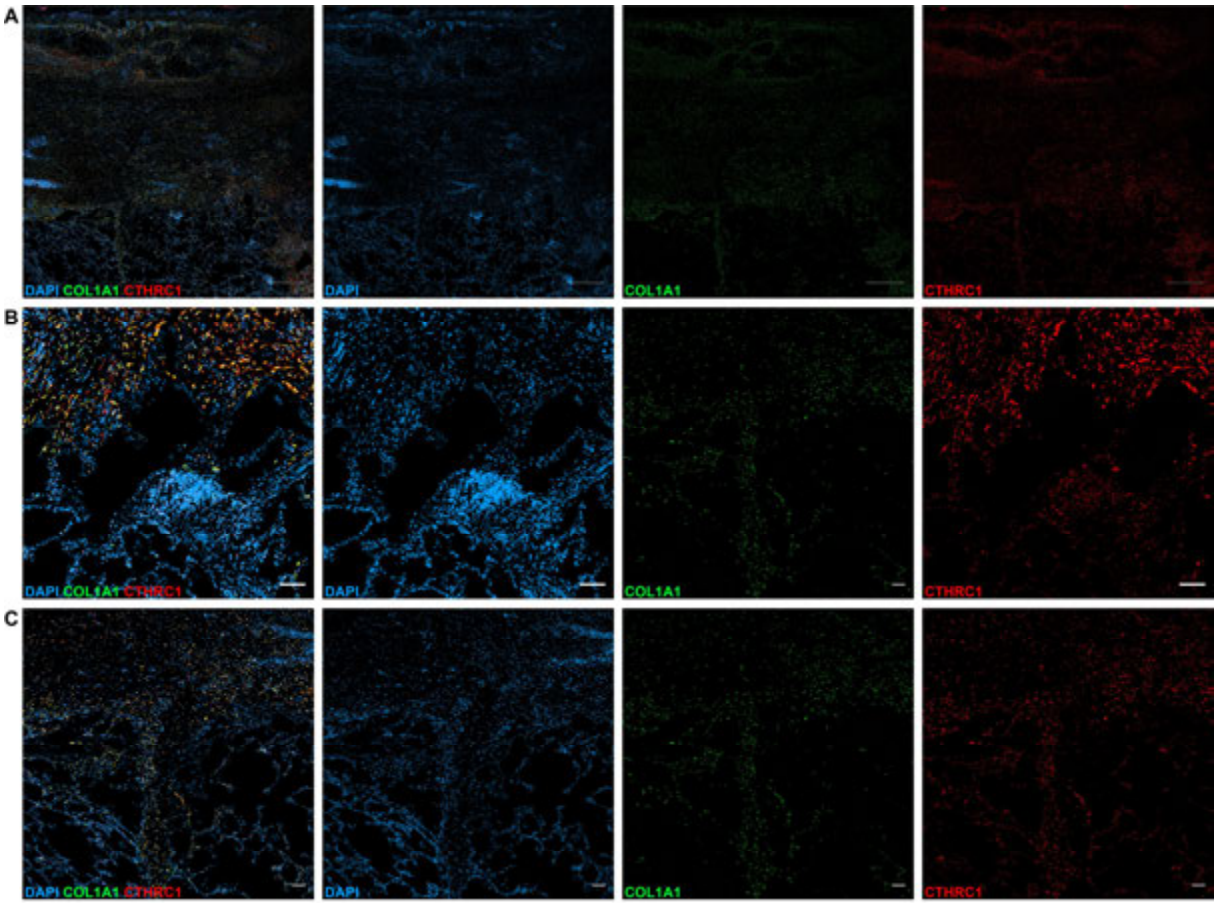

Figure E20: Split channels of stromal targeted RNA *in situ* hybridization stains of RAS lungs.

RNA *in situ* hybridization (RNAscope™) stains of peripheral RAS lung tissues. Scale bars in **A** are 1000 µm. Scale bars in **B** and **C** are 100 µm. Target cell population: stromal cells. For detailed information about the stains see figure legend of Fig. 6 G-I in the main manuscript.

Figure E21:

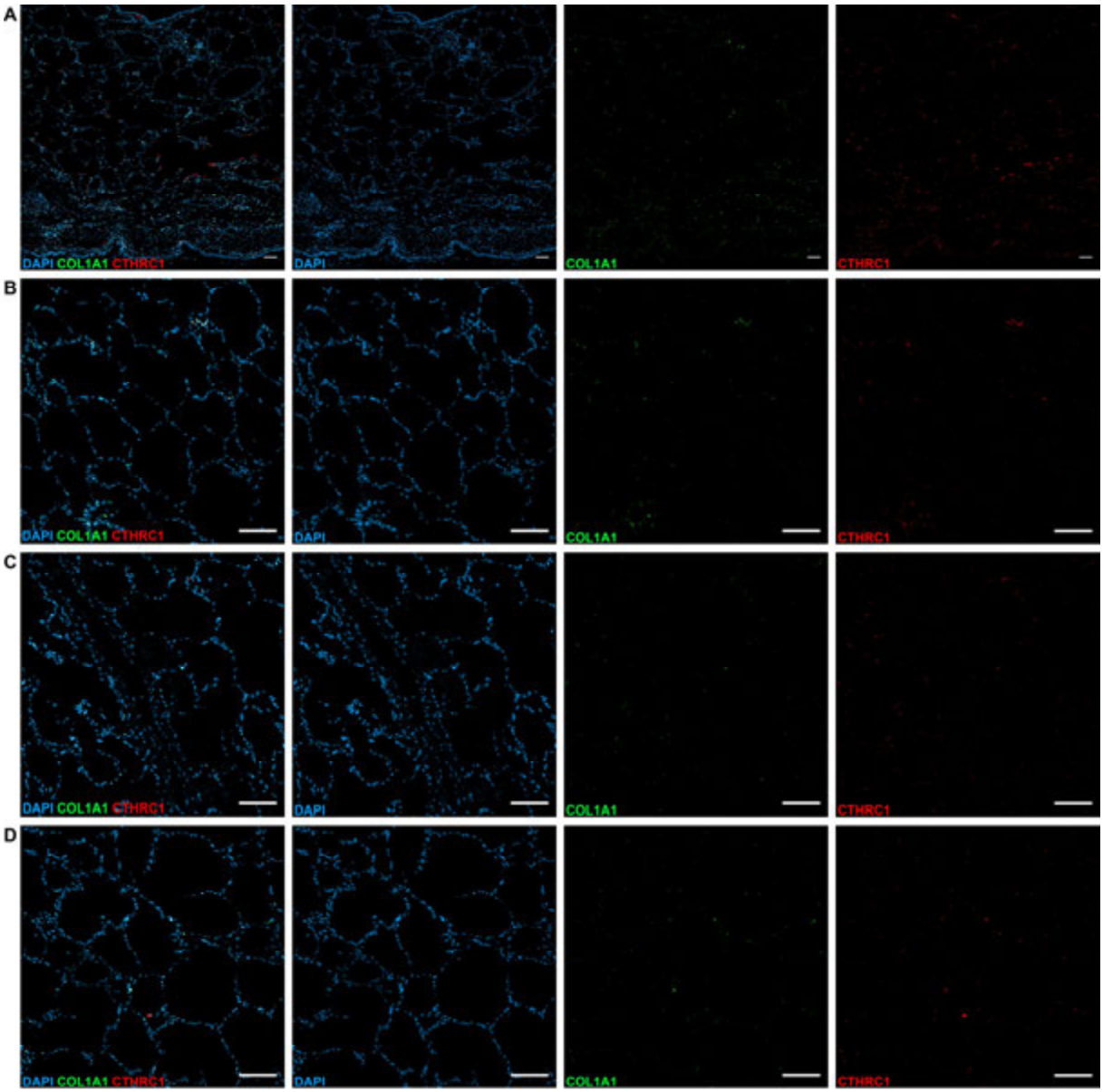

Figure E21: Split channels of stromal targeted RNA *in situ* hybridization stains of control lungs. RNA *in situ* hybridization (RNAscope™) stains of 4 peripheral control lung tissues. Scale bars are 100 µm. Target cell population: stromal cells. None to very few *COL1A1*$^{+}$/*CTHRC1*$^{+}$ fibrotic fibroblasts are observed in control stains.

Figure E22:

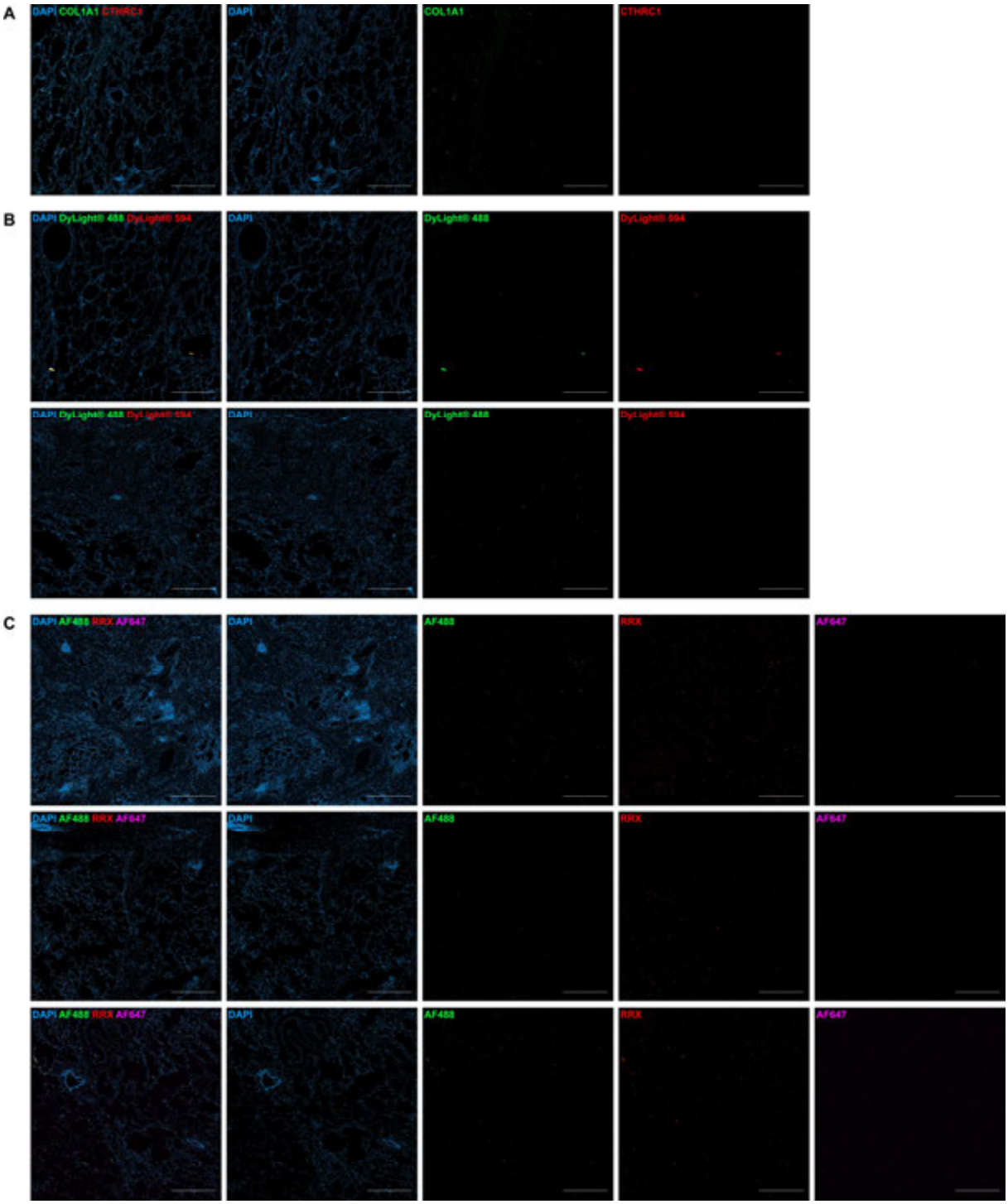

Figure E22: Split channels of RNA *in situ* hybridization and IF negative control stains. RNA *in situ* hybridization and IF stains (split and merged channels) of negative controls. Scale bars are 1000 µm.

A: RNA *in situ* hybridization negative control stain for RNAscope™ Probe - Hs-COL1A1 (Advanced Cell Diagnostics, part of Bio-Techne, Newark, CA, USA; Cat# 401891) and RNAscope™ Probe - Hs-CTHRC1 (Advanced Cell Diagnostics, part of Bio-Techne, Newark, CA, USA; Cat# 413331). **B**: IF negative control stains for VectaFluor™ Duet Immunofluorescence Double Labeling Kit, DyLight® 594 Anti-Rabbit (red), DyLight® 488 Anti-Mouse (green) (Vector Laboratories, Newark, CA, USA; Cat# DK-8828). **C**: IF negative control stains for Donkey anti-Goat IgG (H+L), Alexa Fluor® 488 (AF 488), AffiniPure® (Jackson ImmunoResearch, West Grove, PA, USA; Cat# 705-545-147), Donkey anti-Rabbit IgG (H+L), Rhodamine Red™-X (RRX), AffiniPure® (Jackson ImmunoResearch, West Grove, PA, USA; Cat# 711-295-152), and Donkey anti-Mouse IgG (H+L), Highly Cross-Adsorbed Secondary Antibody, Alexa Fluor™ Plus 647 (AF 647) (Invitrogen™, Thermo Fisher Scientific, Waltham, MA, USA; Cat# A32787TR).

Figure E23:

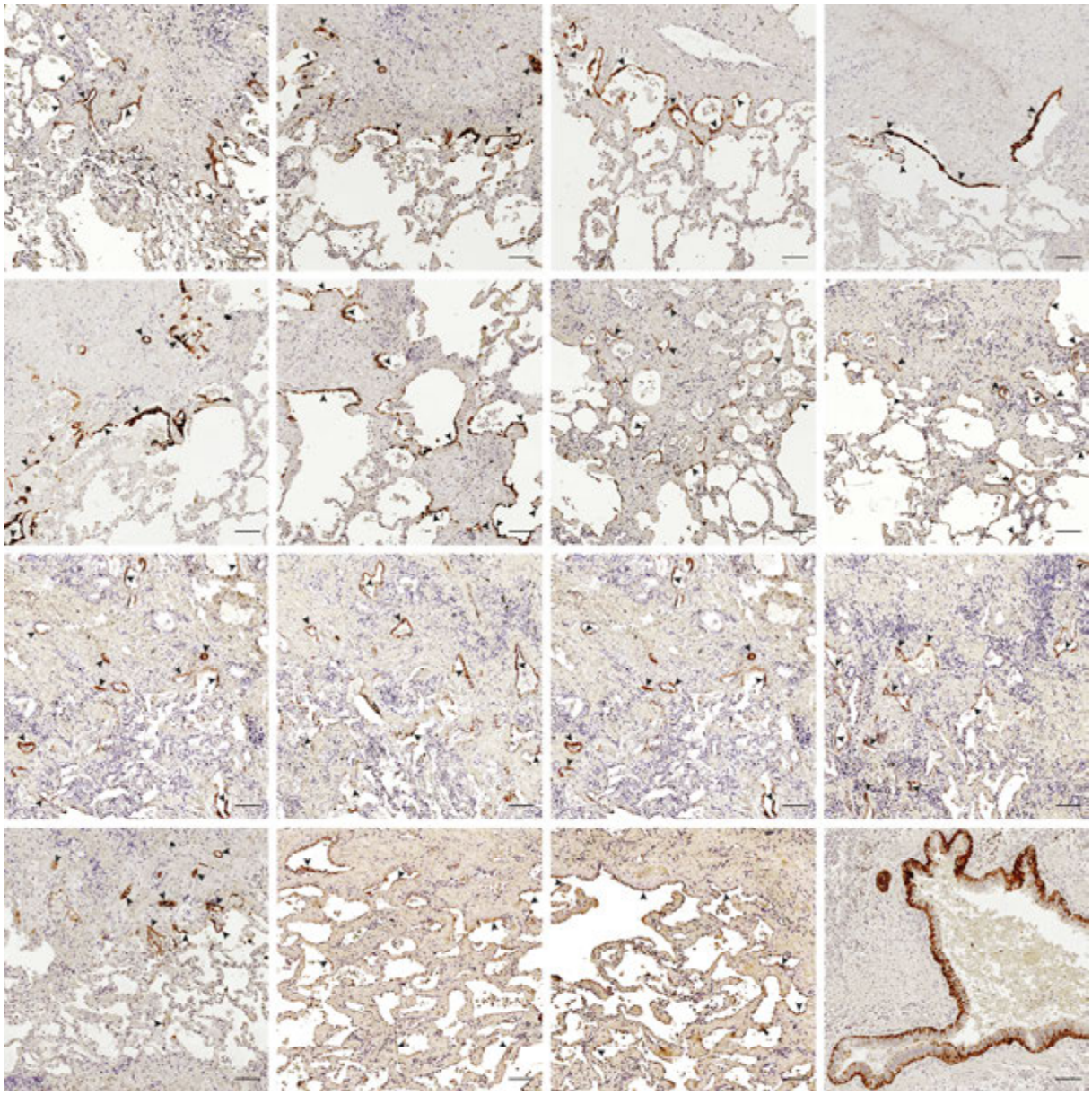

Figure E23: IHC stains of KRT17^{+} aberrant basaloid cells. IHC stains for *KRT17* in RAS. Scale bars are 100 µm. Arrows indicate exemplary *KRT17*$^{+}$ cells. *KRT17*$^{+}$ cells line the fibrotic edge, obliterating alveoli and fibrotically thickened alveolar septa. The last image shows a bronchiole with *KRT17*$^{+}$ basal cells as an internal control for specific *KRT17* staining.

Figure E24:

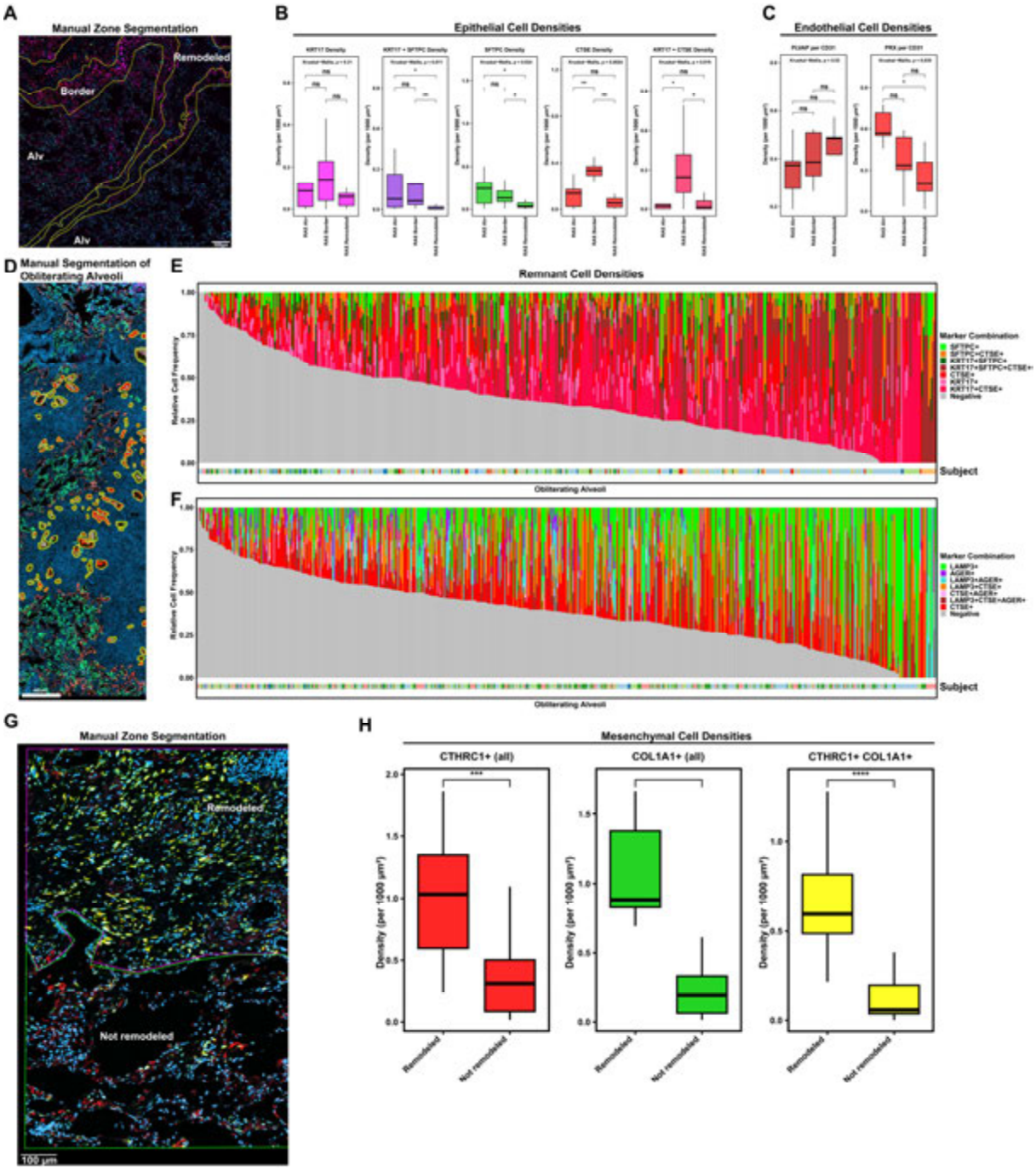

Figure E24: Quantification of cellular distribution and composition of "obliterating alveoli" in RAS. A: Representative example of manual zone segmentation for IF stains. Three zones were annotated: "Alv" = alveolar tissue, "Border" = fibrotic edge and adjacent fibrotic areas, and "Remodeled" = fibrotic areas. Scale bar is 500 µm. **B:** Quantification of epithelial cell densities in each zone (Alv, Border, Remodeled) based on multiplex IF staining and artificial

neural network analysis. *KRT17^{+}/CTSE^{+}* cells indicate aberrant basaloid cells, *KRT17^{+}/SFTPC^{+}* cells mark transitional cells. Statistical comparisons among zones were performed using the Wilcoxon rank sum test with *: $p \leq 0.05$, **: $p \leq 0.01$, ***: $p \leq 0.001$, and ****: $p \leq 0.0001$. **C:** Quantification of endothelial cell densities across the same zones. *PLVAP^{+}/CD31^{+}* cells indicate *COL15A1^{+}/PLVAP^{+}*(ectopic) pVECs, *PRX^{+}/CD31^{+}* cells reflect physiological alveolar capillaries. Statistical testing as in (B). **D:** Representative example of manual segmentation of "obliterating alveoli". Scale bar is 400 µm. **E, F:** Each column depicts the cellular composition of manually segmented "obliterating alveoli". *KRT17^{+}/CTSE^{+}* cells indicate aberrant basaloid cells; *KRT17^{+}/SFTPC^{+}* cells are transitional cells; *LAMP^{+}/AGER^{+}* cells represent AT1 cells. "Obliterating alveoli" were ordered by the relative abundance of *KRT17^{-}/CTSE^{-}/SFTPC^{-}* cell populations. **G:** Representative example of manual zone segmentation for RNA *in situ* hybridization stains. Two zones were annotated: "Remodeled" = fibrotic areas and "Not remodeled" = non-fibrotic areas. Scale bar is 100 µm. **H:** Quantification of stromal cell densities in both zones ("Remodeled" and "Not remodeled") based on multiplex RNA *in situ* hybridization staining and artificial neural network analysis. *CTHRC1^{+}/COL1A1^{+}* cells indicate *CTHRC1^{+}* fibrotic fibroblasts. Statistical comparisons among zones were performed using the Wilcoxon rank sum test with *: $p \leq 0.05$, **: $p \leq 0.01$, ***: $p \leq 0.001$, and ****: $p \leq 0.0001$.

Figure E25:

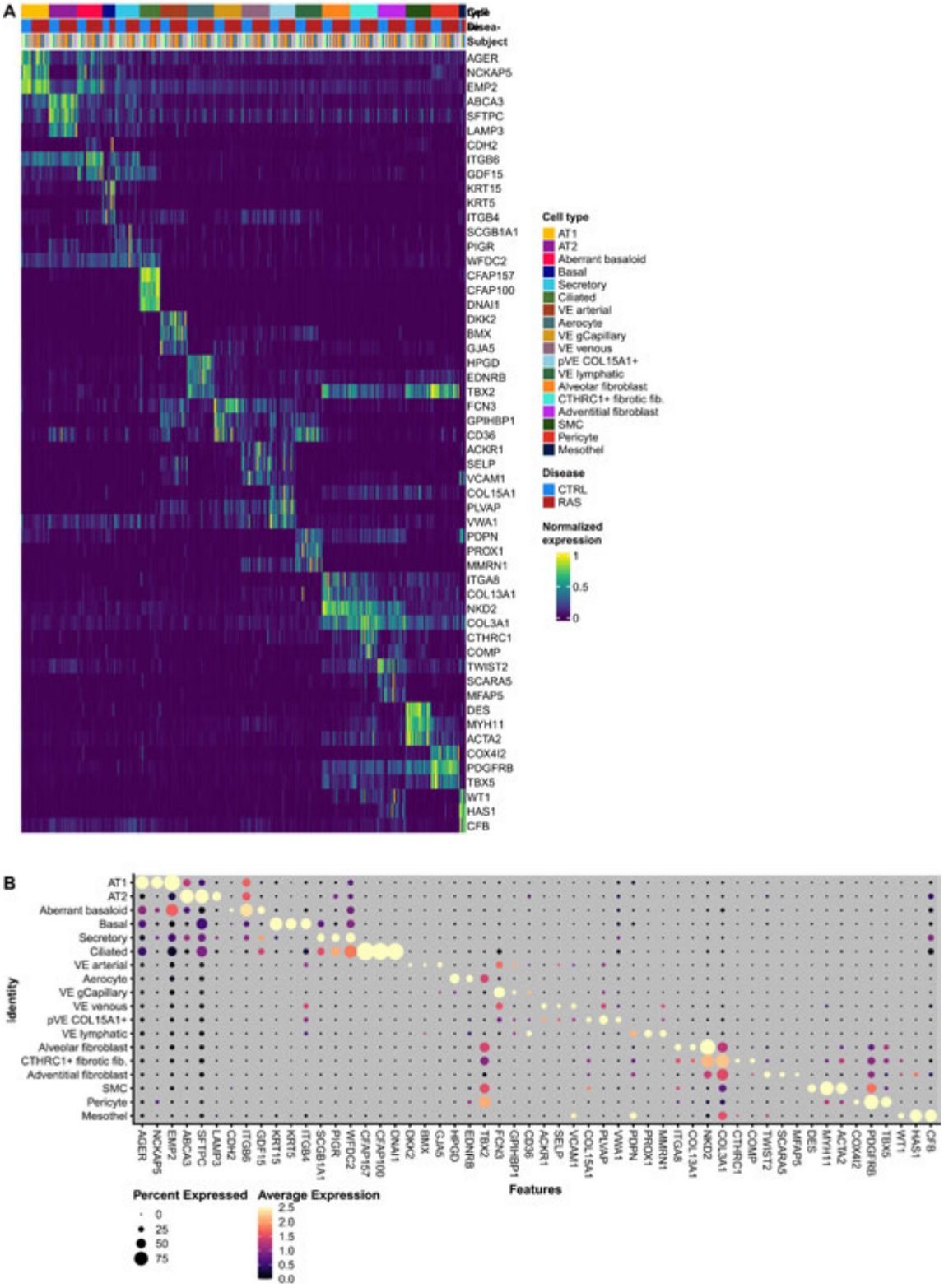

Figure E25: Heatmap and dot plot of lineage marker gene expression across analyzed cell types in RAS and CTRL subjects. A: Heatmap showing unity-normalized expression (range: 0–

1) of lineage marker genes across all analyzed cell types. Gene expression values are averaged per subject for each cell type. Each column represents the average marker gene expression of an individual subject, grouped by disease status (CTRL or RAS) and annotated cell type. Subjects are indicated by unique colors in the subject annotation bar; disease status is shown in the adjacent color bar. Cell types are represented in the colored bar at the top of the heatmap. **B:** Dot plot showing the same lineage marker genes across all analyzed cell types as in **(A)**. Gene expression values are averaged normalized per cell type.

Figure E26:

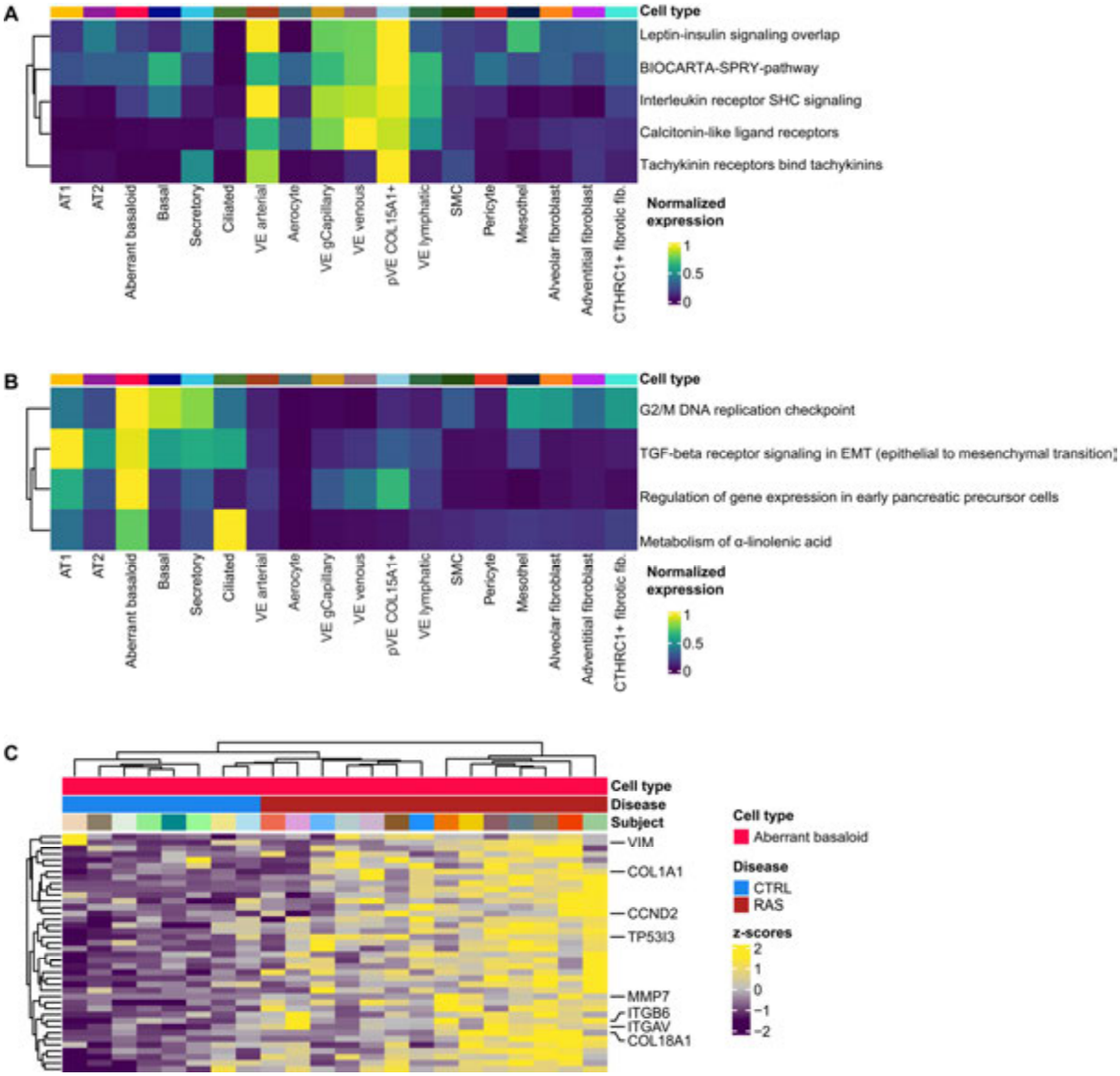

Figure E26: Pathway enrichment analysis in RAS and hierarchical clustering heatmaps of aberrant basaloid cells. A, B: Pathway analysis of 15 specimens. Depicted are average enrichment scores per cell type and disease state. Enrichment scores are unity normalized between 0 and 1 across all identified cell types. Cell types are indicated by the colored annotation bars above. **C:** Heat map of differentially expressed genes comparing RAS and controls in aberrant basaloid cells, hierarchically clustered. Average expression values are

scaled across subjects. Each subject is represented by a unique color, and disease state and cell type are represented in the colored annotation bars above.

Figure E27:

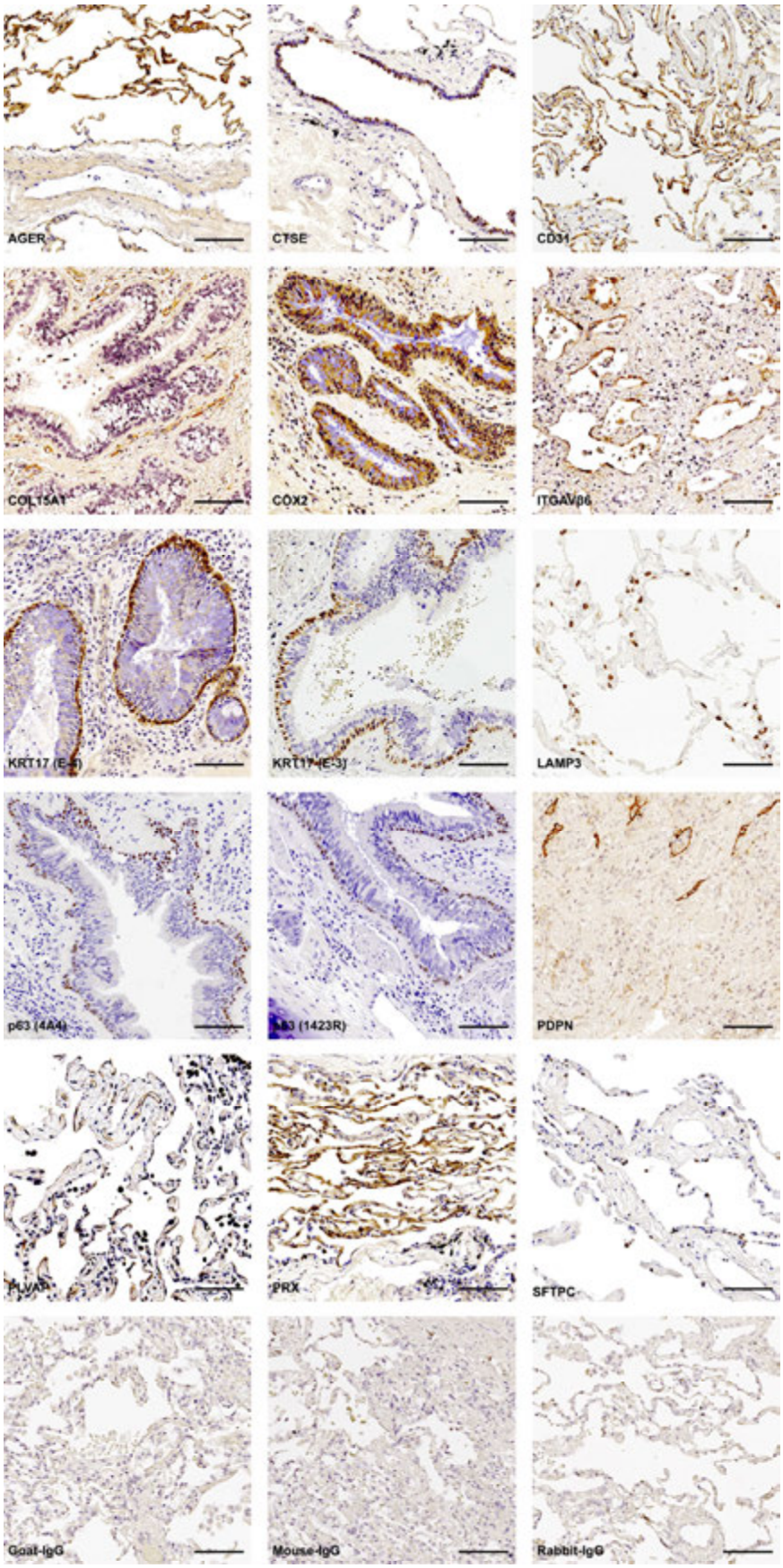

Figure E27: Antibody specificity controls. Representative immunohistochemical stainings illustrating the specificity of all primary antibodies listed in Table E3, as well as the secondary antibodies used for immunohistochemistry in this study. Each panel shows a representative tissue section demonstrating the expected staining pattern in appropriate lung compartments, consistent with known marker localization and cell type specificity. Negative controls using species-matched IgG antibodies are included to confirm the absence of nonspecific background staining. All images were acquired using identical staining and imaging conditions. Scale bars represent 100 µm.